



PCI Journal

Precast/Prestressed Concrete Institute

NOVEMBER—DECEMBER 2021
VOLUME 66, NUMBER 6

Innovation

17

Structured-light three-dimensional scanning for process monitoring and quality control in precast concrete production

33

Axial load limit considerations for 14 in. square prestressed concrete piles

51

Live-load distribution of an adjacent box-beam bridge: Influence of bridge deck



PRESTRESS SUPPLY INC.



Strand chucks & accessories

Stressing equipment

T-630 Concrete Transporter

Form protection coatings

form release agents

Curing covers

Bearing pads

Calibration loadcells

Dynamometers

Testing equipment & supplies

Post-tensioning equipment & supplies

Prestress/Post-tension repair

Wire ties & accessories

Strand sheathing

Rebar & mesh chairs

FL (800) 282-7321, US (800) 328-8036 • sales@psilakeland.com

Visit us at: www.prestresssupply.com

JVI Connections... **Always a *Safe* Bet!**



Your Connection Connection

7131 North Ridgeway Avenue • Lincolnwood, IL 60712 USA
847-675-1560 • 1-800-742-8127 • www.jvi-inc.com



Innovation



17

Structured-Light Three-Dimensional Scanning for Process Monitoring and Quality Control in Precast Concrete Production

17

Rongxuan Wang, Yinan Wang, Sonam Devadiga, Isaac Perkins, Zhenyu (James) Kong, and Xiaowei Yue

Axial Load Limit Considerations for 14 in. Square Prestressed Concrete Piles

33

John C. Ryan and Timothy W. Mays



51

Live-Load Distribution of an Adjacent Box-Beam Bridge: Influence of Bridge Deck

51

Ryan T. Whelchel, Christopher S. Williams, and Robert J. Frosch

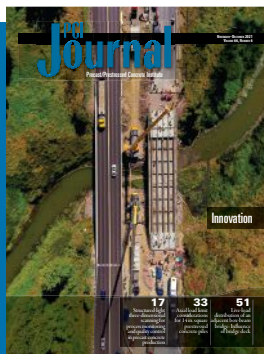
Index of advertisers

CEG..... Inside Back Cover
cegengineers.com
Hamilton Form.....Back Cover
hamiltonform.com
High Concrete Accessories 12
highconcreteaccessories.com

JVI.....1
jvi-inc.com
Prestress Supply Inc.....
.....Inside Front Cover
prestresssupply.com
Tucker's..... 4
tuckerbilt.com

On the cover

Four Interstate 89 bridges in Colchester, Vt., were rehabilitated and had their decks replaced over the course of just four weekends using precast concrete from Fort Miller Co. Inc. and careful planning. Courtesy of Kubricky Construction Corp./The Fort Miller Co. Inc.



DEPARTMENTS

>> Chairman's Message	5
It's Been a Long, Strange Year	
President's Message	7
IAS Accreditation Differentiates PCI-Certified Plants	
From PCI Headquarters	8
PCI Calendar	10
Our Members	11
In the News	13
Industry Calendar	14
Project Spotlight	15
PCI Directories	73
Board of Directors and Technical Activities Council	73
PCI Staff Directory	74
Regional Offices	75
Coming Ahead	75
Meet Kenneth Kruse	76

JOURNAL ADVISORY COMMITTEE

Chair Richard Alan Miller

Vice Chair vacant

Secretary Collin Moriarty

Staff Liaison Tom Klemens

Amir Fam

Alexander G. Mihaylov

Pinar Okumus

Sri Sritharan

EDITORIAL

Tom Klemens Editor-in-Chief

K. Michelle Burgess Managing Editor

Courtney McCormick Technical Editor

Angela Tremblay Technical Editor

Rory Cleveland Copy Editor

Elizabeth Nishiura Copy Editor

Laura Vidale Copy Editor

Laura Bedolla Technical Activities Program Manager

DESIGN & PRODUCTION

Lisa Scacco Publications Manager

Walt Furie Senior Production Specialist

ADVERTISING SALES

Trice Turner Business Development Manager

PCI Journal (ISSN 0887-9672) is published bimonthly by the Precast/Prestressed Concrete Institute, 8770 W. Bryn Mawr Ave., Chicago, IL 60631. Copyright © 2021, Precast/Prestressed Concrete Institute. The Precast/Prestressed Concrete Institute is not responsible for statements made by authors of papers or claims made by advertisers in PCI Journal. Original manuscripts and letters on published papers are accepted on review by the PCI Technical Review Committee. No payment is offered. Direct all correspondence to PCI Journal at journal@pci.org or Precast/Prestressed Concrete Institute, c/o PCI Journal, 8770 W. Bryn Mawr Ave., Suite 1150, Chicago, IL 60631. For information on advertising rates, send an email to adsales@pci.org. Subscription rates are \$80 per year and \$200 for three years in the United States, \$170 per year and \$470 for three years for international, and \$80 per year and \$200 for three years for electronic-only subscriptions anywhere in the world. A single or back issue is \$15. International subscriptions are delivered by an international carrier; allow one to three weeks.

Postmaster: Please send address changes to PCI Journal, 8770 W. Bryn Mawr Ave., Suite 1150, Chicago, IL 60631. Periodicals postage rates paid at Chicago and additional mailing offices.

This paper is milled from a 3rd-party certified source

THE ALL NEW **TUCKERBILT®** T-644

THE ULTIMATE, **SMART**, 6-YARD, CONCRETE TRANSPORT VEHICLE



The new **smart** T-644 vehicle is equipped with the latest CAN-based machine control technology resulting in greater operator control, increased safety, and diagnostic capabilities.

TUCKER'S
MACHINE & STEEL SERVICE, INC.

TUCKERBILT.COM

352-787-3157

P.O. Box 492810 • Leesburg, FL




Its been a long, strange year

As I write this Chairman's Message, I am entering the final third of my year as chair. So far, my experience has been a great one, despite navigating some really strange times. The people I've met and connected with from the different chapters will provide me with lifelong memories and friends. It has also been beneficial to me to hear and discuss how members from around the country are handling the supply-chain demand issues, which if managed correctly, can provide our products an advantage in the marketplace by surpassing our competition's lead times and keeping project time lines on or ahead of schedule.

Unfortunately, I will be repeating myself on this next topic. I have written the same comment in each one of my Chairman's Messages since the very first one and still no action has been accomplished. I am optimistic that our federal lawmakers can do what is needed for our country and our industry by passing legislation to fund transportation. As our elected officials stall on deciding what is and what is not transportation and how it will be paid for, our companies struggle to staff and maintain a workforce that will be ready to take on the challenge when action is finally taken. I urge you to press your congressional representatives to take action and pass transportation legislation.

PCI Committee Days was held September 22 through 24 in Rosemont, Ill. Future PCI Committee Days locations will be rotated every other year between Rosemont and another city beginning with San Antonio, Tex., in 2023. As we've become accustomed to, especially during our current challenges, the PCI staff did a great job organizing and managing the events. The schedule was condensed to shorten the time required away from your companies and families. A similar schedule will be utilized at the 2022 PCI Convention in March. The National Precast Concrete Association (NPCA) has agreed to move the final networking event to Friday night, beginning with the 2025 show, requiring one less day at the show and promoting more PCI member attendance. Please support this move in Kansas City, Mo.

Continuing to build on our strong partnering relationships with NPCA, the executive committees of both associations are meeting October 25 and 26 to review and plan The Precast Show and collaborate on current events, such as government affairs, safety, and workforce development.

I remain encouraged about the future despite some of the negativity that surrounds us all in our lives today. Our industry brings a great deal to the table. Our country needs us to build, provide employment, and prosper, and knowing the people in the prestressed concrete industry as I do, we are ready for the challenge. 



Dennis R. Fink

2021 PCI Board Chair

President

Northeast Prestressed Products LLC

Cressona, Pa.

MARCH 1-5, 2022

SAVE THE DATE

KANSAS CITY CONVENTION CENTER | KANSAS CITY, MISSOURI



2022 PCI CONVENTION

KANSAS CITY, MISSOURI

pci.org/convention | [#PCIConvention](https://twitter.com/PCIConvention)

IAS accreditation differentiates PCI-certified plants


PCI-certified plants are now eligible for accreditation to the International Accreditation Service (IAS) AC157 “Accreditation Criteria for Fabricator Inspection Programs for Reinforced and Precast/Prestressed Concrete” directly through PCI at a significant cost savings over applying directly to IAS.

This eligibility results from the alignment of PCI’s plant certification requirements with those of IAS AC157 so that PCI-certified plants have demonstrated compliance with the key technical provisions of AC157 accreditation as well. Members of the Plant Certification Committee, Quality Activities Council, and PCI staff have worked diligently along with our partners at IAS over the past few years to make the necessary changes to PCI’s certification program to meet AC157 requirements.

Section 1704 of the *2021 International Building Code* states that special inspections are required of fabricated structural, load-bearing members “except where the fabricator has been *approved* to perform work without *special inspections* in accordance with Section 1704.2.5.1.”

Section 1704.2.5.1 states, “*Special inspections* during fabrication are not required where the work is done on the premises of a fabricator *approved* to perform such work without *special inspection*. Approval shall be based on review of the fabricator’s written fabrication procedures and quality control manuals that provide a basis for control of materials and workmanship, with periodic auditing of fabrication and quality control practices by an *approved agency* or the *building official*.”

AC157 accreditation provides a mechanism to become an approved fabricator without requiring approval of the building official on each project. PCI has now made this as easy as filling out an application, completing a cross-reference checklist of the quality system manual to AC157 requirements, and submitting the required IAS fee. Minor revisions to the quality system manual will be required to incorporate specific IAS program references. AC157 also requires two 2-day audits, so additional audit fees may be necessary for plants receiving 1-day audits. PCI has worked out a partnership with IAS that allows PCI members to get AC157 accreditation for about half the cost of getting accredited by IAS directly. More information and an application can be found in the Plant Certification section of the PCI website at https://www.pci.org/PCI/PCI-Certification/Plant_Certification/IAS-AC157.aspx.

Alignment of PCI plant certification requirements with AC157 criteria is unique. It demonstrates the level of attention to quality control necessary to be PCI certified and differentiates PCI-certified plants in the marketplace. We are pleased to be able to provide this value to certified plants and to further demonstrate why architects, engineers, and owners should specify PCI-certified plants for all of their projects. There is no equivalent. 



Bob Risser, PE
PCI President and CEO

FROM PCI HEADQUARTERS

Corbel errata released for *PCI Design Handbook*

Updated errata for the eighth edition of the *PCI Design Handbook: Precast and Prestressed Concrete* have been posted to the PCI website. The recent errata address discrepancies in corbel dimensions. To view the updated errata, go to https://www.pci.org/PCI_Docs/Design_Resources/Guides_and_manuals/8th_DH_Errata.pdf.

New architectural certification guidelines available online as Designer's Notebook

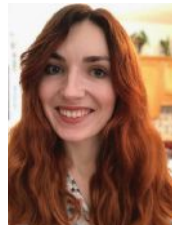
A new Designer's Notebook series is now available from PCI. *PCI Architectural Precast Concrete Certification Category Selection Guidelines*, DN-36-21, provides descriptions of PCI's new architectural precast concrete certification categories that took effect October 1, 2021. Any project being bid on or after this date must be specified using the new categories.

This Designer's Notebook provides a basis for specifying the most appropriate PCI architectural certification categories for the production and field erection of various types of architectural precast concrete components. These five certification categories do not apply to structural components without architectural features.

The *PCI Architectural Precast Concrete Certification Category Selection Guidelines* is available at <https://doi.org/10.15554/DN-36-21>, and all of the Designer's Notebooks are free PDF downloads in the PCI Bookstore.

Kentucky design student Moyles wins \$500 prize for PCI Foundation survey

Juliet Sounders, a graduate student in the College of Design at the University of Kentucky (UK) in Lexington, has won a \$500 prize in an annual drawing of students who take part in the PCI student survey about student experiences in PCI Foundation-sponsored programs. The precast studio at UK is led by Joe Brewer, director of technology and facilities in the College of Design.

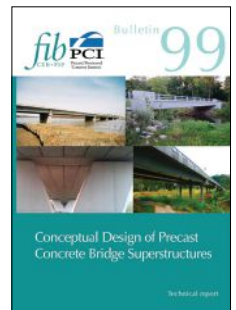


Juliet Sounders

PCI, fib collaborate on bridge superstructure design bulletin

In August, PCI and fib (International Federation for Structural Concrete) released *Bulletin 99: Conceptual Design of Precast Concrete Bridge Superstructures*.

The 276-page technical report prepared by Task Group 6.5 Precast Concrete Bridges takes a closer look at the conceptual (preliminary) design of prefabricated concrete bridges. The bulletin uses 24 examples from around the world to show how leading designers use this methodology to choose a solution that considers all design conditions. The bulletin is available in the PCI Bookstore.



DANIEL P. JENNY FELLOWSHIP CALL FOR APPLICATIONS

Applications for the Daniel P. Jenny Research Fellowships during the 2022/23 academic year are now being accepted. These fellowship awards of up to \$40,000 engage engineering students in precast concrete-related research, introduce students to supporting producers, and provide valuable improvement and development for the entire precast concrete industry. MS degree candidates conducting research related to precast concrete are preferred, but PhD program candidates will also be considered.

Applications are due January 14, 2022. Complete information is available at <https://www.pci.org/JennyFellowship>.

New Committee Central website launches

PCI has launched an improved PCI Committee Central. All information and committee documents are now live on the new site. Following are some of the changes:

- Member and chair work areas have been removed. All actions can be initiated from the committee homepage. The view is based on position on the committee.
- Ballot items can now be moved up and down, and up to four attachments are allowed at the ballot level instead of three.

- Users can create an admin ballot with a 50/50 rule.
- The meeting ballot can capture votes in real time during a virtual or in-person meeting.

Password security requirements have also changed.

Members must still sign in with separate credentials at PCI.org. Usernames are still email addresses; however, passwords must now have at least seven characters and contain one uppercase letter and one number.

To help navigate the new PCI Committee Central, view PCI's how-to videos under "How To's for PCI Website" at <https://www.youtube.com/PCIPrecast/playlists>. Committee Central can be accessed through the Members Only page after you sign into PCI.org. For more information, email membership@pci.org.

PCI FOUNDATION BLOSSOMS OVER 20 YEARS



Twenty years ago, Jim Voss saw that it was going to take a dedicated effort in the education arena to influence how students in architecture, engineering, and construction management learn about precast concrete in school. Not only did the students not know our product but they also didn't know us as an industry.

In 2007, the first year of our fund drive, 16 precast concrete producers, engineering firms, and associates and 5 individuals shared this vision and gave significant contributions, making it possible to start the PCI Foundation programs in earnest. Together they pledged just over \$1 million. The number of companies and individuals in our industry supporting our work continues to grow. Last year, the PCI Foundation received donations from 108 companies and 186 individuals.

As our donor base increases, our programs



Chris Pastorius
PCI Foundation
Chair

expand. More than 6000 students, 75 professors, and 35 schools have taken part in PCI Foundation studio programs. We have added the yearly PCI Foundation Professors Seminar and the Project Precast competition. We also encourage our studios to have precast clubs, enter the Big Beam competition, and connect with our industry through membership in PCI.

To ensure that students know our products prior to graduation and to introduce them to our industry, each studio, club, or competition we sponsor has the same purpose. This is all made possible by having the support of local producers taking part in the studios, associates who donate, and individuals who volunteer time and money to support the work of the PCI Foundation.

The first 20 years have been a time of amazing growth and learning for our industry as well as for the students. We look forward to seeing what the next 20 years brings.



TO DONATE TEXT "PRECAST" TO 41-444

2022 PCI Foundation studio grant applications due December 1

The PCI Foundation is accepting preliminary grant applications for precast studios until December 1, 2021. Precast studios are collaborative education opportunities developed with leading universities with architectural and structural engineering programs. They receive start-up funding grants from the PCI Foundation and are supported by regional PCI associations and local precasters.

For more information, visit Foundation's website at [PCI-Foundation.org](https://www.pci.org). Awards will be announced April 1, 2022.

Metromont's Humphries guest lectures on precast at University of Delaware

Metromont Corp. engineering project manager Eric Humphries recently served as a guest lecturer as part of the PCI Foundation's grant with the University of Delaware in Newark. Humphries presented "Precast Materials, Production, Standard Sections and Applications," one of several guest lectures planned as part of Jovan Tatar's CIEG 404/604 Prestressed Concrete Design course. Tatar is an assistant professor with a research focus on bridges for the future, infrastructure, materials, structures, and sustainability.

PCI's CALENDAR

Events

PCI event details are subject to change. For the most current information, visit <https://www.pci.org/events>.

Marketing and Technical Activities Council Meetings The Biltmore Miami-Coral Gables, Coral Gables, Fla.	January 5-7, 2022
2022 PCI Convention featuring at The Precast Show Loews Hotel, Kansas City, Mo.	March 1-5, 2022
2022 PCI Productivity Tour TradeWinds Island Grand Resort, St. Petersburg, Fla.	May 9-11, 2022
PCI Board of Directors and Committee Meetings Westin New Orleans, New Orleans, La.	June 7-10, 2022
2022 PCI Committee Days and Technical Conference Loews Chicago O'Hare Hotel, Rosemont, Ill.	September 20-24, 2022

PCI personnel training and certification schools

Quality Control School event details are subject to change. If you have any questions about the Quality Control School schedule or need help completing a registration form, please contact PCI's continuing education senior manager, Sherrie Nauden, at snauden@pci.org or (312) 360-3215. Registration forms are available at https://www.pci.org/qc_schools.

Level I and II	November 15-18, 2021 December 6-8, 2021 January 17-19, 2022 February 7-10, 2022	online Nashville, Tenn. Las Vegas, Nev. online
Level III	December 8-11, 2021	Nashville, Tenn.
Certified Field Auditor	January 17-19, 2022	Las Vegas, Nev.

Compiled by K. Michelle Burgess (mburgess@pci.org)

OUR MEMBERS

Mujumdar named to National Academy of Construction

Vilas S. Mujumdar, a PCI Fellow and independent consulting engineer since 2009, was elected to the National Academy of Construction (NAC). Election to the academy is an extensive process based on the contributions, leadership, and service to the engineering profession and advancement of the construction industry.

Mujumdar brings 40 years of engineering experience in the private industry, 10 years in state public



Vilas Mujumdar

service, and 6 years in research management.

He has served on the PCI Seismic Committee for many years and on the first design Handbook review committee. Early in his career, he worked on many precast concrete housing systems and developed one under his own name. He also served on the boards of American Society of Civil Engineers (ASCE) and the Masonry Society and as a trustee of the ASCE Foundation.

Mujumdar is a licensed civil and structural engineer in California and is a fellow of the Institution of Civil Engineers and the Institution of Structural Engineers United Kingdom, the Structural Engineering Institute, the Institution of Engineers in India, and the Society for Risk Analysis.

PCI'S NEWLY CERTIFIED PLANTS AND ERECTORS

PCI recently certified the following plants and erectors. For an explanation of the certification designations, visit http://www.pci.org/Plant_Certification and http://www.pci.org/Erector_Certification.

- C&A Erectors LLC in Rayville, La.: A, S2
- Coreslab Structures (OKLA) Inc. in Oklahoma City, Okla.: S2
- Encore Precast LLC in Dayton, Ohio: B3
- Ideal Contracting LLC in Detroit, Mich.: S2
- Waubensee Development in Aurora, Ill.: A, S2

PCI ARCHITECTURAL CERTIFICATION PROGRAM

The Precast/Prestressed Concrete Institute has established a new PCI Architectural Certification Program to align each PCI precast concrete producer's capabilities with the specific markets it serves. It establishes superior product quality, a third-party inspection mandate, and performance requirements for all certification categories.

BENEFITS OF PCI CERTIFICATION:

- Reduces risk
- Provides the highest probability of a successful project
- Enables prequalification of bidders
- Helps ensure the finished product meets expectations
- Requires less supervision and field inspection, saving time and money

LEARN MORE ABOUT PCI ARCHITECTURAL CERTIFICATION PROGRAM: PCI.ORG/ARCHCERT

WE SET, MEET, AND EXCEED EXPECTATIONS –
AND THAT IS **HOW PRECAST BUILDS**.

HOW PRECAST BUILDS®

PCI
Precast/Prestressed
Concrete Institute

WELCOME TO PCI!



Installers

A.J. McNulty & Co. Inc.

53-20 44th Street
Maspeth, NY 11378
AJMcNulty.com
(718) 784-1655
Primary contact: Elizabeth Weiss
eweiss@ajmcnulty.com

Danny's Construction Co. LLC

1066 W. Third Ave.
Shakopee, MN 55379
DannysConstruction.com
(952) 445-4143
Primary contact: Mark Lannon
mlannon@dannysconstruction.com



Empire Steel Erectors LP

2227 Wilson Road
Humble, TX 77346
EmpireSteelTX.com
(281) 548-7377
Primary contact: Drew Heron
drew@empiresteeltx.com



F. A. Wilhelm Construction Co. Inc.

3914 Prospect St.
Indianapolis, IN 46203
FAWilhelm.com
(317) 359-5411
Primary contact: Will Erwin
willerwin@fawilhelm.com



Peak Construction Group Inc.

660 Liberty Way, Unit C
North Liberty, IA 52317
IowaPeak.com
(319) 383-3474
Primary contact: Steve Oyen
steve@iowapeak.com

Compiled by K. Michelle Burgess (mburgess@pci.org)

Save Time Make a path while avoiding reinforcing



Double Tee
Stem Blockout



U.S. Department of Labor announces enhanced, expanded heat measures

To combat the hazards associated with extreme heat exposure, both indoors and outdoors, the White House today announced that the U.S. Department of Labor is taking enhanced and expanded efforts to address heat-related illnesses.

The department's Occupational Safety and Health Administration (OSHA) is initiating enhanced measures to protect workers better in hot environments and reduce the dangers of exposure to ambient heat.

While heat illness is largely preventable, thousands of workers are sickened each year by workplace heat exposure and 43 workers died from heat illness in 2019. Increasing heat precipitated by climate change can cause lost productivity and work hours, resulting in large wage losses for workers.

To emphasize its concern and take necessary action, OSHA is implementing an enforcement initiative on heat-related hazards, developing a national emphasis program on heat inspections, and launching a rulemaking process to develop a workplace heat standard. In addition, the agency is forming a National Advisory Committee on Occupational Safety and

Health Heat Injury and Illness Prevention Work Group to provide better understanding of challenges and to identify and share best practices to protect workers.

OSHA implemented an intervention and enforcement initiative recently to prevent and protect workers from heat-related illnesses and deaths while they are working in hazardous hot environments. The newly established initiative prioritizes heat-related interventions and inspections of work activities on days when the heat index exceeds 80°F.

The OSHA initiative applies to indoor and outdoor work sites in general industry, construction, agriculture, and maritime where potential heat-related hazards exist. On days when a recognized heat temperature can result in increased risks of heat-related illnesses, OSHA will increase enforcement efforts. Employers are encouraged to implement intervention methods on heat priority days proactively, including regularly taking breaks for water, rest, and shade; training workers on how to identify common symptoms and what to do when a worker suspects a heat-related illness is occurring; and taking periodic measurements to determine workers' heat exposure.

OSHA Area Directors across the nation will institute the following:

- prioritize inspections of heat-related complaints, referrals, and employer-reported illnesses and initiate an onsite investigation where possible

JÖRG SCHLAICH

Jörg Schlaich, a key figure in the development of the strut-and-tie model, died September 4, 2021. He was 86.

Schlaich's industry-changing paper on strut-and-tie modeling, "Toward a Consistent Design of Structural Concrete," ran in the May-June 1987 issue of *PCI Journal* and has been cited more than 1400 times. "It really launched the adoption of STM provisions in the ACI code," says John Breen, a friend of Schlaich's and the Nasser I. Al-Rashid Chair Emeritus in Civil Engineering at the University of Texas at Austin.

When the paper was written, Schlaich was a professor at the Institute of Reinforced Concrete at the University of Stuttgart in Germany, and his coauthors were Kurt Schafer and Mattias Jenne-



Jörg Schlaich

wein. "Toward a Consistent Design of Structural Concrete" is available at <https://doi.org/10.15554/pci.05011987.74.150>.

In 1980, Schlaich cofounded the structural engineering and consulting firm Schlaich Bergermann Partner with Rudolf Bergermann and managed it until 2002.

In 1994, Schlaich was elected an International Member of the National Academy of Engineering "for leadership in structural engineering practice and advancement of economic, environmental, educational, and aesthetic aspects of civil engineering."

Fellow NAE member and consulting engineer David Goodyear says, "I considered Professor Schlaich as the most brilliant structural engineer of our time, not because of his academic prowess, but because of his intuitive understanding of structural engineering."

- instruct compliance safety and health officers, during their travels to job sites, to conduct an intervention (providing the agency's heat poster/wallet card, discuss the importance of easy access to cool water, cooling areas and acclimatization) or opening an inspection when they observe employees performing strenuous work in hot conditions
- expand the scope of other inspections to address heat-related hazards where work site conditions or other evidence indicates these hazards may be present

In October 2021, OSHA will take a significant step toward a federal heat standard to ensure protections in workplaces across the country by issuing an Advance Notice of Proposed Rulemaking on heat injury and illness prevention in outdoor

and indoor work settings. The advance notice will initiate a comment period allowing OSHA to gather diverse perspectives and technical expertise on topics including heat stress thresholds, heat acclimatization planning, exposure monitoring, and strategies to protect workers.

The agency is also working to establish a National Emphasis Program on heat hazard cases, which will target high-risk industries and focus agency resources and staff time on heat inspections. The 2022 National Emphasis Program will build on the existing Regional Emphasis Program for Heat Illnesses in OSHA's Region VI, which covers Arkansas, Louisiana, New Mexico, Oklahoma, and Texas.

—Source: OSHA

INDUSTRY CALENDAR

Event details are subject to change.

World of Concrete 2022

Las Vegas Convention Center, Las Vegas, Nev.

January 18–21, 2022

ACI Spring 2022 Convention

Caribe Royale Orlando, Orlando, Fla.

March 27–31, 2022

Post-Tensioning Institute 2022 Convention

Hilton La Jolla Torrey Pines, La Jolla, Calif.

April 24–27, 2022

2022 fib International Congress

Oslo, Norway

June 12–16, 2022

ACI Fall 2022 Convention

Hyatt Regency Dallas, Dallas, Tex.

October 23–27, 2022

ACI Spring 2023 Convention

Hilton San Francisco Union Square, San Francisco, Calif.

April 2–6, 2023

BEI-2023 "Sustainability in Bridge Engineering"

National University of Singapore, Singapore

Summer 2023

ACI Fall 2023 Convention

Boston Convention Center and Westin Boston Waterfront, Boston, Mass.

October 29–November 2, 2023

ACI Spring 2024 Convention

Hyatt Regency New Orleans, New Orleans, La.

March 24–28, 2024

Compiled by K. Michelle Burgess (mburgess@pci.org)

PROJECT SPOTLIGHT

FDNY rescue facility made for wear and tear

Located in Brooklyn, the new Fire Department of New York (FDNY) Firehouse Rescue No. 2 facility was specifically designed and constructed for training and enabling an elite force of specialized fire and rescue workers in the city to stage and simulate a wide range of emergency conditions in, on, and around the building.

The rescue company is trained to respond to various emergency scenarios, from fire and building collapses to water rescues and scuba operations. During these emergencies, rescuers must often use voids in buildings, whether creating them to let heat and smoke out of a structure or locating them as a means of escape for themselves and others.

As the architect began to learn the tools used by these emergency workers, it helped the firm design and conceive of the structure itself as a training tool. To make sure the facility would be able to meet all of the needs, the architect opted for precast concrete, given that it was ideal to withstand the wear and tear from the fire company for a variety of different training scenarios. High Concrete Group in Denver, Pa., was selected as the precaster.

The three-story building is organized around two large interior voids and enclosed by precast concrete insulated sandwich wall panels, strategically punctured by windows and openings. These interior voids and facade openings enable the fire company to practice multiple rescue scenarios and to mimic

conditions and emergency situations that can occur in urban environments.

In addition, with an *R*-value of 16, the insulated sandwich wall panels help improve the thermal efficiency of the building envelope and reduce the overall HVAC system needs. A green roof, geothermal system, and solar water-heating system also reduce energy use, lowering the building's carbon footprint.

High Concrete Group worked closely with the general contractor to make sure that interruptions were minimal. "High Concrete Group was involved from early on to assist with the BIM coordination," says Sean Dixon, vice president of construction for High Concrete Group. The New York City Department of Design and Construction required a fully coordinated building information model for this project. "The utilization of the model was essential for the coordination between the precast and the terra cotta on this project," he says.

In this urban area, transportation and delivery were important considerations. "HCG had to pay close attention to the delivery schedule and coordination because of the size of the street and the off-site storage," Dixon says. "The precast panels were not small or lightweight, so we also had to consider permits, bridges, city maneuvers, schedule, and storage effectively. Staying true to a schedule and communication on site was the best way to keep this project moving effectively."

Installation also needed to be especially precise. "Maintaining uniform joints while ensuring the openings for the terra cotta installation were maintained required a high level of detail," Dixon says.

—William Atkinson

The new Fire Department of New York Firehouse Rescue No. 2 in Brooklyn, designed for training specialized fire and rescue workers, selected precast concrete for its durability and sustainability. Courtesy of High Concrete Group.





Four Interstate 89 bridges in Colchester, Vt., were rehabilitated and had their decks replaced over the course of just four weekends using precast concrete and careful planning. Courtesy of Kubricky Construction Corp./The Fort Miller Co. Inc.

Vermont rehabs four interstate bridges with minimal closures

In an extremely busy region of Vermont, four Interstate 89 (I-89) bridges that had become severely deteriorated, were rehabilitated and decks were completely replaced over the course of just four weekend closures. In addition, it took just six weekends to complete the entire project, including substructure and steel repairs. The scope of work included deck replacement, steel repairs, and replacement of backwalls, approach slabs, and sleeper slabs.

Precast concrete was immediately identified as a means to execute the goals of this accelerated project, and the Fort Miller Co. Inc. of Greenwich, N.Y., was selected for the project.


The precast concrete panels were match cast in the precaster's production facility with interlocking shear keys to provide reliable shear transfer. The shear keys also self-aligned when being installed, thereby allowing for rapid field setting. During installation, the panels were compressed together by jacking against the girders on the bridge, thereby leaving the completed decks in compression and without cracks. This satisfied the goal of extending the life of the bridge decks by an estimated 40 years.

In all, Fort Miller manufactured 23,535 ft² (286 m²) of bridge deck panels, representing 58 panels, 32 precast concrete approach slabs, 8 precast concrete sleeper slabs, and 32 precast concrete backwalls for the project.

"Manufacturing was done in a long-line match-cast configuration, which provided a higher degree of accuracy for the final product," says John Gonyea, the estimator who worked on the project. "By match casting, every other panel was cast, and then the panels between the previously cast panels were cast." The process was relatively simple, but attention to detail was essential. Casting in this manner allowed for checking the geometry prior to stripping the panels from the casting bed. The match-cast process also allowed the panels to self-align during the installation process, contributing to quick placement in the field.

Transportation and delivery presented challenges. The project was located 120 mi (193 km) from Fort Miller's plant and all of the deliveries associated with the deck panels were oversized, requiring permits and escorts. "Due to the travel time, the restrictions associated with the deliveries, and considering that each individual bridge was to be replaced over 54-hour weekend closures, it was necessary to deliver the panels in advance of the installation dates to an on-site marshalling yard," Gonyea says. By doing so, all of the panels were on site before demolition started, and the contractor had full access to the panels as soon as the decks were removed.

Installation tended to go smoothly, despite some difficult conditions. "The planning process leading up to the installation of each of the bridges was done in such detail, most every challenge was addressed," Gonyea says. The northernmost bridges had access challenges, resulting in the loads having to be backed down into the unloading position, which had a substantial grade and was located within the median between the northbound and southbound bridges. The panels were lifted carefully, using load equalization hardware that automatically adjusted as the panels were lifted. In addition, the match-casting process, specifically the self-aligning characteristics of the panels, contributed to quick installation despite rain and wind affecting a portion of the lifting and placement operation.

—William Atkinson 

Match casting allowed for quick placement in the field during the rehabilitation of four Interstate 89 bridges in Colchester, Vt. Courtesy of Kubricky Construction Corp./The Fort Miller Co. Inc.



Structured-light three-dimensional scanning for process monitoring and quality control in precast concrete production

Rongxuan Wang, Yinan Wang, Sonam Devadiga, Isaac Perkins, Zhenyu (James) Kong, Xiaowei Yue

- This paper presents the use of a structured-light three-dimensional scanner to allow for efficient and real-time inspections of precast concrete specimens. This proposed quality assurance system reviews the quality of a product in three key features: overall dimensions, embedded locations, and surface finishes.
- The experimental program demonstrated that the proposed quality assurance system can quantitatively measure the surface finish of a precast concrete object, recognize and check the location of the embedded metal parts, and validate the overall geometry with the design.

Quality control is a crucial step in the fabrication of precast concrete products. In addition to each component's mechanical properties, three key features ensure a high-quality product: overall dimensions, embedded part locations, and surface finishes. Measuring these three quality features in a highly repeatable and efficient way is challenging. Currently, operators use tape measures to obtain critical overall dimensions and embedded part locations. The tape measure can provide quantitative measurements, but it is not accurate and efficient enough. Measurements from different operators may deviate, and other factors may also affect measurement precision. For example, working temperature can be a source of measurement error because the tape measure, depending on the material, may stretch in high temperatures or shrink in low temperatures. Furthermore, using a tape measure may pose a safety risk if an operator is required to climb onto a ladder or the precast concrete specimen itself multiple times to acquire all of the critical dimensions. As for the third key quality feature, the level of surface finish, judging this relies on the workers' experience because of limited options in real-time measurement devices. Such an experience-based quality control method may result in product quality inconsistency and lead to customer dissatisfaction. Innovative measurement and quality control methods are needed.

In recent years, researchers have developed several quality inspection methods based on the applications of three-dimensional (3-D) scanning and point cloud data.¹ Depending on the specific tasks, the existing conventional methods

PCI Journal (ISSN 0887-9672) V. 66, No. 6, November–December 2021.

PCI Journal is published bimonthly by the Precast/Prestressed Concrete Institute, 8770 W. Bryn Mawr Ave., Suite 1150, Chicago, IL 60631.

Copyright © 2021, Precast/Prestressed Concrete Institute. The Precast/Prestressed Concrete Institute is not responsible for statements made by authors of papers in *PCI Journal*. Original manuscripts and discussion on published papers are accepted on review in accordance with the Precast/Prestressed Concrete Institute's peer-review process. No payment is offered.

focus on dimensional quality inspection, surface quality inspection, or displacement inspection. For dimensional quality inspection, Kim et al.² proposed an automated and noncontact measurement technique using a terrestrial laser scanner to measure and assess the dimensions of precast concrete panels. Wang et al.³ extended the study from checking the dimensional quality of regular shapes to checking shapes with geometric irregularities. Kim and associates⁴ improved the dimensional quality inspection technique by using principal component analysis and testing its performance on full-scale precast concrete objects.

Research on surface quality inspection has mainly targeted surface defects. Liu et al.⁵ employed a digital image processing technique to assess concrete cracks. Kim et al.⁶ presented a technique that can simultaneously localize and quantify spalling defects on concrete surfaces. Wang et al.⁷ used laser scanning to conduct surface flatness and distortion inspection of precast concrete elements.

Recent studies on displacement inspection have explored techniques to detect displacement in large-scale concrete pieces. Gonzalez-Aguilera et al.⁸ proposed a statistical method to monitor the static and dynamic behaviors of large dams based on 3-D laser scanning. Riveiro et al.⁹ developed a terrestrial-laser-scanner- and photogrammetry-based methodology for bridge minimum vertical clearance and overall geometry inspections. Oskouie et al.¹⁰ extracted geometric features of highway retaining walls from laser-scan data and analyzed them to detect displacements.

There are two limitations in the aforementioned studies. First, the point cloud data were acquired using a time-of-flight laser scanner.¹¹ This type of machine shoots a laser beam onto the surface and determines the distance between the machine and the surface by calculating the laser travel time. Although this method is accurate and has long-range coverage, it is time-consuming when high-density surface data are required because it only measures one spot each time.

Photogrammetry¹² is one alternative 3-D scanning technique. It uses multiple pictures taken from different angles to complete the 3-D reconstruction. This method has the advantage of low cost because only one camera is needed, but it has low accuracy.

Another option is to use structured-light scanning (SLS)¹³, which uses a triangulation-based method. This type of 3-D scanner consists of two cameras and a projector. The projector projects a fringe pattern onto the surface, and from the camera's point of view, the pattern is distorted. Such distortion can be used to calculate the surface geometry. SLS has three advantages compared with laser scanning. First, it does not create any laser safety hazards, such as eye injury, and provides a safer working environment in which no extra eye protection is required. Second, SLS is faster than laser scanning and yields higher-resolution results. An SLS scanner takes just a few seconds to scan millions of data points, whereas a laser scanner scans line by line and at a slower

pace. Third, SLS costs less to purchase (typically just a few thousand dollars, whereas a laser scanner can cost more than \$20,000). SLS also works well in a range of light conditions because the scanning software can automatically optimize the settings of the camera (exposure time and gain) and projector (brightness). One potential concern is that the coverage area of the projector that comes with commercialized SLS systems may be too small for scanning typical full-scale precast concrete parts (such as those longer than 20 m [66 ft]). This issue can be resolved by replacing the current office-grade projector with a professional-grade projector (about \$2000 to \$3000), which can provide a very large coverage area. Suggestions for implementing SLS systems in a factory environment are provided at the end of this paper.

The second limitation of the previously described research is that the studies all mainly focused on inspecting a single type of quality issue in precast concrete. However, on the real production line, a systematic quality inspection including the surface finish check, overall dimension check, and embedded parts location check is needed before the final product can be delivered. Furthermore, precasters need user-friendly, operator-accessible software to integrate all the developed techniques.

The main purpose of this paper is to propose a 3-D scanning-based quality inspection and data analytics system for precast, prestressed concrete production. The specific innovations can be summarized as follows:

- adapting SLS to perform the surface and geometric measurements
- developing a set of algorithms to conduct a systematic quality inspection of precast concrete
- providing a user-friendly graphical user interface (GUI) to standardize and simplify the operations

The framework of the proposed quality control system (**Fig. 1**) contains a set of hardware and algorithms and provides a highly reliable and repeatable way to accurately and efficiently complete the three key quality inspection tasks (surface finish check, overall dimension check, and embedded parts location check). This system can substantially reduce operator errors and safety hazards and has the advantages of low cost and short measuring time. When this system was tested using a precast concrete sample that contained multiple surface finishes, complicated surface geometries, and embedded metal plates to mimic all three critical features in real concrete products (**Fig. 2**), it proved to be effective.

Experiment setup and raw data visualization

In the experiment, a mock-up concrete sample with complex shapes, embedded metal parts, and multiple types of surface finish was made by Tindall Corp. The computer-aided design (CAD) drawing of the precast concrete sample is shown in

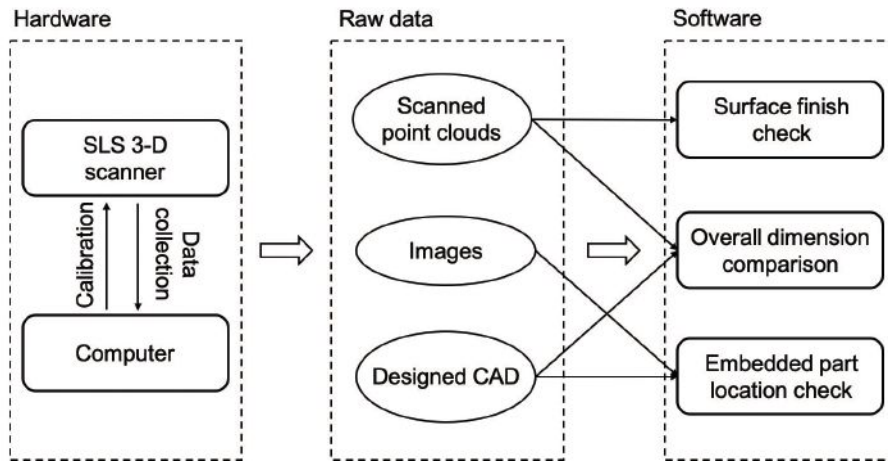


Figure 1. The framework of the proposed quality control system. Note: CAD = computer-aided design; SLS = structured-light scanning; 3-D = three-dimensional.

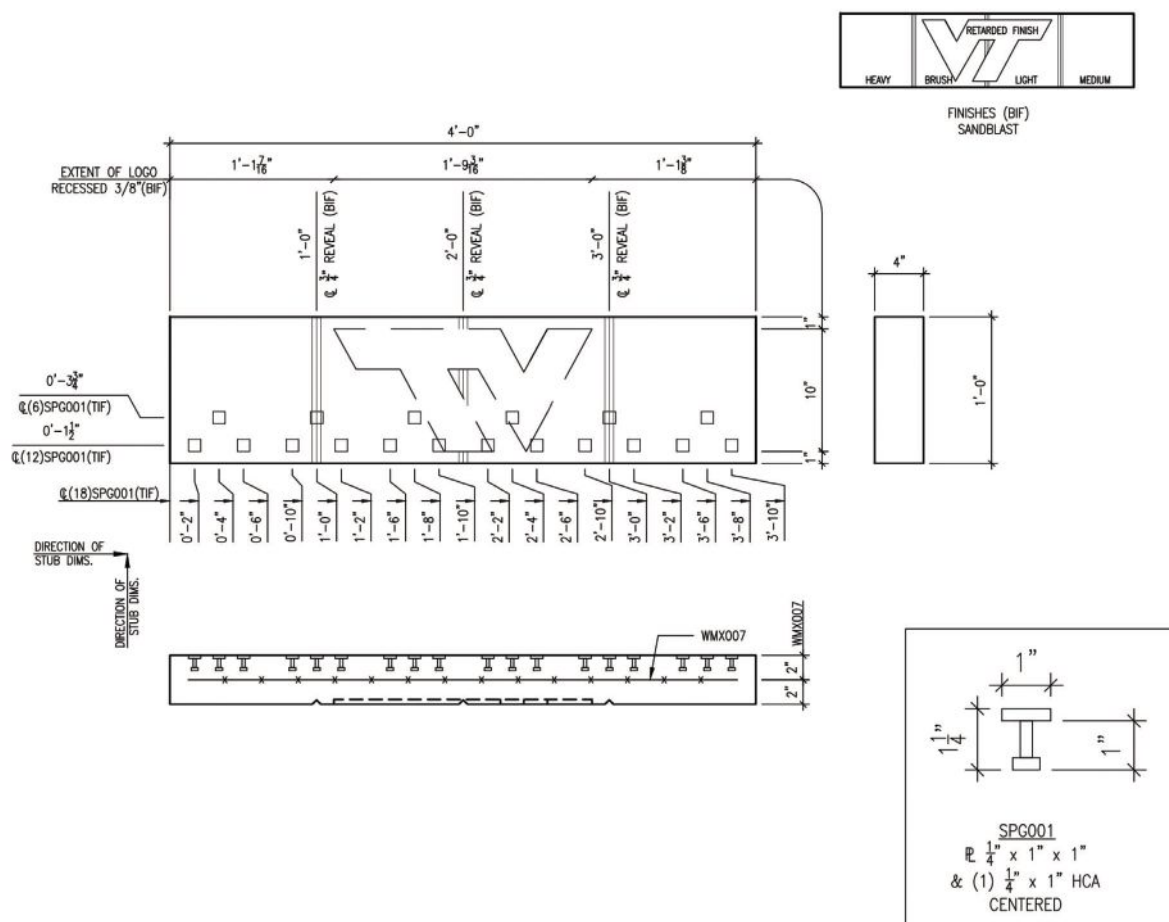


Figure 2. Engineering drawing for mock-up part. Note: BIF = bottom in form; CL = center line; Dims. = dimension; HCA = headed concrete anchor; PL = plate; SPG001 = part number of the anchor; TIF = top in form; WMX007 = part number of the reinforcing bar. 1" = 1 in. = 25.4 mm; 1' = 1 ft = 0.305 m; 1 lb = 4.448 N; 1 psi = 6.895 kPa.

Fig. 2. This test specimen is 4 ft (1.2 m) long, 1 ft (0.3 m) wide, and 4 in. (102 mm) thick. It is a scaled-down test sample that has all the features of interest in real practice. For example, as Fig. 2 illustrates, five commonly used surface finishes are applied to the different regions of the sample surface to test the capability of the proposed system.

A 3-D scanner was used to capture the surface point cloud data from the mock-up sample. **Figure 3** shows the experimental setup. The precast concrete sample was lifted by a crane, and the scanner was placed about 5 ft (1.5 m) away from the sample. Each of the front and back surfaces was covered by two separate scans. The scanner further registered and fused the two front and two back scans to generate the complete surfaces. The first and second rows in **Fig. 4** present the scanned data with and without surface texture information, respectively. Each scan took about 3 seconds to capture the raw data and 15 seconds for the software to complete the triangulation calculation. Once the scan was finished, the result could be loaded into the GUI for quality analysis.

Functional modules

The software for the proposed quality assurance system consists of three modules: overall dimension check, embedded part location check, and surface finish check. The detailed

methodologies for these three functional modules are discussed in this section.

Overall dimension check

The overall dimension check evaluates whether the sample's overall geometry satisfies the geometric dimensions and tolerances specified in the design. This check can identify the areas that failed to meet the designed shape and tolerances. Current quality assurance procedures are achieved by limited point-to-point measurements, such as using a tape measure to measure the length of a precast concrete component; however, precast concrete can distort during curing, which creates a 3-D shape change that cannot be measured accurately with a tape measure. With the proposed quality assurance system, a comparison between the entire surface and the designed geometry is conducted after the concrete is fully cured and cooled. To do so, the CAD model (Fig. 4) is first obtained based on the engineering design (Fig. 2). **Figure 5** illustrates the three-step process of overall dimension check:

1. Register the iterative closest point (ICP) between the designed point cloud from the CAD model and scanned point cloud data.
2. Calculate the pointwise distance based on registration results.

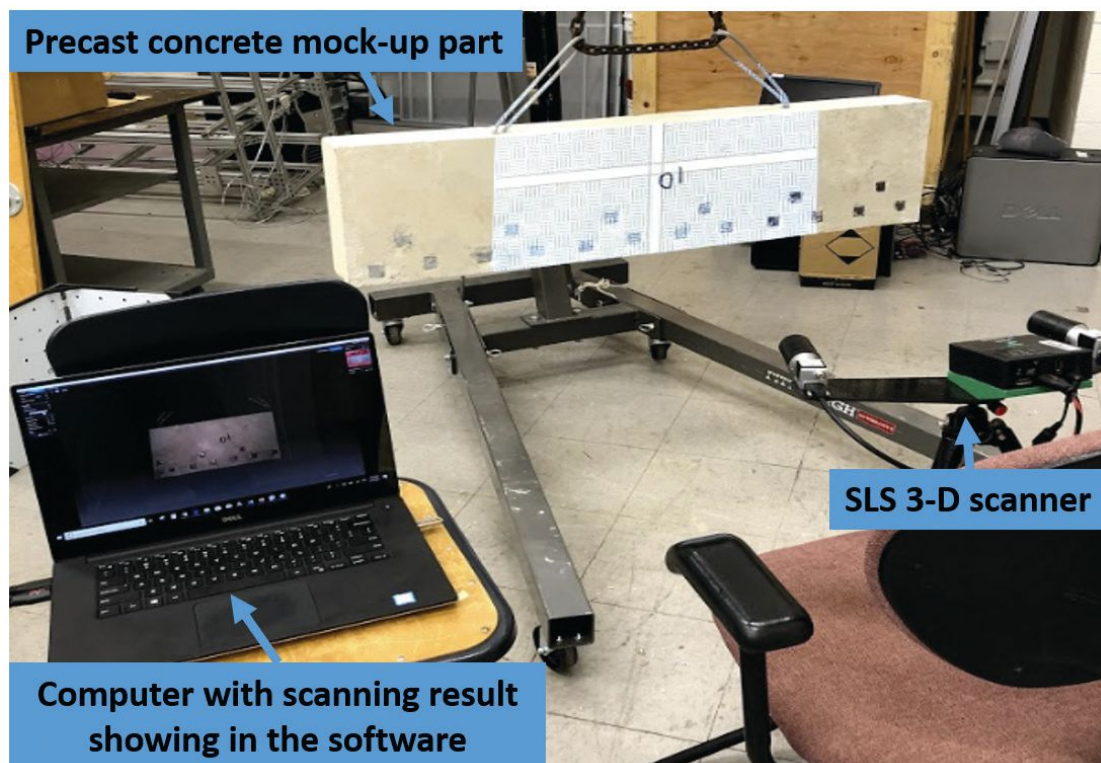


Figure 3. Three-dimensional scanning process of precast concrete sample. Note: SLS = structured-light scanning.

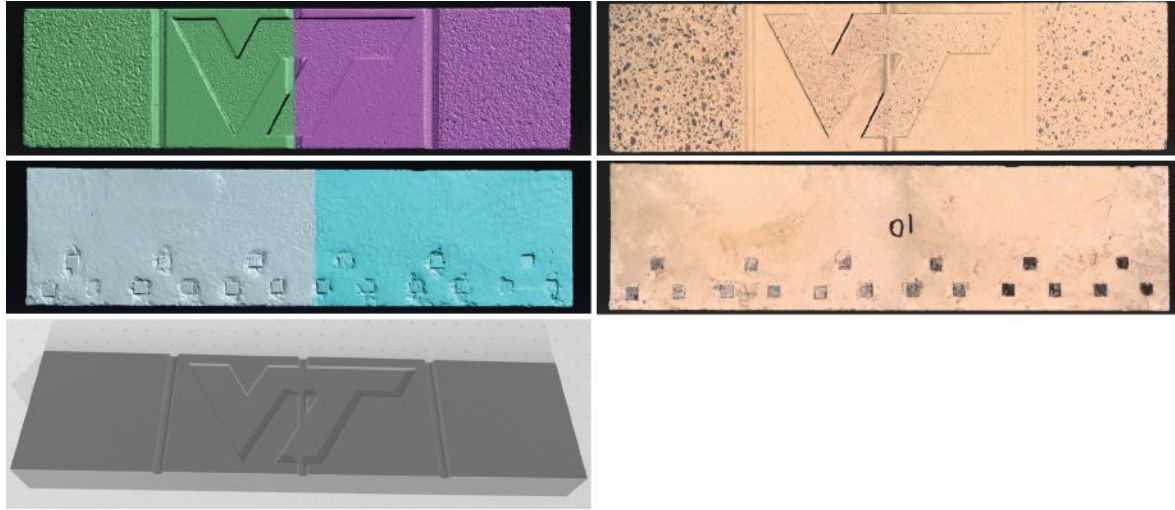


Figure 4. The top row shows three-dimensional surface scan results without texture information and with different colors to represent the results from different scans. The second row shows three-dimensional surface scan results with texture information. The third row shows the computer-aided design model of the mock-up part.

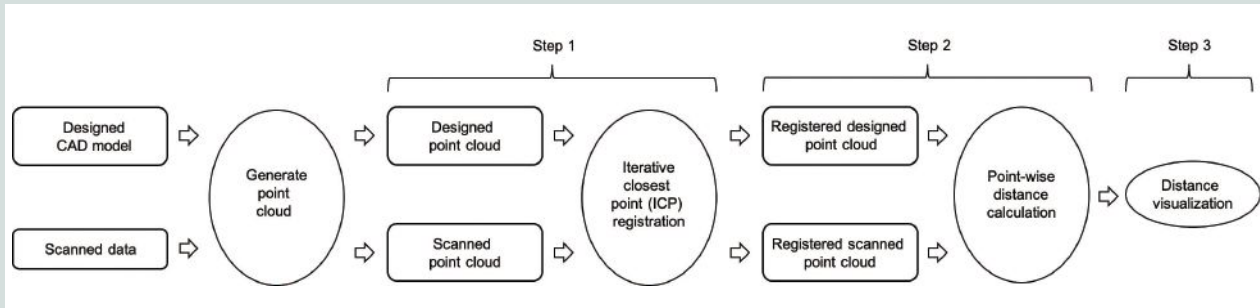


Figure 5. Process of overall dimension check. Note: CAD = computer-aided design.

3. Visualize the distance to show the difference between the designed product and the real product.

Registration matches two point clouds for the same object by rotation and translation. In this experiment (Fig. 5), the designed point cloud was sampled from the CAD model to represent the standard geometry of the precast concrete component and the SLS 3-D scanner was used to collect the scanned point cloud representing the actual dimensions of the product. Ideally, after registration, these two point clouds would be perfectly matched; this would mean there are no production errors and the product is strictly consistent with the design; however, production errors are inevitable and will lead to deviations in some local areas.

The ICP algorithm has been used to minimize the position difference between two point clouds.¹⁴ If the designed point cloud C is denoted as $C \in \mathbb{R}^{N \times 3}$ and the scanned point cloud S

is denoted as $S \in \mathbb{R}^{N \times 3}$, where N is the number of points, the objective function of registration can be formulated as follows.

$$\min(\text{dist}(\tilde{S}, C))$$

$$\text{subject to } \tilde{S} = R \times S + T$$

where

\min = minimum

$\text{dist}(\cdot)$ = distance function evaluating the difference between two point clouds

\tilde{S} = registered scanned point cloud

R = rotation matrix

T = translation matrix

Algorithm 1, the iterative closest point algorithm, summarizes the ICP algorithm procedure. After ICP registration, the registered scanned point cloud \tilde{S} is generated and then the deviation between the \tilde{S} and C is calculated using the multi-scale model-to-model cloud comparison (M3C2) distance¹⁵ to reflect the production error.

For algorithm 1, input the following:

1. $C \in \mathbb{R}^{N \times 3}, S \in \mathbb{R}^{N \times 3}$
2. initial estimate of correspondence points in C and S

Then loop the following:

3. **While not Converge Do.**
4. Determine the correspondence: for each point in S , find the closest point in C .
5. Find the best transform (rotation and translation matrices) for this correspondence.
6. Transform S .

Embedded part location check

If the metal embedded plates used to attach precast concrete parts are mispositioned during the manufacturing process, the product cannot be installed properly. To address this quality concern, the embedded part location check was developed to obtain the positions of embedded metal parts and then compare those positions with positions in the design file. In the experiment, multiple metal plates were embedded on the surface of the precast concrete sample (Fig. 2). **Figure 6** illustrates the process of metal plate detection and comparison. The inputs of the embedded part location check are raw images taken during the 3-D scanning process. The detection process has five steps:

1. image binarization
2. noise filtering
3. edge detection
4. shape detection
5. and position extraction and comparison

This algorithm is not limited to detecting metal plates; it can also be easily extended to detect other critical parts, such as hooks or slots.

Image binarization

We binarize the original image and transform it into black and white to improve efficiency without using losing critical information. Note that the original image from the experiment is in RGB color format and can be denoted as $I \in \mathbb{R}^{H \times W \times 3}$, where I is a three-way tensor representing the color image and H and W represent the height and width of the image, respectively. The intensity of each pixel I_{ij} is represented by a vector $[r, g, b]$, which denotes the intensity of the colors red, green, and blue in this pixel. Before binarization, the image is initially transformed into grayscale using the equation given below.

$$\tilde{I}_{i,j} = 0.3 \times I_{i,j}(1) + 0.59 \times I_{i,j}(2) + 0.11 \times I_{i,j}(3)$$

where

\tilde{I} = the grayscale image with the shape of $H \times W$

$\tilde{I}_{i,j}$ = the grayscale pixel intensity at position (i,j) in grayscale image

$I_{i,j}(1)$ = the intensity of color red

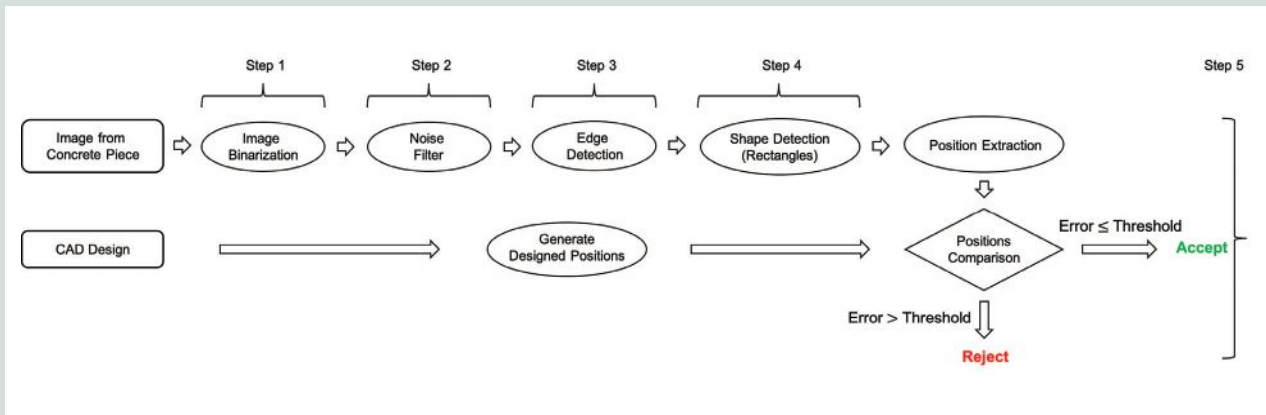


Figure 6. Process of metals detection and comparison. Note: CAD = computer-aided design.

$I_{ij}(2)$ = the intensity of color green

$I_{ij}(3)$ = the intensity of color blue

The binarization is then conducted on the grayscale image by setting a threshold value to binarize the value of each pixel. For a given threshold value, if the pixel value in the grayscale image is greater than the threshold, the corresponding pixel value in the binarized image is set to 255 (white), otherwise the corresponding pixel value is set to 0 (black).

Noise filtering

Some noise (black dots) might remain in the binarized image because the concrete might not be perfectly clean and smooth. The second step is to filter the noise to make the background as smooth as possible. The median filter is selected to eliminate noise from the background. The aim is to slide a square window over the image and replace the center pixel value with the median of all pixel values in the window (5 × 5 pixels).

Edge detection

After noise filtering, the edges of embedded parts can be detected by transforming the image to a gradient map and then using high-pass filters to capture the positions where pixel values change significantly (from white to black). The gradient operator is applied to the noise-filtered image to calculate the magnitude of the pixel-wise gradient. The expressions of a typical gradient operator are as follows.

$$\frac{\partial \tilde{I}_{ij}}{\partial x} = -\frac{1}{2} \tilde{I}_{i-1,j} + \frac{1}{2} \tilde{I}_{i+1,j}$$

$$\frac{\partial \tilde{I}_{ij}}{\partial y} = -\frac{1}{2} \tilde{I}_{i,j-1} + \frac{1}{2} \tilde{I}_{i,j+1}$$

$$|\nabla \tilde{I}| = \sqrt{\frac{\partial \tilde{I}^2}{\partial x} + \frac{\partial \tilde{I}^2}{\partial y}}$$

where

$\tilde{I}_{i-1,j}$ = the intensity of pixel at position $(i-1, j)$ in grayscale image $\tilde{I} \in \mathbb{R}^{H \times W}$

$\tilde{I}_{i+1,j}$ = the intensity of pixel at position $(i+1, j)$ in grayscale image $\tilde{I} \in \mathbb{R}^{H \times W}$

$\tilde{I}_{i,j-1}$ = the intensity of pixel at position $(i, j-1)$ in grayscale image $\tilde{I} \in \mathbb{R}^{H \times W}$

$\tilde{I}_{i,j+1}$ = the intensity of pixel at position $(i, j+1)$ in grayscale image $\tilde{I} \in \mathbb{R}^{H \times W}$

After determining the magnitude of the pixel-wise gradient, a gradient threshold is applied to decide whether edges are present at an image point.

Shape detection

In many cases, workers use pens to mark part numbers on precast concrete components, as seen as “01” in the scans. These marks cannot be easily removed from images and would be counted as edges in the previous edge-detection step. Therefore, to address this type of image noise, we apply a shape detection method.¹⁶ During shape detection, connected edges are assigned to the same contour, and then the shapes of all of the generated contours are checked. Only contours with the rectangular shape are preserved in the image, allowing the rectangular embedded parts to be successfully identified.

Position extraction and comparison

The locations of the detected embedded parts can be found by the centers of the rectangular contours. These locations are recorded in pixels. Subsequently, the pixel-to-dimension ratio of the image is calculated based on the corresponding concrete dimensions to transform the metal plate positions from pixels to inches.

After extracting the positions of embedded parts, position errors can be calculated and annotated by comparing the extracted positions with the designed positions in the CAD file. As the sizes of metal parts are determined, a position error is defined as the distance between the center of an extracted location and the center of the corresponding designed location. The error is calculated by the Euclidean distance between the designed center position (x, y) and the product's center position (\hat{x}, \hat{y}) , which is given as follows:

$$\text{error} = \sqrt{(x - \hat{x})^2 + (y - \hat{y})^2}$$

Surface finish check

The surface finish check aims to provide quantitative guidance for architectural precast concrete finishers to meet the requirements of their customers. The surface finishes are calculated based on the point cloud data acquired from the 3-D scanner and can be quantified by the mean distance between the measured points and the locally fitted plane. The globally fitted plane is not used here because the real product might have deformations due to stress or molding error. These deformations introduce errors in surface finish calculations. Calculating the surface finish based on the locally fitted plane can eliminate the influence of overall deformation.

Calculating distances between point cloud and fitted plane

The surface point cloud data can be represented in the 3-D space by a set of points (x_i, y_i, z_i) that represent the position of point i along each axis. To generate a locally fitted plane, the first step is to segment a subregion of the point clouds. Second, we suppose that the selected points distribute on the same plane, with the expression of the plane given as Eq. (1).

$$A\beta = B \quad (1)$$

where

$$A = \begin{pmatrix} x_1 & y_1 & 1 \\ \vdots & \vdots & \vdots \\ x_N & y_N & 1 \end{pmatrix}, \text{ represented by } A \in \mathbb{R}^{N \times 3}, \text{ the } i_{th} \text{ row of } A \text{ is denoted as } A_i = [x_i, y_i, 1]$$

β = unknown parameters of this plane, represented by $\beta \in \mathbb{R}^{3 \times 1}$

B = $[z_1, \dots, z_N]^T$, represented by $B \in \mathbb{R}^{N \times 1}$, the i_{th} row of B is denoted as $B_i = [z_i]$

Given the points in the segmented subregion, we can derive the solution of unknown parameters (Eq. [2]).

$$\hat{\beta} = (A^T A)^{(-1)} A^T B \quad (2)$$

$\hat{\beta}$ = the estimated parameters of this plane

A^T = the transpose of A

The absolute distance D between the selected points and the locally fitted plane can be calculated by Eq. (3).

$$D = |B - A\hat{\beta}| \quad (3)$$

where

$$D \in \mathbb{R}^{N \times 1}$$

$| \cdot |$ = the element-wise absolute operation

The positive values in $B - A\hat{\beta}$ represent the corresponding points above the fitted plane, and the negative values represent the corresponding points below the fitted plane.

The mean and variance of D are selected to represent the roughness of the segmented subregions. The second row in **Fig. 7** presents some examples of the surface finish visualization.

Summarizing local results to reflect overall surface finish

Given D is calculated for each subregion, the overall surface finish can be represented by the mean and variance of D from all subregions. The test sample had five different surface finishes: light, medium, heavy, brush, and retarded (Fig. 2). Each finish was quantified individually. Figure 7 shows the pipeline to obtain the surface finish statistics for the test sample. The entire process can be summarized in three steps. First, for each

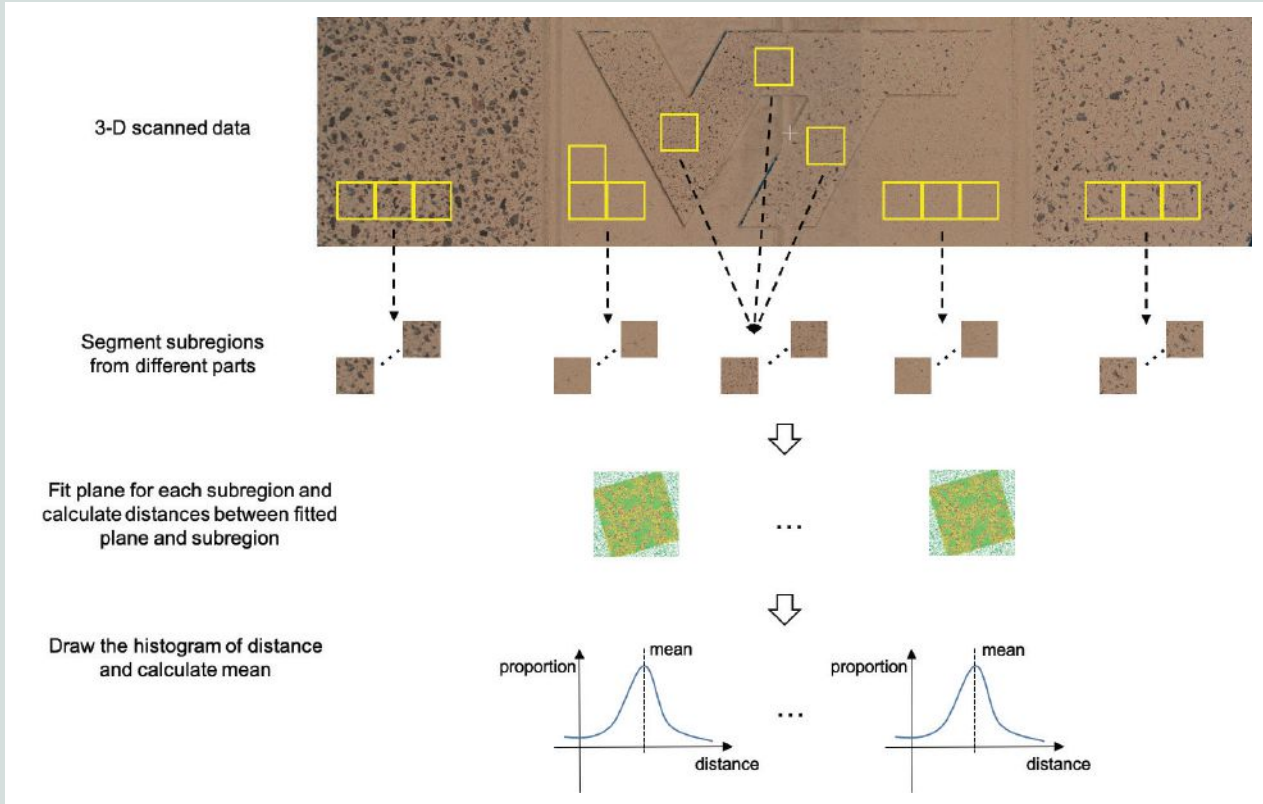


Figure 7. Overview of the surface finish statistics pipeline. Note: 3-D = three-dimensional.

type of finish, 20 subregions (each approximately 1.2×1.2 in. [30×30 mm]) were segmented from the raw data. Then, for each subregion, the pointwise distance between the subregion and its fitted plane was calculated based on Eq. (1) through (3). Finally, for each type of finish, the roughness statistics were calculated using all the corresponding segmented subregions. The control limit was set to 1 standard deviation.

Experiment results

This section describes the results of the experiments conducted on the mock-up precast concrete sample to validate the performance of the proposed quality assurance system.

Overall dimensions check

Results calculated from the ICP and M3C2 algorithms described earlier are visualized in **Fig. 8**, where the various colors indicate the magnitude of M3C2 distances on each point, representing the deviations between the design and the real

product. In this precast concrete sample, the upper-left corner exceeds the tolerance because of over-etching or excessive sandblasting and the conjunction lines between different surface finishes also have significant differences due to the molding inaccuracy. The proposed quality system can check both overall dimension quality and irregular shapes in the real product.

Embedded parts location check

The results of the embedded parts location check are visualized in **Fig. 9**, in which the blue boxes represent the design metal plate locations while the yellow boxes represent the measurements. The error is annotated by the side of each metal plate, where green represents an acceptable difference and red represents an unacceptable difference. The tolerance to distinguish the acceptance is currently set to 0.1 inches and can be modified given production requirements. In general, the mismatching of the two colored boxes indicates the direction of the error, and the calculated annotated error number indicates numerically how much the difference is.

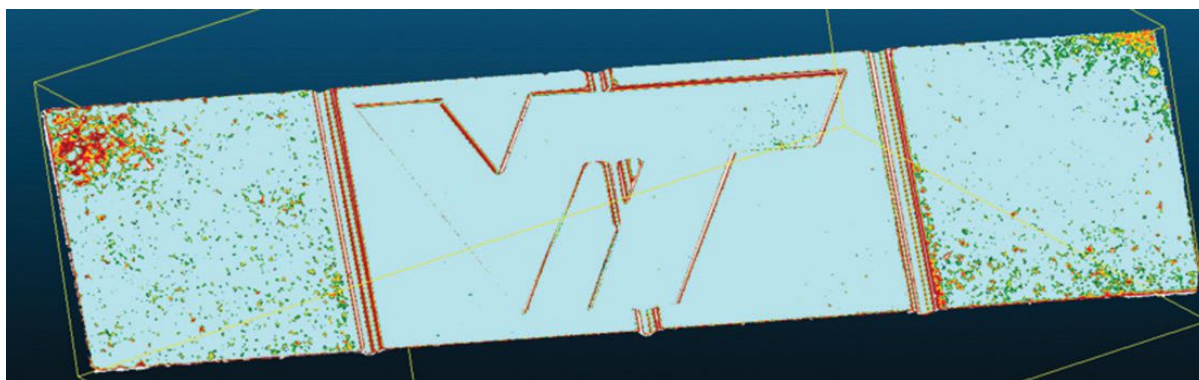


Figure 8. Geometry comparison between the scanned surface and the computer-aided design. The difference is following the cyan-green-yellow-red order, where red means the area with the largest deviations.

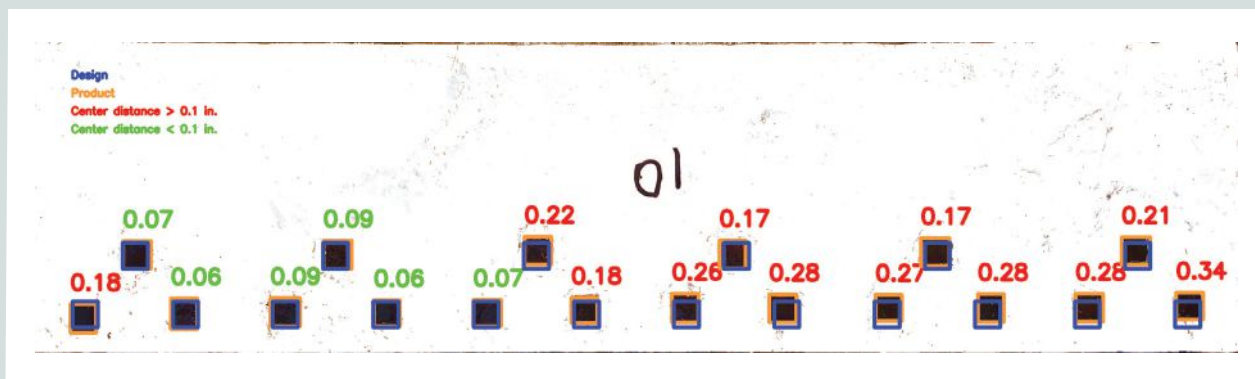


Figure 9. Results of back metal detection and comparison, where green indicates acceptable and red means out of range. Note: 1 in. = 25.4 mm.

Surface finish check

Table 1 presents the quantified results of the surface finish check for the sample's five different surface finishes. The results show substantial differences in mean values among the different surface finishes. The mean values can be used to automatically differentiate and recognize the type of surface finish during the quality inspection. The control limit is set to 1 standard deviation from the mean. It can provide a quantitative guideline for workers to perform sandblasting. The first two rows in **Fig. 10** illustrate graphical tools—a histogram of absolute distances and 3-D visualization of different surface

Table 1. Mean, standard deviation, and tolerance for each surface finish region

Type of surface finish	Mean	Standard deviation	Tolerance
Heavy	0.2759	0.0371	0.2759 ± 0.0371
Medium	0.2115	0.0215	0.2115 ± 0.0215
Retarded	0.1065	0.0099	0.1065 ± 0.0099
Light	0.0527	0.0078	0.0527 ± 0.0078
Brush	0.0245	0.0030	0.0245 ± 0.0030

finishes—that can be used to visualize the differences among various surface finishes. The last row in **Fig. 10** shows the calculated roughness at selected subregions. This graph can be accessed in the developed GUI, where the user can define the location and size of the subregions.

Graphical user interface

The algorithms of the three quality control functions are integrated into a GUI, which was built in Python on the Tkinter library. The GUI contains four parts: a menu (for loading all the necessary data) and the three quality inspection modules (**Fig. 11**).

Module 1: Metal plate location

Figure 12 illustrates the process and results of module 1. The inputs required to activate module 1 are an image (PNG or JPEG) of the back of the precast concrete part and a comma-separated value (CSV) file with design positions of metal plate and dimensions of the precast concrete sample.

Module 2: Overall dimension check

As described earlier, the process of overall dimension check includes three steps:

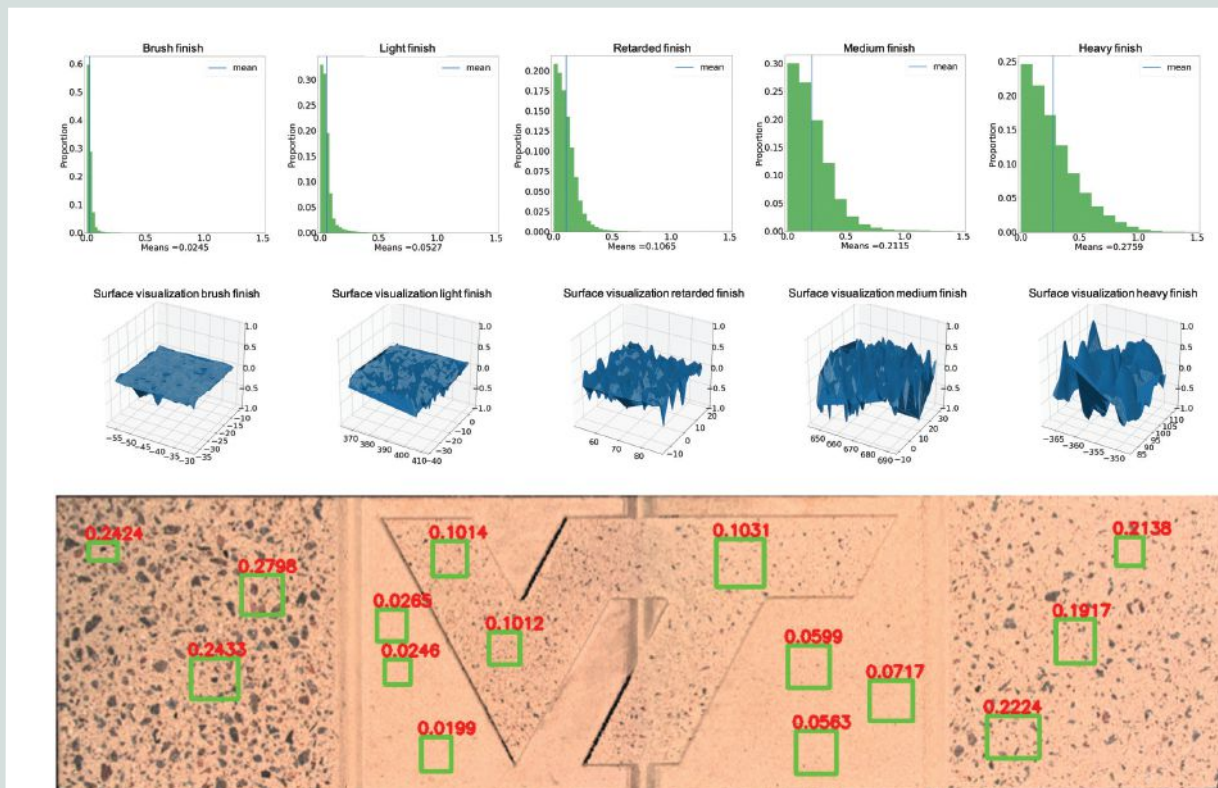


Figure 10. The top row shows the surface finish quantification results for brush, light, retarded, medium, and heavy finishes. The second row shows the surface finish visualization (examples) for brush, light, retarded, medium, and heavy finishes. The third row shows quantified surface roughness on example regions.

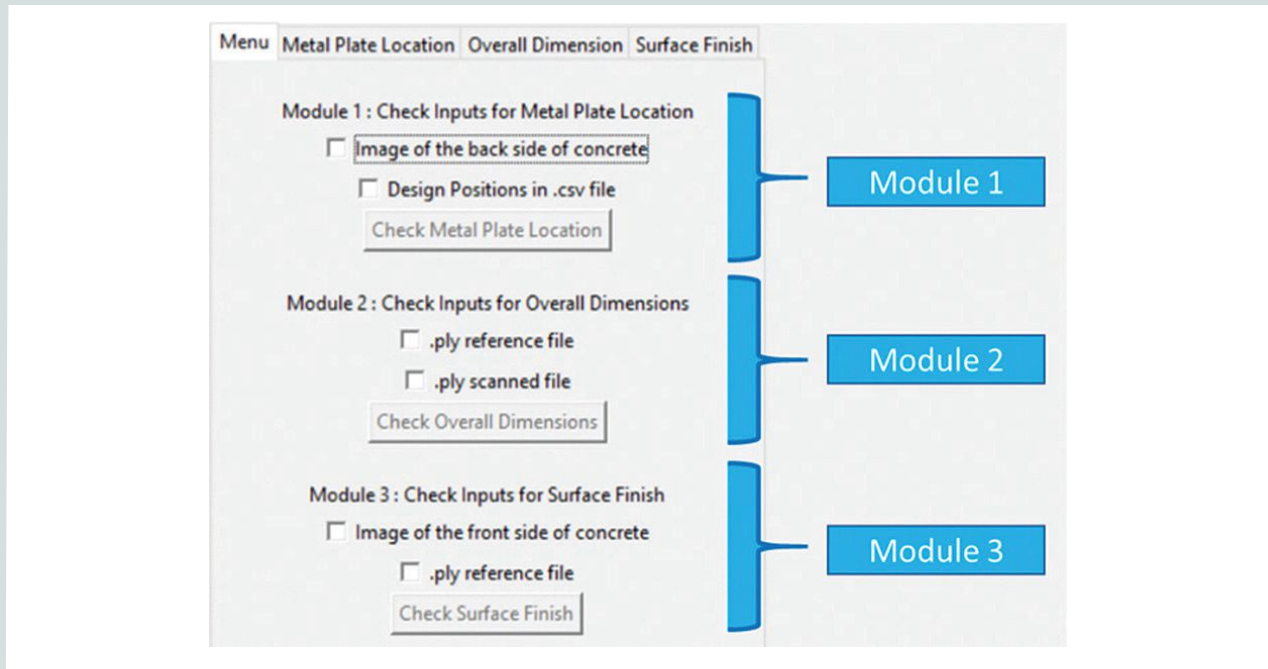


Figure 11. Menu tab on the graphical user interface along with the three module tabs.

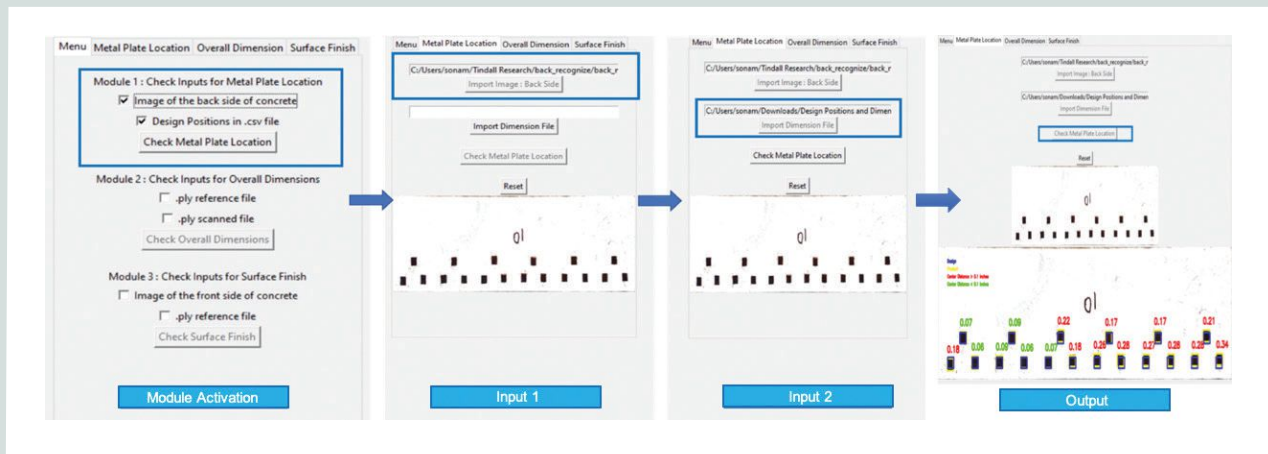


Figure 12. Process and result of module 1: metal plate location.

1. Register the ICP between the designed point cloud from the CAD model and scanned point cloud data.
 2. Calculate the pointwise distance based on registration results.
 3. Visualize the distance to show the difference between the designed product and the real product.
- the PLY reference file of the front side of the precast concrete part (from the designed CAD file)
 - the PLY scanned file of the front side of the precast concrete part
 - the BIN file created from the registration process
 - the ASC distance file created from the comparison (keyword "M3C2" in the filename)

The following are the primary inputs required to activate the first step of module 2:

The final overall dimension check can be visualized in the GUI (Fig. 13).

Module 3: Surface finish

The inputs required to activate module 3 are the .ply reference file of the front side of the precast concrete sample, the PNG or JPEG image of the front of the precast concrete sample, and the number of crop areas to be made. The crop area command activates the open 3-D window. **Figure 14** shows the cropping process and the evaluation results of cropped areas.

Summary and implementation suggestions

The proposed 3-D scanning-based precast concrete quality assurance system can quantitatively measure the surface finish of a precast concrete object, recognize and check the location of the embedded metal parts, and validate the overall geometry with the design. Additionally, the surface finish standard, developed based on the statistical analysis of different types of finishes, can be adapted for future surface quality inspection applications. The proposed quality assurance system can



Figure 13. The final output of module 2: overall dimension check.

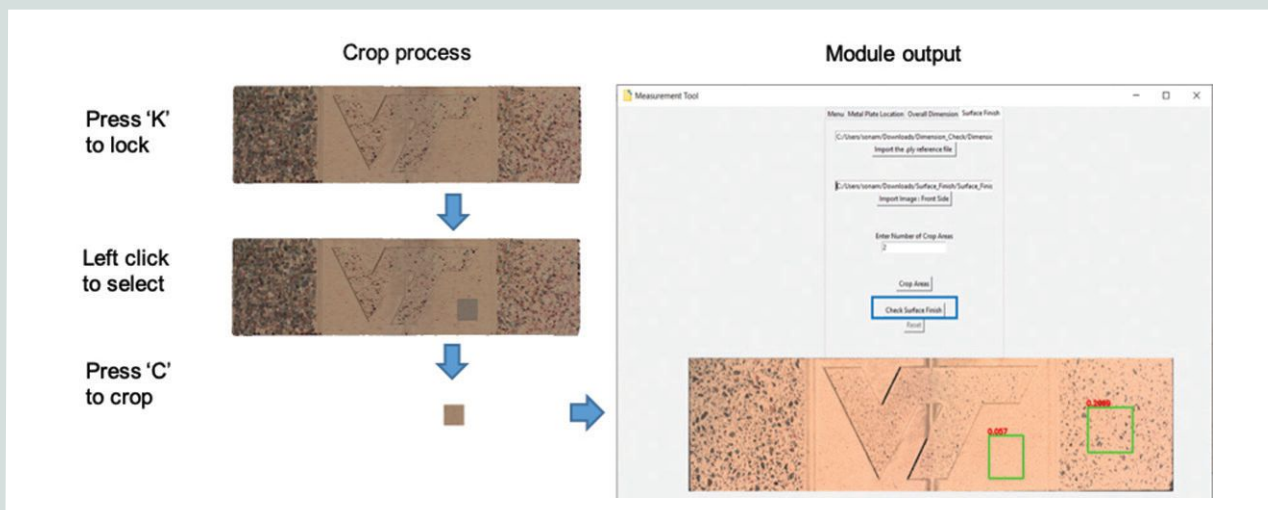


Figure 14. Crop process and output of module 3: surface finish.

provide high accuracy and efficient quality inspection and analysis. The scanned data and analysis results can be used for real-time analysis of product quality in the production process and the GUI software can satisfy the data analysis and visualization requirements in precast concrete quality inspection. Furthermore, this system can help to reduce operators' workload and safety hazards.

The system proved to be effective for the precast concrete quality assurance system and has the potential to be implemented in real practice.

For an industrial setup, a 3-D scanner with a larger field of view (FOV) than the currently marketed model must be built and calibrated. The long side of the FOV can be determined by the largest width of the products or the width of the crane. Most 3-D scanning software has stitching functions that can combine several scans to a whole part (the first two rows in Fig. 4). A 3-D scanner appropriate for industrial use can be built by modifying the currently available SLS system. Both the projector and the two cameras would need to be modified to fit the desired configuration.

In the factory, the entire scanning system could be mounted on a gantry crane with the projector on the center of the crane and the cameras at two sides, and faced downward. The suggested angle between the projector and camera is 15 ± 3 degrees.

A professional-grade projector (for example, Epson PowerLite L510U WUXGA 3LCD Laser Projector) would be needed to cover a large FOV with sufficient illumination. The lens of the original camera from the 3-D scanner has a zoom function that enables an adjustable FOV. If the coverage area were insufficient, replacing the lens with a shorter focal length would fix the problem.

Special cover cases might be required to protect the projector and cameras from the dusty industrial production environment. The cover cases could be made from acrylic sheets with integrated air filtering functions.

Before using the system, a calibration process would be needed to determine the relative angle and position between two cameras. The 3-D scanner manufacturer can provide the targets as well as other calibration instructions. This process would only need to be done once, as long as the cameras were not reinstalled.

During scanning, the concrete would not need to be positioned precisely at the exact location every time. As long as the concrete segment was within the FOV of the scanner, the whole process would function as expected.

Depending on the size of the sample and the required data spatial resolution, a precast concrete segment might require multiple scans. For example, using an SLS with a 3000×4000 pixel camera to scan a 15×20 ft (1.4×1.9 m) area provides 0.06 in. (15.2 mm) spatial resolution (the area divided by the number of pixels). With such resolution, to scan an 80 ft (24

m) long precast concrete object, five scans would be needed ($20 + 15 + 15 + 15 + 15$ ft [$6.1 + 4.6 + 4.6 + 4.6 + 4.6$ m], where the 15 ft lengths include 5 ft [1.5 m] of overlap for scan result–stitching purposes). A well-trained engineer could scan one part and complete the entire inspection process for that part in less than 10 minutes. For large products, additional time might be required to reposition the scanner.

Acknowledgments

This work is supported by PCI via the Daniel P. Jenny Fellowship program. We appreciate the support from Tindall Corp., which made the concrete sample. We also appreciate the constructive suggestions from Roger Becker and the PCI Research and Development Industry Advisory Committee, including Lee Lawrence, chair; Nathan Krause; Nathan Brooks; and Jason Woodard.

References

1. Woo, H., E. Kang, S. Wang, and K. H. Lee. 2002. "A New Segmentation Method for Point Cloud Data." *International Journal of Machine Tools and Manufacture* 42 (2): 167–178. [https://doi.org/10.1016/S0890-6955\(01\)00120-1](https://doi.org/10.1016/S0890-6955(01)00120-1).
2. Kim, M. K., H. Sohn, and C. C. Chang. 2014. "Automated Dimensional Quality Assessment of Precast Concrete Panels Using Terrestrial Laser Scanning." *Automation in Construction* 45: 163–177. <https://doi.org/10.1016/j.autcon.2014.05.015>.
3. Wang, Q., M. K. Kim, S. Yoon, J. C. P. Cheng, and H. Sohn. 2016. "Automated Quality Assessment of Precast Concrete Elements with Geometry Irregularities Using Terrestrial Laser Scanning." *Automation in Construction* 68: 170–182. <https://doi.org/10.1016/j.autcon.2016.03.014>.
4. Kim, M. K., Q. Wang, J. W. Park, J. C. P. Cheng, H. Sohn, C. C. Chang. 2016. "Automated Dimensional Quality Assurance of Full-Scale Precast Concrete Elements Using Laser Scanning and BIM." *Automation in Construction* 72 (2): 102–114. <https://doi.org/10.1016/j.autcon.2016.08.035>.
5. Liu, Y. F., S. Cho, B. F. Spencer, J. S. Fan. 2016. "Concrete Crack Assessment Using Digital Image Processing and 3D Scene Reconstruction." *Journal of Computing in Civil Engineering* 30 (1). [https://doi.org/10.1061/\(ASCE\)CP.1943-5487.0000446](https://doi.org/10.1061/(ASCE)CP.1943-5487.0000446).
6. Kim, M. K., H. Sohn, and C. C. Chang. 2015. "Localization and Quantification of Concrete Spalling Defects Using Terrestrial Laser Scanning." *Journal of Computing in Civil Engineering* 29 (6). [https://doi.org/10.1061/\(ASCE\)CP.1943-5487.0000415](https://doi.org/10.1061/(ASCE)CP.1943-5487.0000415).
7. Wang, Q., M. K. Kim, H. Sohn, and J. C. P. Cheng. 2016. "Surface Flatness and Distortion Inspection of Precast

Concrete Elements Using Laser Scanning Technology.” *Smart Structures and Systems* 18 (3): 601–623. <https://doi.org/10.12989/sss.2016.18.3.601>.

8. Gonzalez-Aguilera, D., J. Gomez-Lahoz, and J. Sanchez. 2008. “A New Approach for Structural Monitoring of Large Dams with a Three-Dimensional Laser Scanner.” *Sensors* 8 (9): 5866–5883. <https://doi.org/10.3390/s8095866>.
9. Riveiro, B., H. González-Jorge, M. Varela, D.V. Jauregui. 2013. “Validation of Terrestrial Laser Scanning and Photogrammetry Techniques for the Measurement of Vertical Underclearance and Beam Geometry in Structural Inspection of Bridges.” *Measurement* 46 (1): 784–794. <https://doi.org/10.1016/j.measurement.2012.09.018>.
10. Oskouie, P., B. Becerik-Gerber, and L. Soibelman. 2016. “Automated Measurement of Highway Retaining Wall Displacements Using Terrestrial Laser Scanners.” *Automation in Construction* 65: 86–101. <https://doi.org/10.1016/j.autcon.2015.12.023>.
11. Fröhlich, C., and M. Mettenleiter. 2004. “Terrestrial Laser Scanning—New Perspectives in 3D Surveying.” *International Archives of Photogrammetry, Remote Sensing and Spatial Information Sciences*. 36 (8 W2): 7–13. <https://www.isprs.org/proceedings/xxxvi/8-w2/FROEHLICH.pdf>.
12. Mikhail, E. M., J. S. Bethel, and J. C. McGlone. 2001. *Introduction to Modern Photogrammetry*. New York: Wiley and Sons.
13. Geng, J. 2011. “Structured-Light 3D Surface Imaging: A Tutorial.” *Advances in Optics and Photonics* 3 (2): 128–160. <https://doi.org/10.1364/AOP.3.000128>.
14. Zhang, Z. Y. 1994. “Iterative Point Matching for Registration of Free-Form Curves and Surfaces.” *International Journal of Computer Vision* 13 (2): 119–152. <https://doi.org/10.1007/BF01427149>.
15. Lague, D., N. Brodu, and J. Leroux. 2013. “Accurate 3D Comparison of Complex Topography with Terrestrial Laser Scanner: Application to the Rangitikei Canyon (N-Z).” *ISPRS Journal of Photogrammetry and Remote Sensing* 82: 10–26. <https://doi.org/10.1016/j.isprsjprs.2013.04.009>.
16. Suzuki, S., and K. Abe. 1985. “Topological Structural-Analysis of Digitized Binary Images by Border Following.” *Computer Vision Graphics and Image Processing* 30 (1): 32–46. [https://doi.org/10.1016/0034-189X\(85\)90016-7](https://doi.org/10.1016/0034-189X(85)90016-7).

Notation

A = spatial coordinate

b = vector

B = height coordinate

C = designed point cloud

D = distance between point cloud and fitted plane

$dist(.)$ = distance function evaluating the difference between two point clouds

H = height of the image (both grayscale and color)

I = RGB image

\tilde{I} = the grayscale image with the shape of $H \times W$

$I_{ij}(1)$ = the intensity of color red

$I_{ij}(2)$ = the intensity of color green

$I_{ij}(3)$ = the intensity of color blue

\tilde{I}_{ij} = the grayscale pixel intensity at position (i,j) in grayscale image

$\tilde{I}_{i-1,j}$ = the intensity of pixel at position $(i-1,j)$ in grayscale image $\tilde{I} \in \mathbb{R}^{H \times W}$

$\tilde{I}_{i+1,j}$ = the intensity of pixel at position $(i+1,j)$ in grayscale image $\tilde{I} \in \mathbb{R}^{H \times W}$

$\tilde{I}_{i,j-1}$ = the intensity of pixel at position $(i,j-1)$ in grayscale image $\tilde{I} \in \mathbb{R}^{H \times W}$

$\tilde{I}_{i,j+1}$ = the intensity of pixel at position $(i,j+1)$ in grayscale image $\tilde{I} \in \mathbb{R}^{H \times W}$

R = rotation matrix

S = scanned point cloud

\tilde{S} = registered scanned point cloud

T = translation matrix

W = width of the image (both grayscale and color)

(x, y) = coordinate of designed center point of metal plates

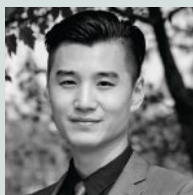
(\hat{x}, \hat{y}) = coordinate of measured center position of metal plates in product

(x_p, y_p, z_p) = coordinate of a single point in the point cloud

β = unknown parameters of the fitted plane

$\hat{\beta}$ = estimated parameters of the fitted plane

About the authors



Rongxuan Wang is a PhD student at the Grado Department of Industrial and Systems Engineering at the Virginia Polytechnic Institute and State University in Blacksburg, Va., specializing in sensing techniques such as three-dimensional scanning, digital image correlation, radiology, and thermography. His research focuses on process monitoring and quality control in smart manufacturing.



Yinan Wang is a PhD student at the Grado Department of Industrial and Systems Engineering at the Virginia Polytechnic Institute and State University. His research interests include data analytics, system pattern recognition, machine learning techniques in material/system design, and advanced manufacturing.



Sonam Devadiga is a master of science student at the Grado Department of Industrial and Systems Engineering at the Virginia Polytechnic Institute and State University.



Issac Perkins is plant manager at Tindall Corp. in Petersburg, Va. His expertise includes operations management, construction management, process improvement, and lean manufacturing.



Zhenyu (James) Kong, PhD, is a professor at the Grado Department of Industrial and Systems Engineering at the Virginia Polytechnic Institute and State University and a fellow of the Institute of Industrial and Systems Engineers (IISE). His research focuses on sensing and analytics for smart manufacturing. Kong is an associate editor for *IEEE Transactions on Automation Science and Engineering* and *IISE Transactions*.



Xiaowei Yue is an assistant professor at the Grado Department of Industrial and Systems Engineering at the Virginia Polytechnic Institute and State University. His research focuses on machine learning and data analytics for advanced manufacturing. Yue is a U.S. Department of Defense Manufacturing Engineering Education Program faculty fellow and an associate editor for *IISE Transactions* and the *Journal of Intelligent Manufacturing*.

Rongxuan Wang and Yinan Wang contributed equally to this paper.

The corresponding author is Xiaowei Yue (xwy@vt.edu).

Abstract

Quality control is a crucial step in the fabrication of precast concrete products. There are three critical quality features: the fabrication consistency of surface finish, the dimensional accuracy of the overall geometry, and the positioning accuracy of the embedded parts. Existing quality control methods rely on tape measures and inspectors' experience, which may lead to measurement inconsistency, operator faults, and safety hazards. This paper proposes an innovative real-time quality inspection system for the three critical quality features. The system first uses a structured-light three-dimensional scanner to capture the surface and geometric data from the precast concrete parts and then calculates and visualizes the deviations by applying specially developed algorithms. In addition, all of the functions are compiled into a graphical user interface that can be easily used by operators without a data analytics background. The system has been tested on a precast concrete sample with five different surface finishes in five regions of the sample, complex geometries, and a variety of embedded parts. The experiment results show that the proposed quality inspection and data analysis system can obtain critical quality information efficiently and accurately.

<https://doi.org/10.15554/pcij66.6-01>

Keywords

Computer-aided design, dimension check, embedded part, machine vision, point cloud data, quality assurance, structured-light scanning three-dimensional scanner, surface quality.

Review policy

This paper was reviewed in accordance with the Precast/Prestressed Concrete Institute's peer-review process.

Reader comments

Please address any reader comments to *PCI Journal* editor-in-chief Tom Klemens at tklemens@pci.org or Precast/Prestressed Concrete Institute, c/o PCI Journal, 8770 W. Bryn Mawr Ave., Suite 1150, Chicago, IL 60631. [f](#)

Axial load limit considerations for 14 in. square prestressed concrete piles

John C. Ryan and Timothy W. Mays

- This research analyzed the moment-curvature response of 14 in. (350 mm) square prestressed concrete piles for varying axial loads. The moment-curvature analysis was performed using structural analysis and design software.
- In previous research, axial load limits were recommended for 14 in. (350 mm) square prestressed concrete piles to prevent loss in moment relative to the first peak moment, which was believed to result in unreliable seismic performance; however, 14 in. piles have a second peak that can vary from 80% of the first peak to over 100% of the first peak moment in most cases.
- Results presented in this paper suggest that more-accurate load limits can be established. In addition, the use of an axial load limit to ensure acceptable seismic performance may not be reasonably justified.

From the 1997 *Uniform Building Code* (UBC)¹ to the 2015 *International Building Code* (IBC),² the required quantity of confinement spiral ρ_s for 14 in. (350 mm) square prestressed concrete piles was capped at 0.021. This upper bound appears to be related to conclusions made by Banerjee et al.,³ who found that 14 in. piles with a quantity of confinement spiral ρ_s greater than 0.020 were expected to have “virtually unlimited curvature capacity.”⁴ The usability of the curvature capacity was recently brought into question by Sritharan et al.⁵ based on results obtained while performing a parametric study of pile ductility. Their research was funded by PCI and aimed at developing updated minimum spiral confinement equations intended for inclusion in the update of the PCI Prestressed Concrete Piling Committee’s “Recommended Practice for Design, Manufacture, and Installation of Prestressed Concrete Piling”⁶ and for possible consideration during future code development deliberations. When reviewing their research results, Sritharan et al. were concerned about the significant drop in moment capacity that occurs when the pile’s cover spalls as part of the pile hinge process. In response, the researchers established a threshold of 40% as the maximum permitted drop in moment capacity that they would permit for 14 in. piles. For cases where the 40% drop was exceeded, published results are not available and the researchers recommended against the use of these piles. Because the percent drop is related to the axial load on the pile, the 40% drop was found by the researchers to occur in some cases when the axial load exceeded $0.2 f'_c A_g$, where f'_c is the specified 28-day concrete strength and A_g is the gross cross-sectional

PCI Journal (ISSN 0887-9672) V. 66, No. 6, November–December 2021.

PCI Journal is published bimonthly by the Precast/Prestressed Concrete Institute, 8770 W. Bryn Mawr Ave., Suite 1150, Chicago, IL 60631.

Copyright © 2021, Precast/Prestressed Concrete Institute. The Precast/Prestressed Concrete Institute is not responsible for statements made by authors of papers in *PCI Journal*. Original manuscripts and discussion on published papers are accepted on review in accordance with the Precast/Prestressed Concrete Institute’s peer-review process. No payment is offered.

area, or 20% of the nominal concrete compressive capacity of the 14 in. prestressed concrete pile.

The 2018 IBC⁷ and the American Concrete Institute's *Building Code Requirements for Structural Concrete (ACI 318-19)* and *Commentary (ACI 318-19R)*⁸ have now adopted the updated confinement equations developed by Sritharan et al.⁵ and have also adopted axial load limits as suggested by these researchers. For seismic design categories C through F, IBC section 1810.3.8.3.4 and ACI 318-19 section 18.13.5.10.6 limit the factored axial load for all square prestressed concrete piles to $0.2 f'_c A_g$. Unfortunately, this limit prohibits the use of some commonly used 14 in. (350 mm) square prestressed concrete pile configurations in areas of moderate to high seismicity. The PCI Prestressed Concrete Piling Committee⁶ has also adopted the updated confinement equations and axial load limits, but this PCI committee publication assumes that performance-based design will be used when the axial load limits are exceeded. Performance-based design of foundation elements is not explicitly codified in the 2018 IBC⁷ and ACI 318-19,⁸ making implementation an arduous task at best, possibly requiring the use of alternative means and methods provisions in some cases.

The basis of the limit on axial load described earlier can be explained with reference to **Fig. 1**, excerpted from Fanous et al.⁹ In Fig. 1, a drop in moment capacity after the first peak moment and subsequent to reaching the second peak moment is evident. The results showed that the percent moment drop

is related to the applied axial load used during moment-curvature analysis. Fanous et al.⁹ suggested that this drop should be limited to approximately 40% of the first peak moment, and that the most effective way of managing the desired limit on the drop in moment was to limit the axial load. Therefore, axial load limits were recommended for the 14 in. (350 mm) pile to prevent loss in moment relative to the first peak moment in excess of approximately 40% based on the pile configurations considered (that is, 14 in. square piles with 2 in. [50.8 mm] cover and round spiral). Avoiding the 40% drop in moment reportedly correlated well with maintaining a response in which the curvature at the initiation of tension cracking ϕ_{cr} is less than the curvature associated with the initiation of unconfined concrete spalling ϕ_{sp} , where strain in the outermost unconfined compression fiber equal to 0.004 is taken as the value that spalling would initiate. According to Sritharan et al.,⁵ "the reason for imposing this condition is that the magnitude of the moment drop due to spalling of the cover concrete is significant when $\phi_{sp} > \phi_{cr}$." Note that current codes do not require the curvature associated with the initiation of unconfined concrete spalling ϕ_{sp} to be greater than the curvature at the initiation of tension cracking ϕ_{cr} for seismic design and that the implementation of this requirement was selected to attempt to control the moment drop associated with seismic hinging.

It should be noted that Fanous et al.⁹ do not appear to define or study the rationale for the concern or to determine if the moment drop would actually result in poor performance of the subject piling. Rather, the authors note that larger moment

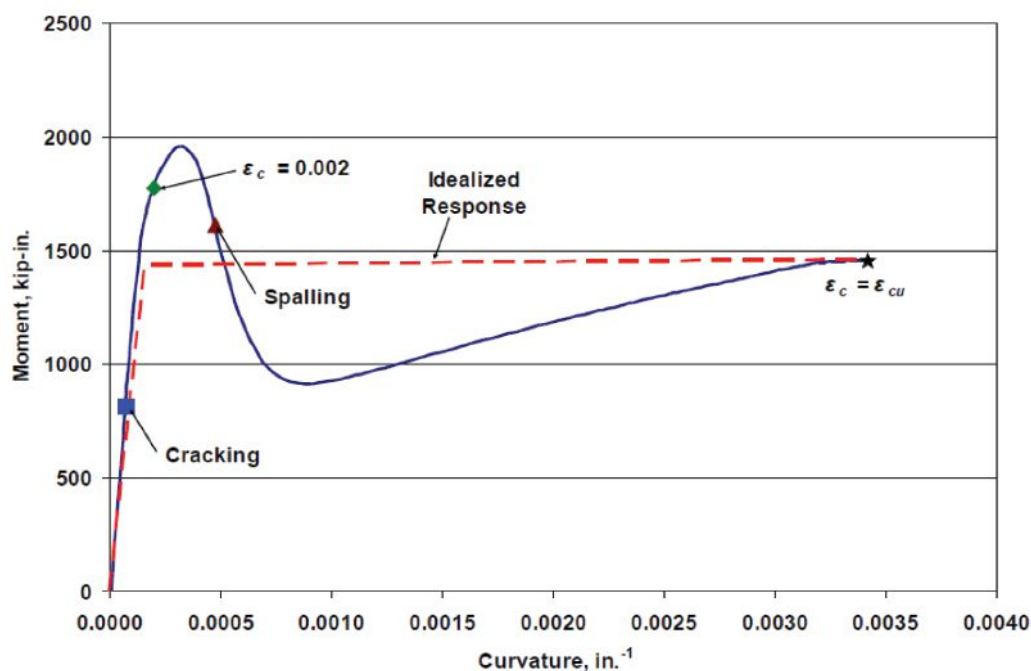


Figure 1. Moment-curvature relationship for a 14 in. square pile with specified concrete strength f'_c of 6000 psi, effective prestress f_{pc} of 1200 psi, and a 0.2 axial load ratio. Source: Reproduced by permission from Fanous et al. (2010, Fig. 3.30). Note: f'_c = specified 28-day strength of the concrete; f_{pc} = effective prestress in the pile; ϵ_c = strain in concrete; ϵ_{cu} = ultimate strain in concrete. 1 in. = 25.4 mm; 1 kip-in. = 0.113 kN-m; 1 psi = 6.895 kPa.

drops were deemed to be “unacceptable for piles in seismic regions” and “the stability of the pile experiencing significant moment drop may not be dependable.” The concern about moment drop expressed by the previous researchers was an opinion based on research related to Eurocode and not U.S. codes and standards. *Seismic Design of Concrete Buildings to Eurocode 8*¹⁰ discusses the moment drop issue and states that the ultimate ductility capacity is typically taken as the ductility capacity when the moment drops 20% from its peak value. This makes sense for moment-curvature analysis (that is, moment rotation results) where the moment is continuing to decline down to an unpredictable value at failure. **Figure 2** shows that typical small diameter auger-cast piles may warrant such consideration; however, as shown in the same figure, 14 in. (350 mm) square prestressed concrete piles are not approaching an impending failure mechanism and do not perform as assumed by the Eurocode provision. The Eurocode-related publication recognizes that this may be the case when it refers to the ductility capacity related to the 20% moment drop as follows: “It may be assumed that it represents the flexural deformation capacity of a member. Actually, a member has additional capacity beyond the NC (Near Collapse) limit state. In principle, it is possible to model the moment-rotation relation beyond the ultimate rotation of the plastic hinge θ_u ; however, there is lack of data on the descending branch of the moment-rotation curve. Moreover, simulating the behavior beyond the NC limit state usually has only very limited practical value.”

As will be discussed in the results section of this paper, 14 in. (350 mm) prestressed concrete piles have a second peak that can be shown to vary from 80% of the first peak to over 100% of the first peak moment in most cases. U.S. codes and standards committees are aware of the benefits and stability of the second peak moment that occurs for prestressed piles used as lateral-force-resisting elements and these committees have already established a vetted means to account for the first moment drop without applying an artificial axial load limit.

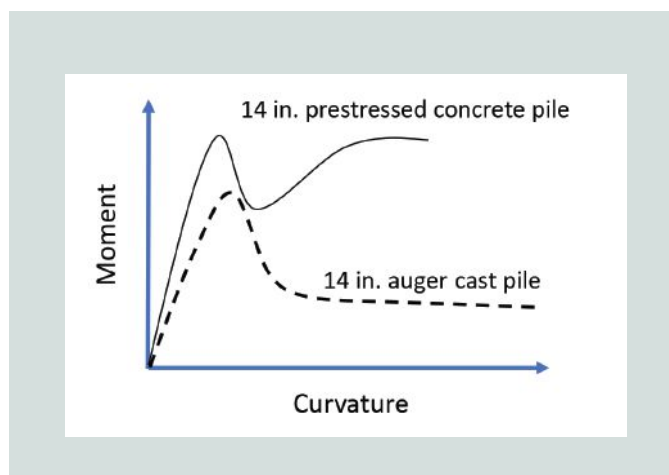


Figure 2. Comparison of typical moment-curvature relationships for a 14 in. square prestressed concrete pile and 14 in. auger cast pile with $0.2f'_c A_g$ applied axial load in both cases. Note: A_g = gross cross-sectional area; f'_c = specified 28-day strength of the concrete. 1 in. = 25.4 mm.

Current practice in the United States

It is well established in U.S. codes and standards that moment-curvature curves for prestressed concrete piles are very stable and unique in their response characteristics. Although building standards such as American Society of Civil Engineers (ASCE) Structural Engineering Institute's (SEI's) *Seismic Evaluation and Retrofit of Existing Buildings* ASCE/SEI 41-17¹¹ present recommendations on modeling building elements with moment drops leading to failure, building piles are designed to respond elastically to the design earthquake and thus modeling prestressed concrete pile ductility response is not a primary focus of these standards. On the other hand, in California, where seismic design is paramount, prestressed concrete pile ductility modeling provisions have been incorporated into the California Building Code through “Marine Oil Terminal Engineering and Maintenance Standards.”¹² These provisions apply when prestressed concrete piles are the entire lateral-force-resisting system for marine oil terminal pier and wharf structures. Regarding moment-curvature analysis and ductility modeling of prestressed concrete piles, the California Building Code provisions are identical to what is presented in ASCE 61-14¹³ for piers and wharfs and in *Port of Long Beach Wharf Design Criteria*.¹⁴ Unlike the philosophy for building piles, because the moment-curvature response of pier piles is critical to the intended ductility performance of the entire structure, related codes and standards must address pile ductility limits as part of their criteria. The same is true for codes and standards related to bridge design in areas of high seismicity.

*Port of Long Beach Wharf Design Criteria*¹⁴ provides an overview of how moment-curvature response is conservatively modeled for prestressed concrete piles. **Figure 3** is a generalized moment-curvature plot, which is useful in describing the Port of Long Beach¹⁴ model. It should be noted that a fictitious axial load limit is not established. Rather, the

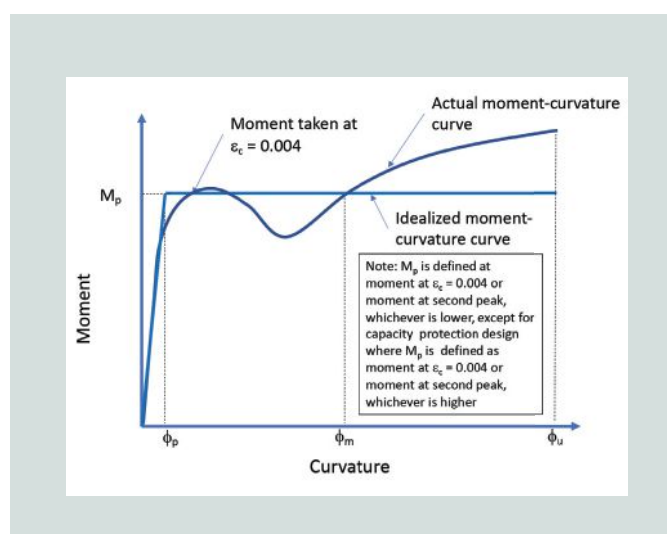


Figure 3. Typical moment-curvature model for prestressed concrete pile. Source: Adapted from Port of Long Beach (2015). Note: M_p = plastic or maximum moment on the bilinear idealized moment-curvature curve; ϵ_c = strain in concrete; ϕ_m = maximum curvature; ϕ_p = plastic curvature; ϕ_u = ultimate curvature.

California Building Code,¹² ASCE 61-14,¹³ and *Port of Long Beach Wharf Design Criteria*¹⁴ use energy dissipation penalties by reducing the moment and not the ultimate curvature. Specifically, if the second peak moment exceeds the first peak moment, the moment-curvature curve is taken as the bilinear curve shown with a maximum moment M_p associated with the first peak moment on the curve. If the second peak moment is less than the first peak moment, the moment-curvature curve is taken as the bilinear curve shown but with a maximum moment M_p equal to the second peak moment on the curve. In other words, if a moment drop occurs and the moment-curvature curve does not return to a (second peak) maximum moment equal to or greater than the value associated with the first peak, the bilinear moment-curvature curve shall be taken with a maximum moment equal to the second peak moment. This simple approach penalizes the design by dissipating less energy (that is, energy dissipation is related to the area under the moment-curvature curve), which also results in a larger displacement demand for the structure. The larger displacement demand yields larger second-order effects as well; however, it should be noted that the ultimate curvature capacity ϕ_u is not decreased. In addition, as previously stated, axial load limits are not established, which is contrary to recommendations from Fanous et al.⁹ To avoid any confusion, it should be noted that performance-based design typically does use lateral load drops exceeding 20% as the limit when using pushover analysis for the lateral-force-resisting system. This limit is not relevant to the topic addressed in this paper as it is meant to prevent progressive collapse of the lateral-force-resisting system caused by excessive second-order effects (that is, axial load P and pile deflection Δ , or $P-\Delta$, effects).

Bridge codes and standards use performance-based design approaches that are very similar to those used in the pier and wharf industry, with notable variations. For example,

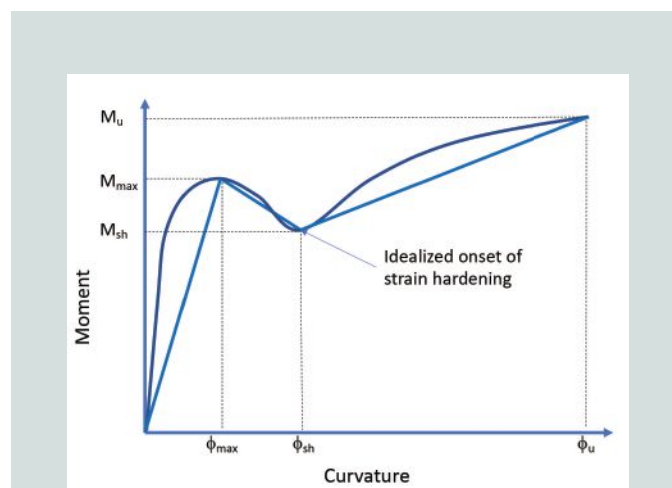


Figure 4. Trilinear moment-curvature model for prestressed concrete pile. Source: Adapted from South Carolina Department of Transportation (2008). Note: M_{max} = maximum moment; M_{sh} = moment at strain hardening; M_u = ultimate moment; ϕ_{max} = maximum curvature; ϕ_{sh} = curvature at strain hardening; ϕ_u = ultimate curvature.

in addition to simple bilinear moment-curvature models for prestressed concrete piles often used in the industry, codes and standards such as the South Carolina Department of Transportation *SCDOT Seismic Design Criteria*¹⁵ also allow the engineer to directly model the trilinear behavior of the pile to account for moment loss (**Fig. 4**). These models may be considered more accurate in regard to capturing the maximum and minimum moments of the moment-curvature curve and global stability of the structure is more accurately accounted for when trilinear models are used. In addition to trilinear models, modern software allows for moment-curvature curves made of many points and, in these cases, not only strength but also stiffness is more accurately represented.

Procedure

The primary focus of this study was to analyze through modeling the moment-curvature response of 14 in. (350 mm) square prestressed concrete piles with varying axial loads exceeding $0.2 f'_c A_g$.

Both round and square spiral configurations, enclosing round and square strand patterns respectively, with 2 and 3 in. (50.8 and 76.2 mm) of cover were considered. Standard use in the industry limits the scope of the study to six- and eight-strand configurations with effective prestress after losses between 700 and 1200 psi (4830 and 8270 kPa). Concrete compressive strengths between 5000 and 8000 psi (34,500 and 55,200 kPa) were considered. Prestressing strands were assumed to conform to ASTM A416.¹⁵ Plain wire reinforcement was assumed to conform to ASTM A1064.¹⁶ In this study, and as required by ASTM A1064, wire reinforcement was assumed to have a yield stress of 65 ksi (448 MPa) and an ultimate stress of 75 ksi (517 MPa). For the purposes of this study, nominal rather than expected material properties were assumed.

Performance-based design codes often require the use of expected material properties when performing moment-curvature analyses. All moment-curvature analysis results presented in this report were obtained using SAP2000, a structural analysis and design software. SAP2000 has its own built-in material modeling and moment-curvature analysis methodologies that are well recognized by both academic and industry practice. Prestressing strands and wire reinforcement are modeled using nonlinear material models. Unconfined and confined concrete are modeled using the model from Mander et al.¹⁸ (**Fig. 5**). Readers seeking more information regarding material models considered in this paper are referred to Ryan and Mays.¹⁹

A distinction should be noted between analysis tools used for the research presented in this paper and those used in the prior study. The analysis program chosen by Fanous et al.⁹ had element limitations and, therefore, the research team created special elements to attempt to model the full cross-sectional behavior. In addition, the geometries considered were limited to round spiral configurations with 2 in.

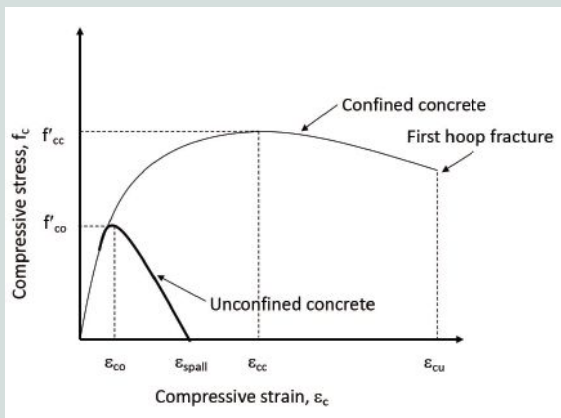


Figure 5. Mander's model for unconfined and confined concrete. Source: Adapted from Mander et al. (1988). Note: f'_{cc} = ultimate stress in confined concrete; f'_{co} = stress in unconfined concrete; ϵ_{cc} = strain in confined concrete at peak stress; ϵ_{co} = strain in unconfined concrete at peak stress; ϵ_{cu} = ultimate strain in concrete; ϵ_{spall} = strain at unconfined concrete spalling.

(50.8 mm) of cover. Square confinement and square strand configurations were not considered by the previous research. The previous research authors do not suggest that fiber models created for their study were validated for the correct number of fiber elements nor compared with other software used in the industry to validate the accuracy of the moment drop calculated during the study. Fanous et al.⁹ compared results obtained from the two program options used in the previous research (**Fig. 6**). The authors state that the figure shows “fairly similar behavior confirming the accuracy of both programs.” This appears to be true for ultimate curva-

ture, but when comparing the values for initial peak moment and moment after initial loss in strength, the analyzed values differ by a factor of approximately 1.5 and 2.0, respectively. Because conclusions related to applying axial load limits are drawn almost entirely from these initial portions of the moment-curvature response, greater scrutiny of the model is warranted.

All moment-curvature analysis results presented in this paper were obtained using section designer within SAP2000. No elements were developed by the research team to model the pile cross sections, as SAP2000 has required element models available within the program, and these elements have been fully tested for use as part of the subject research.

Figure 7 shows a typical pile cross section modeled in SAP2000. Prior to performing the parametric study, fiber models with rectangular and cylindrical configurations were tested for convergence with exact integration solutions.

Figures 8 and 9 show typical fiber element configurations tested during the convergence study. It was determined that in all cases, 30 × 30 rectangular and 30 × 20 cylindrical configurations always matched the exact integration solution. The cylindrical fiber configuration required fewer elements and was thus favored for circular confinement sections. The rectangular fiber configuration was favored for square confinement sections.

Parametric study parameters

Using the material models discussed in the previous section for the prestressing strand, spiral reinforcement, unconfined concrete, and confined concrete, a moment-curvature-related parametric study of 14 in. (350 mm) square prestressed pile

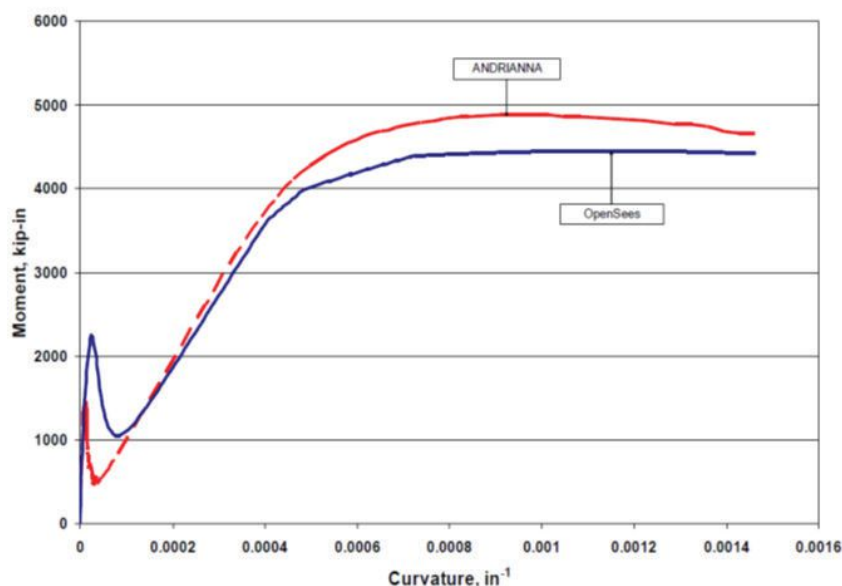


Figure 6. A comparison of moment-curvature response results obtained from two separate programs. Source: Reproduced by permission from Fanous et al. (2010, Fig. 3.11). Note: 1 in. = 25.4 mm; 1 kip-in. = 0.113 kN-m.

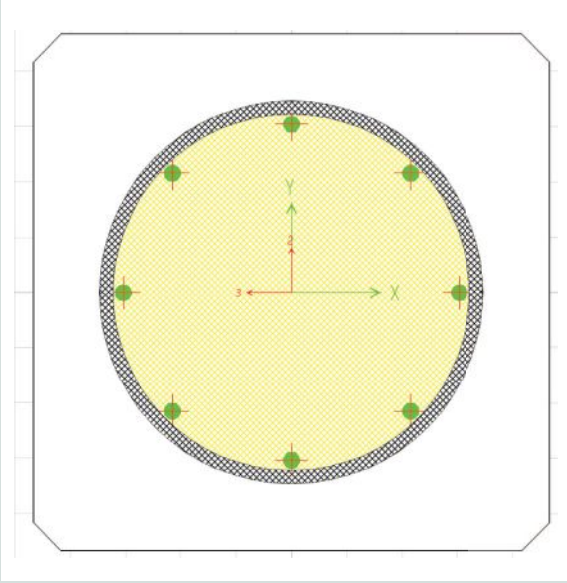


Figure 7. Typical cross-sectional model showing strands, spiral, confined concrete, and unconfined concrete properties in SAP2000.

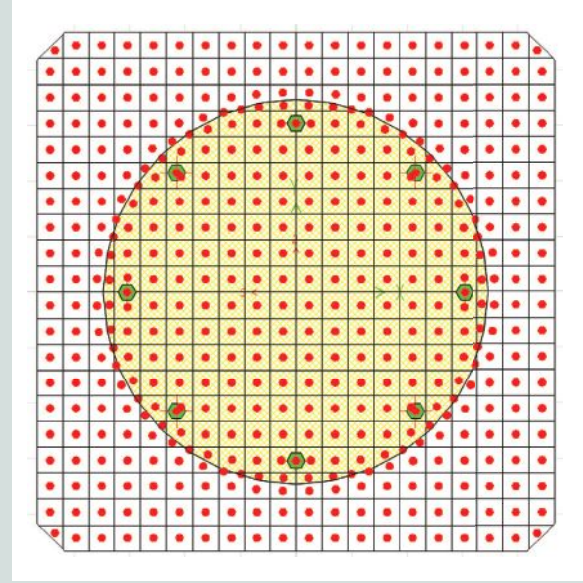


Figure 8. Typical rectangular fiber model (20 × 20 shown).

configurations was performed. The study was limited to pile cross sections and initial prestress levels commonly used in the United States. The following parameters were considered:

- normalweight concrete with concrete compressive strength f'_c between 5000 and 8000 psi (34,500 and 55,200 kPa)
- concrete cover to the spiral reinforcement between 2 and 3 in. (50.8 and 76.2 mm)
- effective prestress after losses f_{pc} between 700 and 1200 psi (4830 and 8270 kPa)
- axial load P between $0.2 f'_c A_g$ and $0.35 f'_c A_g$
- six- and eight-strand circular configurations (with circular spiral confinement wire)
- six- and eight-strand square configurations (with square confinement wire)

The amount of spiral reinforcement modeled was determined using the prescriptive requirements of the PCI Prestressed Concrete Piling Committee.⁶ For piles using a circular prestressed reinforcement configuration, the quantity of confinement spiral ρ_s provided was taken as:

$$\rho_s = 0.06 \left(\frac{f'_c}{f_{yh}} \right) \left(2.8 + \frac{1.25P}{0.53 f'_c A_g} \right) \quad (1)$$

where

f_{yh} = yield strength of spiral reinforcement

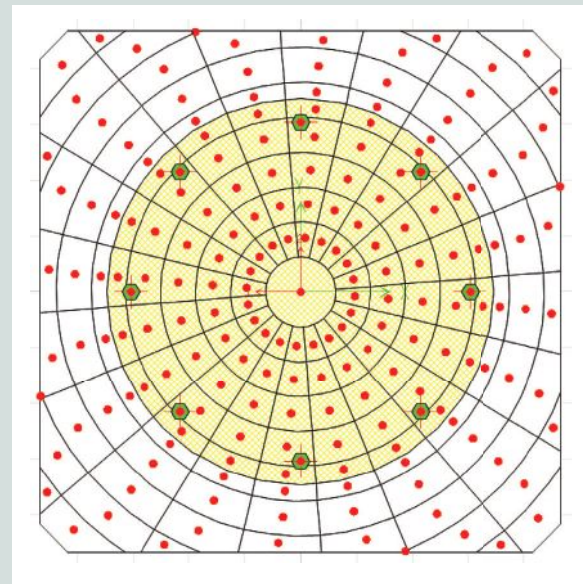


Figure 9. Typical cylindrical fiber model (20 × 10 shown).

For piles with a square prestressed reinforcement configuration, the total cross-sectional area of transverse reinforcement provided separately in each direction, including crossies where applicable A_{sh} was taken as:

$$A_{sh} = 0.04 s h_c \left(\frac{f'_c}{f_{yh}} \right) \left(2.8 + \frac{1.25P}{0.53 f'_c A_g} \right) \quad (2)$$

where

s = longitudinal spacing of the transverse steel

h_c = confined concrete side dimension defined by transverse steel dimension

W10 and W12 wire were used exclusively for spiral wire during the study. Spacing of the spiral was used to proportion the quantity of confinement spiral ρ_s and the total cross-sectional area of transverse reinforcement A_{sh} to match minimum prescriptive values calculated using Eq. (1) and (2). Spacing of the spiral was also verified to be less than the maximum recommended spacing presented in the PCI Prestressed Concrete Piling Committee's recommended practice,⁶ such that the spacing for all models did not exceed the minimum of:

- $\frac{1}{5}$ of the smallest pile dimension
- six strand diameters
- 6 in. (152 mm)

As previously discussed, axial load limits were recommended by Fanous et al.⁹ for the 14 in. (350 mm) pile to prevent loss in moment relative to the first peak moment in excess of approximately 40% based on pile configurations considered (that is, 14 in. square piles with 2 in. [50.8 mm] cover and round spiral). As such, this paper presents the results of the parametric study as related to the drop in moment after the first peak moment occurs during moment-curvature analysis. This section of the paper accepts the premise that the 40% moment drop is actually a concern and presents the results of a thorough study (as recommended by Fanous et al.⁹) of axial loads and pile geometries related to 14 in. prestressed concrete piles in seismic areas as needed to provide designers a practical response to the new and arbitrary axial load limit established by the previous researchers.

Because the moment drop, or percent moment drop, after the first peak moment is the critical data point to be recorded during this study, it was recorded for every moment-curvature analysis performed. The second peak moment is also a data point of interest because the second peak moment often returns close to the initial peak moment value. The second peak moment ensures section stability and seismic energy dissipation. More importantly, the second peak should make the initial moment drop less of a concern as the descending branch of the moment-curvature curve does not continue downward in an unreliable manner with limited energy dissipation capability. For the reasons discussed above, the research team has recorded the three moment values for all moment-curvature analyses (**Fig. 10**).

The curvature values associated with the three moment values were not recorded during the study; however, each analysis was checked to ensure that the available curvature ductility capacity was greater than 18 for all cases as required by Fanous et al.⁹ and the PCI Prestressed Concrete Piling Committee.⁶

For discussion of the results presented in this chapter, it is

convenient to define two moment ratios: percent drop and percent return.

Percent drop $\%Drop$ is the ratio of the minimum moment that occurs after $M_{peak,1}$ on the moment-curvature curve M_{drop} to the first maximum moment that occurs on the moment-curvature curve $M_{peak,1}$ and percent return $\%Return$ is the ratio of the second maximum moment that occurs after M_{drop} on the moment-curvature curve $M_{peak,2}$ to the first maximum moment that occurs on the moment-curvature curve $M_{peak,1}$. Percent drop $\%Drop$ was used to compare the SAP2000 model results described herein with results from Fanous et al.⁹ The previous study limited $\%Drop$ to no less than 60%. In other words, if the first maximum moment that occurs on the moment-curvature curve $M_{peak,1}$ was reduced by more than 40%, the combination of pile cross section, prestress, and axial load was determined to be unsuitable and $\%Return$ was not reported. Recommended axial load limits were, in part, calibrated based on that criterion. Based on $\%Drop$, this study showed that increased axial load limits can be validated using an improved SAP2000 model while remaining consistent with methodology used by Fanous et al.⁹ The SAP2000 model contains more realistic and industry-proven fiber elements than those used in the previous study. SAP2000 is also used commercially by practicing engineers to model prestressed pile hinging.

Percent return $\%Return$ is the measure of proximity to the first peak moment that a pile can be expected to achieve during stable hinging behavior. Percent return $\%Return$ is less than 1.0 when the second peak moment is less than the first peak moment. Percent return $\%Return$ is equal to 1.0 when the second peak moment is equal to the first peak moment. Percent return $\%Return$ is greater than 1.0 when the pile second peak moment is greater than the first peak moment. Percent return $\%Return$ has been included as a basis for possible modification of the previously accepted methodology for axial load limit.

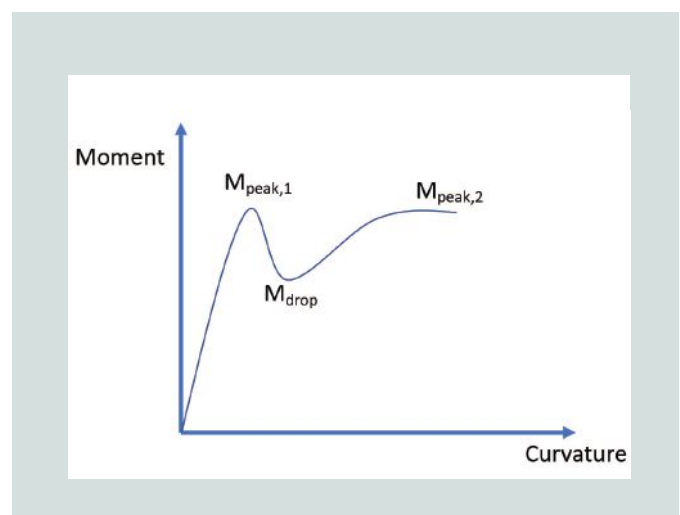


Figure 10. Three data points recorded during moment-curvature analysis. Note: M_{drop} = minimum moment that occurs after $M_{peak,1}$ on the moment-curvature curve; $M_{peak,1}$ = first maximum moment that occurs on the moment-curvature curve; $M_{peak,2}$ = second maximum moment that occurs after M_{drop} on the moment-curvature curve.

Results: 14 in. square piles with 2 in. cover

For this study, the aim of the research team was to perform a moment-curvature-related parametric study of 14 in. (350 mm) prestress pile configurations limited to pile cross sections and initial prestress levels commonly used in the United States. For each configuration considered, the first maximum moment that occurs on the moment-curvature curve $M_{peak,1}$, the minimum moment that occurs after $M_{peak,1}$ on the moment-curvature curve M_{drop} , and the second maximum moment that occurs after M_{drop} on the moment-curvature curve $M_{peak,2}$ were recorded. **Tables 1** through **10** present the results provided by the moment-curvature analysis for the 160 primary cases considered in this study.

A few practical points should be made regarding typical 14 in. (350 mm) piles. In practical design, the strands are typically pretensioned to 75% of the ultimate strength of prestressing strands f_{pu} and the piles normally exhibit losses around 15%. The baseline cases for this study consist of the most common pile strand configurations used in practice, which are the six-strand and eight-strand patterns, using ½ in. (12.7 mm) diameter strands (cross-sectional area of spiral reinforcement A_{sp} is 0.153 in.² [98.7 mm²] per strand). Losses for the baseline cases are assumed to be 15%. The six-strand baseline case has an effective prestress very close to the 700 psi (4830 kPa) minimum value considered in the study.

Similarly, the eight-strand baseline case has an effective prestress very close to the 1200 psi (8270 kPa) maximum value considered. The data presented in Tables 1 through 10 are for the bounds considered in the study; however, it should be noted that the results from the baseline cases did not noticeably change from the adjacent upper- and lower-bound results; as such, and to avoid reader confusion, the results for the baseline cases are not presented as separate cases in this paper. It should be noted that 1200 psi effective prestress, as defined in the maximum prestress cases, would be difficult to achieve in practice using the ½ in. strand configurations discussed earlier and accounting for losses. There may be occasions where adding strand, using different strand sizes, and reducing the initial tension in the strands from 75% of ultimate strength of the prestressing strand f_{pu} could achieve a performance objective, however, the designer should provide clear instructions for the producer to avoid confusion and increased costs associated with additional steel.

Based solely on the results presented in Tables 1 through 4, it can be argued that for circular spiral and strand configurations, $0.25 f'_c A_g$ is a more appropriate axial load limit when the effective prestress is near 1200 psi (8270 kPa). For circular spiral and strand configurations, $0.30 f'_c A_g$ is a more appropriate axial load limit when the effective prestress is near 700 psi (4830 kPa), at least up to a compressive concrete strength f'_c of 7000 psi (48,300 kPa).

Table 1. Results of moment-curvature analysis for 14 in. square pile with eight strands, circular W10 confinement, 0.5 in. diameter strand, and 1200 psi effective prestress

f'_c , ksi	Multiplier $f'_c A_g$	$M_{peak,1}$, kip-in.	M_{drop} , kip-in.	$M_{peak,2}$, kip-in.	%Drop	%Return
5	0.20	1650	1120	1490	68	90
6	0.20	1890	1270	1630	67	86
7	0.20	2240	1350	1720	60	77
8	0.20	2460	1490	1860	61	76
5	0.25	1680	1090	1510	65	90
6	0.25	1940	1230	1660	63	86
7	0.25	2280	1310	1760	57	77
8	0.25	2530	1450	1900	57	75
5	0.30	1700	1020	1500	60	88
6	0.30	1970	1170	1670	59	85
7	0.30	2270	1230	1770	54	78
8	0.30	2540	1370	1900	54	75
5	0.35	1700	950	1500	56	88
6	0.35	1970	1100	1660	56	84
7	0.35	2240	1120	1750	50	78
8	0.35	2500	1240	1900	50	76

Note: A_g = gross cross-sectional area; f'_c = specified 28-day strength of the concrete; M_{drop} = minimum moment that occurs after $M_{peak,1}$ on the moment-curvature curve; $M_{peak,1}$ = first maximum moment that occurs on the moment-curvature curve; $M_{peak,2}$ = second maximum moment that occurs after M_{drop} on the moment-curvature curve; %Drop = ratio of M_{drop} to $M_{peak,1}$; %Return = ratio of $M_{peak,2}$ to $M_{peak,1}$; 1 in. = 25.4 mm; 1 kip-in. = 0.113 kN-m; 1 psi = 6.895 kPa; 1 ksi = 6.895 MPa; W10 = MW65.

Table 2. Results of moment-curvature analysis for 14 in. square pile with eight strands, circular W10 confinement, 0.5 in. diameter strand, and 700 psi effective prestress

f'_c , ksi	Multiplier $f'_c A_g$	$M_{peak,1}$, kip-in.	M_{drop} , kip-in.	$M_{peak,2}$, kip-in.	%Drop	%Return
5	0.20	1700	1150	1500	68	88
6	0.20	2030	1260	1640	62	81
7	0.20	2140	1440	1780	67	83
8	0.20	2350	1570	1900	67	81
5	0.25	1730	1130	1540	65	89
6	0.25	2050	1220	1660	60	81
7	0.25	2210	1420	1820	64	82
8	0.25	2440	1540	1950	63	80
5	0.30	1730	1080	1540	62	89
6	0.30	2050	1160	1670	57	81
7	0.30	2270	1360	1830	60	81
8	0.30	2510	1490	1980	59	79
5	0.35	1740	1010	1520	58	87
6	0.35	2020	1050	1650	52	82
7	0.35	2280	1280	1810	56	79
8	0.35	2540	1400	1950	55	77

Note: A_g = gross cross-sectional area; f'_c = specified 28-day strength of the concrete; M_{drop} = minimum moment that occurs after $M_{peak,1}$ on the moment-curvature curve; $M_{peak,1}$ = first maximum moment that occurs on the moment-curvature curve; $M_{peak,2}$ = second maximum moment that occurs after M_{drop} on the moment-curvature curve; %Drop = ratio of M_{drop} to $M_{peak,1}$; %Return = ratio of $M_{peak,2}$ to $M_{peak,1}$. 1 in. = 25.4 mm; 1 kip-in. = 0.113 kN-m; 1 psi = 6.895 kPa; 1 ksi = 6.895 MPa; W10 = WM65.

Table 3. Results of moment-curvature analysis for 14 in. square pile with six strands, circular W10 confinement, 0.5 in. diameter strand, and 1200 psi effective prestress

f'_c , ksi	Multiplier $f'_c A_g$	$M_{peak,1}$, kip-in.	M_{drop} , kip-in.	$M_{peak,2}$, kip-in.	%Drop	%Return
5	0.20	1610	990	1210	61	75
6	0.20	1850	1140	1350	62	73
7	0.20	2070	1270	1470	61	71
8	0.20	2290	1400	1600	61	70
5	0.25	1650	960	1240	58	75
6	0.25	1900	1120	1390	59	73
7	0.25	2150	1250	1510	58	70
8	0.25	2390	1380	1660	58	69
5	0.30	1660	900	1230	54	74
6	0.30	1900	1060	1390	56	73
7	0.30	2200	1190	1520	54	69
8	0.30	2450	1330	1670	54	68
5	0.35	1650	820	1190	50	72
6	0.35	1930	980	1360	51	70
7	0.35	2200	1110	1490	50	68
8	0.35	2470	1230	1640	50	66

Note: A_g = gross cross-sectional area; f'_c = specified 28-day strength of the concrete; M_{drop} = minimum moment that occurs after $M_{peak,1}$ on the moment-curvature curve; $M_{peak,1}$ = first maximum moment that occurs on the moment-curvature curve; $M_{peak,2}$ = second maximum moment that occurs after M_{drop} on the moment-curvature curve; %Drop = ratio of M_{drop} to $M_{peak,1}$; %Return = ratio of $M_{peak,2}$ to $M_{peak,1}$. 1 in. = 25.4 mm; 1 kip-in. = 0.113 kN-m; 1 psi = 6.895 kPa; 1 ksi = 6.895 MPa; W10 = MW65.

Table 4. Results of moment-curvature analysis for 14 in. square pile with six strands, circular W10 confinement, 0.5 in. diameter strand, and 700 psi effective prestress

f'_c , ksi	Multiplier $f'_c A_g$	$M_{peak,1}$, kip-in.	M_{drop} , kip-in.	$M_{peak,2}$, kip-in.	%Drop	%Return
5	0.20	1640	1050	1250	64	76
6	0.20	1870	1190	1380	64	74
7	0.20	2090	1320	1500	63	72
8	0.20	2350	1540	1540	66	66
5	0.25	1680	1020	1280	61	76
6	0.25	1930	1180	1430	61	74
7	0.25	2180	1310	1560	60	72
8	0.25	2460	1320	1590	54	65
5	0.30	1700	980	1290	58	76
6	0.30	1970	1140	1440	58	73
7	0.30	2200	1270	1580	58	72
8	0.30	2500	1260	1600	50	64
5	0.35	1700	920	1280	54	75
6	0.35	1980	1060	1430	54	72
7	0.35	2250	1190	1550	53	69
8	0.35	2470	1140	1570	46	64

Note: A_g = gross cross-sectional area; f'_c = specified 28-day strength of the concrete; M_{drop} = minimum moment that occurs after $M_{peak,1}$ on the moment-curvature curve; $M_{peak,1}$ = first maximum moment that occurs on the moment-curvature curve; $M_{peak,2}$ = second maximum moment that occurs after M_{drop} on the moment-curvature curve; %Drop = ratio of M_{drop} to $M_{peak,1}$; %Return = ratio of $M_{peak,2}$ to $M_{peak,1}$; 1 in. = 25.4 mm; 1 kip-in. = 0.113 kN-m; 1 psi = 6.895 kPa; 1 ksi = 6.895 MPa; W10 = MW65.

Table 5. Results of moment-curvature analysis for 14 in. square pile with eight strands, square W12 confinement, 0.5 in. diameter strand, and 1200 psi effective prestress

f'_c , ksi	Multiplier $f'_c A_g$	$M_{peak,1}$, kip-in.	M_{drop} , kip-in.	$M_{peak,2}$, kip-in.	%Drop	%Return
5	0.20	1840	1330	1880	72	102
6	0.20	2070	1490	1970	72	95
7	0.20	2320	1680	2130	72	92
8	0.20	2540	1830	2230	72	88
5	0.25	1860	1300	1890	70	102
6	0.25	2110	1470	1940	70	92
7	0.25	2360	1670	2180	71	92
8	0.25	2590	1810	2210	70	85
5	0.30	1840	1250	1850	68	101
6	0.30	2100	1410	1900	67	90
7	0.30	2360	1630	2130	69	90
8	0.30	2600	1770	2130	68	82
5	0.35	1790	1160	1830	65	102
6	0.35	2060	1310	1850	64	90
7	0.35	2320	1540	2070	66	89
8	0.35	2570	1660	2060	65	80

Note: A_g = gross cross-sectional area; f'_c = specified 28-day strength of the concrete; M_{drop} = minimum moment that occurs after $M_{peak,1}$ on the moment-curvature curve; $M_{peak,1}$ = first maximum moment that occurs on the moment-curvature curve; $M_{peak,2}$ = second maximum moment that occurs after M_{drop} on the moment-curvature curve; %Drop = ratio of M_{drop} to $M_{peak,1}$; %Return = ratio of $M_{peak,2}$ to $M_{peak,1}$; 1 in. = 25.4 mm; 1 kip-in. = 0.113 kN-m; 1 psi = 6.895 kPa; 1 ksi = 6.895 MPa; W12 = MW77.

Table 6. Results of moment-curvature analysis for 14 in. square pile with eight strands, square W12 confinement, 0.5 in. diameter strand, and 700 psi effective prestress

f'_c , ksi	Multiplier $f'_c A_g$	$M_{peak,1}$, kip-in.	M_{drop} , kip-in.	$M_{peak,2}$, kip-in.	%Drop	%Return
5	0.20	1840	1450	1890	79	103
6	0.20	2050	1610	1980	79	97
7	0.20	2260	1780	2170	79	96
8	0.20	2450	1910	2240	78	91
5	0.25	1860	1420	1900	76	102
6	0.25	2090	1580	1920	76	92
7	0.25	2320	1780	2180	77	94
8	0.25	2540	1900	2180	75	86
5	0.30	1850	1400	1860	76	101
6	0.30	2110	1530	1920	73	91
7	0.30	2360	1750	2140	74	91
8	0.30	2590	1870	2160	72	83
5	0.35	1840	1320	1850	72	101
6	0.35	2110	1470	1890	70	90
7	0.35	2370	1690	2110	71	89
8	0.35	2600	1800	2100	69	81

Note: A_g = gross cross-sectional area; f'_c = specified 28-day strength of the concrete; M_{drop} = minimum moment that occurs after $M_{peak,1}$ on the moment-curvature curve; $M_{peak,1}$ = first maximum moment that occurs on the moment-curvature curve; $M_{peak,2}$ = second maximum moment that occurs after M_{drop} on the moment-curvature curve; %Drop = ratio of M_{drop} to $M_{peak,1}$; %Return = ratio of $M_{peak,2}$ to $M_{peak,1}$. 1 in. = 25.4 mm; 1 kip-in. = 0.113 kN-m; 1 psi = 6.895 kPa; 1 ksi = 6.895 MPa; W12 = MW77.

Table 7. Results of moment-curvature analysis for 14 in. square pile with six strands (strong axis), square W12 confinement, 0.5 in. diameter strand, and 1200 psi effective prestress

f'_c , ksi	Multiplier $f'_c A_g$	$M_{peak,1}$, kip-in.	M_{drop} , kip-in.	$M_{peak,2}$, kip-in.	%Drop	%Return
5	0.20	1650	1150	1560	70	95
6	0.20	1890	1300	1660	69	88
7	0.20	2130	1480	1780	69	84
8	0.20	2350	1610	1870	69	80
5	0.25	1680	1120	1670	67	99
6	0.25	1940	1280	1790	66	92
7	0.25	2200	1490	1920	68	87
8	0.25	2430	1620	2040	67	84
5	0.30	1680	1060	1800	63	107
6	0.30	1950	1230	1930	63	99
7	0.30	2210	1450	2080	66	94
8	0.30	2460	1590	2200	65	89
5	0.35	1650	980	1860	59	113
6	0.35	1910	1120	1890	59	99
7	0.35	2190	1360	2120	62	97
8	0.35	2440	1490	2130	61	87

Note: A_g = gross cross-sectional area; f'_c = specified 28-day strength of the concrete; M_{drop} = minimum moment that occurs after $M_{peak,1}$ on the moment-curvature curve; $M_{peak,1}$ = first maximum moment that occurs on the moment-curvature curve; $M_{peak,2}$ = second maximum moment that occurs after M_{drop} on the moment-curvature curve; %Drop = ratio of M_{drop} to $M_{peak,1}$; %Return = ratio of $M_{peak,2}$ to $M_{peak,1}$. 1 in. = 25.4 mm; 1 kip-in. = 0.113 kN-m; 1 psi = 6.895 kPa; 1 ksi = 6.895 MPa; W12 = MW77.

Table 8. Results of moment-curvature analysis for 14 in. square pile with six strands (strong axis), square W12 confinement, 0.5 in. diameter strand, and 700 psi effective prestress

f'_c , ksi	Multiplier $f'_c A_g$	$M_{peak,1}$, kip-in.	M_{drop} , kip-in.	$M_{peak,2}$, kip-in.	%Drop	%Return
5	0.20	1816	1414	1720	78	95
6	0.20	2030	1550	1840	76	91
7	0.20	2240	1720	1990	77	89
8	0.20	2450	1840	2100	75	86
5	0.25	1860	1410	1860	76	100
6	0.25	2080	1570	1970	75	95
7	0.25	2310	1760	2140	76	93
8	0.25	2530	1890	2250	75	89
5	0.30	1880	1380	1900	73	101
6	0.30	2110	1550	1950	73	92
7	0.30	2360	1740	2180	74	92
8	0.30	2580	1870	2200	72	85
5	0.35	1860	1330	1960	72	105
6	0.35	2110	1470	1910	70	91
7	0.35	2360	1670	2120	71	90
8	0.35	2600	1790	2150	69	83

Note: A_g = gross cross-sectional area; f'_c = specified 28-day strength of the concrete; M_{drop} = minimum moment that occurs after $M_{peak,1}$ on the moment-curvature curve; $M_{peak,1}$ = first maximum moment that occurs on the moment-curvature curve; $M_{peak,2}$ = second maximum moment that occurs after M_{drop} on the moment-curvature curve; %Drop = ratio of M_{drop} to $M_{peak,1}$; %Return = ratio of $M_{peak,2}$ to $M_{peak,1}$; 1 in. = 25.4 mm; 1 kip-in. = 0.113 kN-m; 1 psi = 6.895 kPa; 1 ksi = 6.895 MPa; W12 = MW77.

Table 9. Results of moment-curvature analysis for 14 in. square pile with six strands (weak axis), square W12 confinement, 0.5 in. diameter strand, and 1200 psi effective prestress

f'_c , ksi	Multiplier $f'_c A_g$	$M_{peak,1}$, kip-in.	M_{drop} , kip-in.	$M_{peak,2}$, kip-in.	%Drop	%Return
5	0.20	1630	1080	1430	66	88
6	0.20	1880	1230	1510	65	80
7	0.20	2120	1420	1650	67	78
8	0.20	2350	1560	1740	66	74
5	0.25	1660	1040	1510	63	91
6	0.25	1920	1210	1570	63	82
7	0.25	2180	1410	1760	65	81
8	0.25	2420	1560	1840	64	76
5	0.30	1650	980	1470	59	89
6	0.30	1920	1130	1510	59	79
7	0.30	2200	1360	1760	62	80
8	0.30	2450	1500	1780	61	73
5	0.35	1620	890	1430	55	88
6	0.35	1890	1030	1460	54	77
7	0.35	2180	1280	1700	59	78
8	0.35	2430	1400	1670	58	69

Note: A_g = gross cross-sectional area; f'_c = specified 28-day strength of the concrete; M_{drop} = minimum moment that occurs after $M_{peak,1}$ on the moment-curvature curve; $M_{peak,1}$ = first maximum moment that occurs on the moment-curvature curve; $M_{peak,2}$ = second maximum moment that occurs after M_{drop} on the moment-curvature curve; %Drop = ratio of M_{drop} to $M_{peak,1}$; %Return = ratio of $M_{peak,2}$ to $M_{peak,1}$; 1 in. = 25.4 mm; 1 kip-in. = 0.113 kN-m; 1 psi = 6.895 kPa; 1 ksi = 6.895 MPa; W12 = MW77.

Table 10. Results of moment-curvature analysis for 14 in. square pile with six strands (weak axis), square W12 confinement, 0.5 in. diameter strand, and 700 psi effective prestress

f'_c , ksi	Multiplier $f'_c A_g$	$M_{peak,1}$ kip-in.	M_{drop} kip-in.	$M_{peak,2}$ kip-in.	%Drop	%Return
5	0.20	1700	1270	1530	75	90
6	0.20	1920	1390	1610	72	84
7	0.20	2140	1560	1810	73	85
8	0.20	2340	1700	1890	73	81
5	0.25	1740	1260	1530	72	88
6	0.25	1990	1410	1580	71	79
7	0.25	2220	1610	1820	73	82
8	0.25	2450	1730	1850	71	76
5	0.30	1760	1240	1500	70	85
6	0.30	2020	1390	1570	69	78
7	0.30	2280	1600	1780	70	78
8	0.30	2520	1720	1810	68	72
5	0.35	1770	1180	1470	67	83
6	0.35	2030	1330	1520	66	75
7	0.35	2290	1540	1740	67	76
8	0.35	2540	1660	1760	65	69

Note: A_g = gross cross-sectional area; f'_c = specified 28-day strength of the concrete; M_{drop} = minimum moment that occurs after $M_{peak,1}$ on the moment-curvature curve; $M_{peak,1}$ = first maximum moment that occurs on the moment-curvature curve; $M_{peak,2}$ = second maximum moment that occurs after M_{drop} on the moment-curvature curve; %Drop = ratio of M_{drop} to $M_{peak,1}$; %Return = ratio of $M_{peak,2}$ to $M_{peak,1}$. 1 in. = 25.4 mm; 1 kip-in. = 0.113 kN-m; 1 psi = 6.895 kPa; 1 ksi = 6.895 MPa; W12 = MW77.

Based solely on the results presented in Tables 5 through 10, it can be argued that for square spiral and strand configurations, $0.35A_g$ is a more appropriate axial load limit when the effective prestress is between 700 and 1200 psi (4830 and 8270 kPa). The only exception was for the singly symmetric six-strand case (weak axis; Table 9) where $0.30f'_c A_g$ is a more appropriate axial load limit when the effective prestress is near 1200 psi.

Results: 14 in. square piles with 3 in. cover

It appears that most 14 in. (350 mm) piles using 3 in. (76.2 mm) of cover are for either state department of transportation related projects (not governed by the axial load limits of the 2018 IBC⁷) or marine projects with low axial loads. All pile configurations presented in Tables 1 through 10 (modified to include 3 in. of cover) result in %Drop greater than 60%. **Figure 11** presents the best results obtained for one of the circular configurations considered. All 14 in. piles with 3 in. of cover (both circular and square strand configurations) should continue to use an axial load limit of $0.20f'_c A_g$, as no improved performance was noted by the research.

Conclusion

The primary goal of this research project was to closely examine the moment-curvature behavior of 14 in. (350 mm) pre-

stressed concrete piles with axial loads greater than $0.2f'_c A_g$. Previous research by Fanous et al.⁹ opined that significant moment drops larger than 40% of the first peak moment could result in unreliable seismic performance and concluded that the most effective way of managing the desired limit on the drop in moment was to limit the axial load to $0.2f'_c A_g$.

Assuming that the 40% drop is actually a concern, the results presented in this paper suggest that more accurate axial load limits can be established.

For circular spiral and strand configurations with 2 in. (76.2 mm) cover, use the following:

- $0.30f'_c A_g$ when the effective prestress is 700 psi (4830 kPa)
- $0.25f'_c A_g$ when the effective prestress is 1200 psi (8270 kPa)

Linear interpolation between $0.30f'_c A_g$ and $0.25f'_c A_g$ may be used for effective prestress values between 700 and 1200 psi (4830 and 8270 kPa), respectively.

Figure 12 shows the impact of adopting the suggested increase in the axial load limit. The moment-curvature behavior and stability remain almost completely unchanged. Although there is a slightly increased moment drop for the

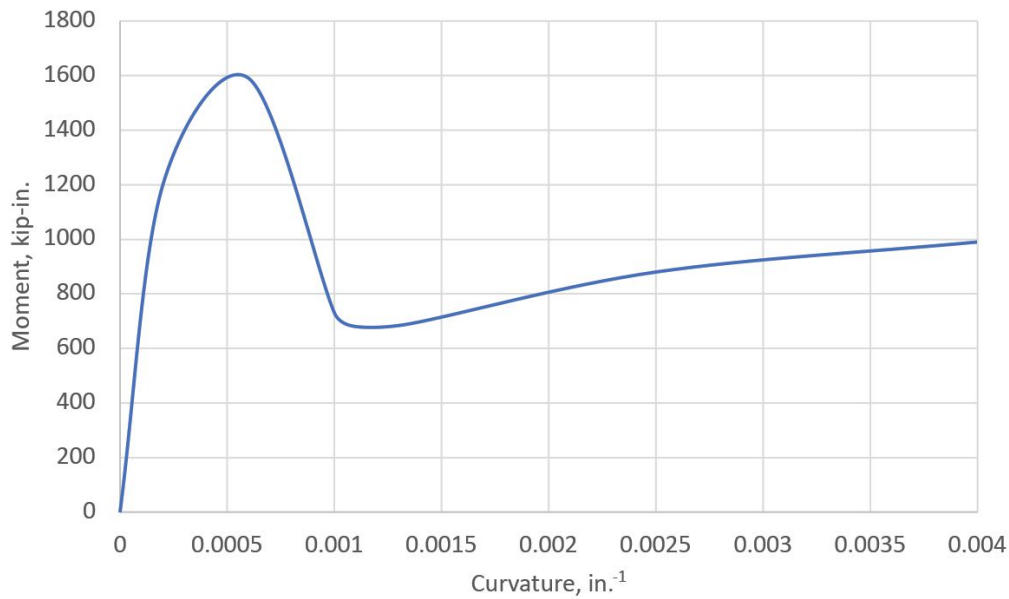


Figure 11. Best shape of full moment-curvature curve with 3 in. of cover. Note that %Drop = 43% and %Return = 63%. This case can be compared with the results of row 1 of Table 2, which are for 2 in. of cover. Note: M_{drop} = minimum moment that occurs after $M_{peak,1}$ on the moment-curvature curve; $M_{peak,1}$ = first maximum moment that occurs on the moment-curvature curve; $M_{peak,2}$ = second maximum moment that occurs after M_{drop} on the moment-curvature curve; %Drop = ratio $M_{drop}/M_{peak,1}$; %Return = ratio $M_{peak,2}/M_{peak,1}$. 1 in. = 25.4 mm; 1 kip-in. = 0.113 kN-m.

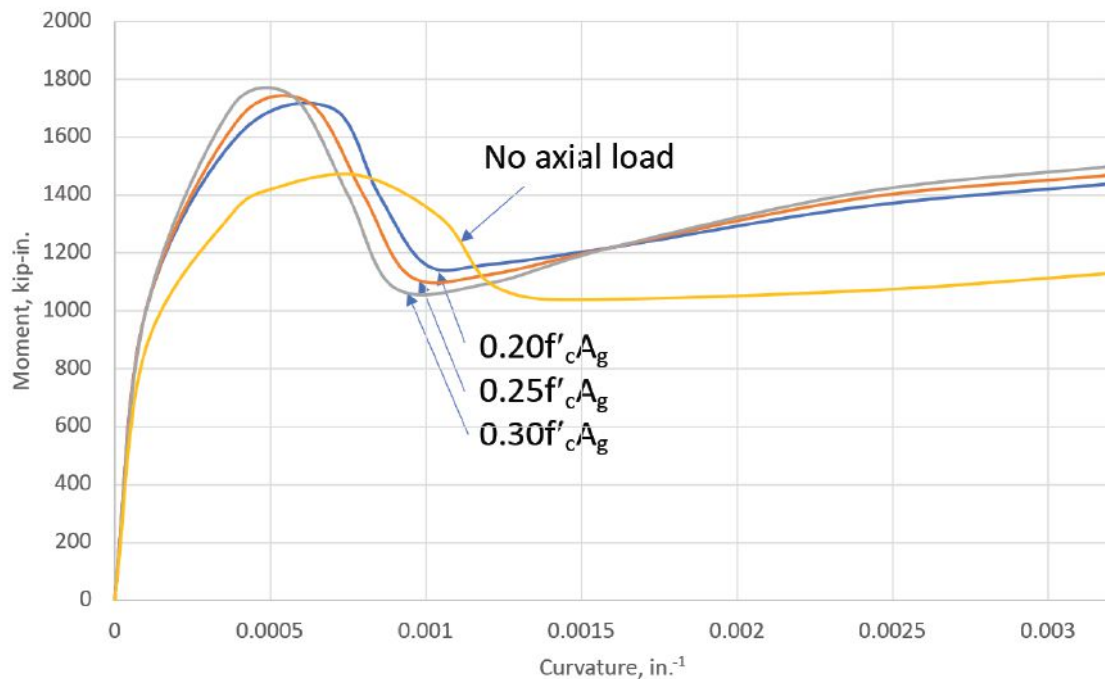


Figure 12. Typical curves showing increased moment drop as axial load is increased. Note: A_g = gross cross-sectional area; f'_c = specified 28-day strength of the concrete. 1 in. = 25.4 mm; 1 k-in. = 0.113 kN-m.

increased axial load, there is also an increase in the second maximum moment that occurs after M_{drop} on the moment-curvature curve $M_{peak,2}$. As such, the energy dissipated appears to be unrelated to the axial loads applied. Although the minimum axial load considered in this study is $0.20 f'_c A_g$, the significant drop in moment occurs even with no axial load applied to the pile. In other words, the moment-curvature response for a pile with zero axial load is only nominally better than the same pile with an axial load ratio equal to 0.35 when coupling seismic performance to a drop in the moment. Therefore, the use of an axial load limit as a means of ensuring acceptable seismic performance may not be reasonably justifiable.

For square confinement and strand configurations with 2 in. (76.2 mm) cover: $0.35 f'_c A_g$ when the effective prestress is between 700 and 1200 psi (4830 and 8270 kPa). Note that square confinement was not considered by Fanous et al.⁹

Based on the results of this research study, the research team recommends that the following options be considered:

- Eliminate the axial load limit for prestressed piles. It is the authors' opinion that the axial load limits for pile ductility applied to piles are unusual and already accounted for directly in vetted codes and standards used in the United States, not appropriate for prestressed piles because the moment strength returns in a reliable manner following the moment drop, and based on a performance requirement not mandated in the codes for other products, such as auger-cast and proprietary pile systems.
- If code committees desire an axial load limit to be maintained, the authors suggest that the axial load limits for 14 in. (350 mm) square piles be increased as justified by the findings of this paper. The authors' discussions with pile producers and designers of 14 in. piles in areas of high seismicity suggest that the increased limits established in this report would be in line with axial loads normally considered in design.
- Where 3 in. (76.2 mm) of cover is required, the authors recommend that the outer 1 in. (25.4 mm) of concrete be considered sacrificial and not included in the cross-sectional analysis calculations used to design the pile. The results of this paper can then be utilized but a significant reduction in moment capacity should be expected (that is, the pile will behave more like a 12 in. [305 mm] pile).
- Although auger-cast piles are outside the scope of this paper, Fig. 2 suggests that they can perform significantly worse than prestressed piles of the same size with respect to moment drop. In addition, the auger-cast pile response considered does not exhibit a second peak moment. This general response exhibited by auger-cast piles may tend toward the exact failure mechanism that limiting the moment drop seeks to address. At a minimum, if

concrete design codes limit prestress pile axial loads due to percent drop in peak moment to prevent instability, other concrete foundation elements should conform to the same limitations.

Previous experimental research on the seismic design of prestressed piles has focused primarily on the ductility of pile hinges under cyclic loading. The condition of the exposed pile hinge after a major earthquake would also be important in regard to pile repair and potential future use without repair or replacement. Although analytical models used in this study and previous experimental research suggest that piles maintain their prestress after multiple reversed cyclic loads, the fact that many pile hinges would occur in areas that are not repairable makes this an important area of future research.

Acknowledgments

The authors wish to thank PCI for its support. The research discussed in this paper would not be possible without the financial support from PCI and the input from PCI committee members.

References

1. ICBO (International Conference of Building Officials). 1997. *Uniform Building Code*. Whittier, CA: ICBO.
2. ICC (International Code Council). 2015. *International Building Code*. Country Club Hills, IL: ICC.
3. Banerjee, S., J. F. Stanton, and N. M. Hawkins. 1987. "Seismic Performance of Precast Concrete Bridge Piles." *Journal of Structural Engineering* 113 (2): 381–396.
4. Budek, A. M., G. Benzoni, and M. J. N. Priestly. 1997. *Experimental Investigation of Ductility of In-Ground Hinges in Solid and Hollow Prestressed Piles*. Report SSRP-97/17, University of California San Diego.
5. Sritharan, S., A. Cox, J. Huang, M. Suleiman, and K. Arulmoli. 2016. "Minimum Confinement Reinforcement for Prestressed Concrete Piles and a Rational Seismic Design Framework." *PCI Journal* 61 (1): 51–69.
6. PCI Committee on Prestressed Concrete Piling. 2019. "Recommended Practice for Design, Manufacture, and Installation of Prestressed Concrete Piling." *PCI Journal* 64 (4): 84–116.
7. ICC. 2018. *International Building Code*. Country Club Hills, IL: ICC.
8. ACI (American Concrete Institute) Committee 318. 2019. *Building Code Requirements for Structural Concrete (ACI 318-19) and Commentary (ACI 318-19R)*. Farmington Hills, MI: ACI.

9. Fanous, A., S. Sritharan, M. Suleiman, J. Huang, and K. Arulmoli. 2010. "Minimum Spiral Reinforcement Requirements and Lateral Displacement Limits for Prestressed Concrete Piles in High Seismic Regions." Final report to PCI. ISU-ERI-Ames report ERIERI-10321, Department of Civil, Construction, and Environmental Engineering, Iowa State University, Ames, IA.
10. Michael N. Fardis, Eduardo C. Carvalho, Peter Fajfar, and Alain Pecker. 2015. *Seismic Design of Concrete Buildings to Eurocode 8*. Boca Raton, FL: CRC Press.
11. ASCE/SEI Committee 41. 2017. *Seismic Evaluation and Retrofit of Existing Buildings*. ASCE/SEI 41-17. Reston, VA: American Society of Civil Engineers.
12. California State Lands Commission. 2016. "Marine Oil Terminals." In Title 24, *California Code of Regulations*, Part 2, California Building Code. Long Beach, CA: California State Lands Commission.
13. ASCE/COPRI Committee 61. 2014. *Seismic Design of Piers and Wharfs*. ASCE/COPRI 61-14. Reston, VA: American Society of Civil Engineers.
14. Port of Long Beach. 2015. *Port of Long Beach Wharf Design Criteria*. Long Beach, CA: Port of Long Beach.
15. South Carolina Department of Transportation. 2008. *SCDOT Seismic Design Criteria*. Columbia, SC: South Carolina Department of Transportation.
16. ASTM A416. 2018. *Standard Specification for Low-Relaxation, Seven-Wire Steel Strand for Prestressed Concrete*. ASTM A416/A416M-18: West Conshohocken, PA: ASTM International.
17. ASTM Subcommittee A01.05. 2010. *Standard Specification for Steel Wire and Welded Wire Reinforcement, Plain and Deformed, for Concrete*. ASTM A1064/ A1064M-10. West Conshohocken, PA: ASTM International.
18. Mander, J. B., M. J. N. Priestley, and R. Park. 1988. "Theoretical Stress-Strain Behavior of Confined Concrete." *Journal of the Structural Division* 114 (8): 1804–1825.
19. Ryan, J. C., and T. W. Mays. 2020. *Axial Load Limit Considerations for 14 in. Prestressed Concrete Piles Reconciling the 2018 IBC and ACI 318-19 Prestressed Pile Axial Load Limits with PCI's 2019 Recommended Practice for Design, Manufacture, and Installation of Prestressed Concrete Piling*. Report no. CIT-CEE-1, The Citadel, Charleston, SC.

Notation

A_g = gross cross-sectional area

A_{sh} = total cross-sectional area of transverse reinforcement provided separately in each direction, including crossties where applicable

A_{sp} = cross-sectional area of spiral reinforcement

f_c = stress in concrete

f'_c = specified 28-day strength of the concrete

f'_{cc} = ultimate stress in confined concrete

f'_{co} = stress in unconfined concrete

f_{pc} = effective prestress in the pile

f_{pu} = ultimate strength of prestressing strand

f_{yh} = yield strength of spiral reinforcement

h_c = confined concrete side dimension defined by transverse steel dimension

M_{drop} = minimum moment that occurs after $M_{peak,1}$ on the moment-curvature curve

M_{max} = maximum moment

M_p = plastic or maximum moment on the bilinear idealized moment-curvature curve

$M_{peak,1}$ = first maximum moment that occurs on the moment-curvature curve

$M_{peak,2}$ = second maximum moment that occurs after M_{drop} on the moment-curvature curve

M_{sh} = moment at strain hardening

M_u = ultimate moment

P = axial load on the pile

$\%Drop$ = ratio of M_{drop} to $M_{peak,1}$

$\%Return$ = ratio of $M_{peak,2}$ to $M_{peak,1}$

s = longitudinal spacing of the transverse steel

Δ = pile deflection

ϵ_c = strain in concrete

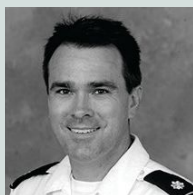
ϵ_{cc} = strain in confined concrete at peak stress

ϵ_{co} = strain in unconfined concrete at peak stress

ϵ_{cu} = ultimate strain in concrete

ε_{spall}	= strain at unconfined concrete spalling
θ_u	= ultimate rotation of the plastic hinge
ρ_s	= quantity of confinement spiral
ϕ_{cr}	= curvature at the initiation of tension cracking
ϕ_m	= maximum curvature
ϕ_{max}	= maximum curvature
ϕ_p	= plastic curvature
ϕ_{sh}	= curvature at strain hardening
ϕ_{sp}	= curvature associated with the initiation of unconfined concrete spalling
ϕ_u	= ultimate curvature

About the authors



Timothy W. Mays, PhD, PE, is a professor of civil engineering at The Citadel in Charleston, S.C. He actively participates in PCI-related research and on standards development committees through PCI and the American Society of Civil Engineers. He obtained his

doctorate in civil engineering from Virginia Polytechnic Institute and State University in Blacksburg, Va., in 2000. His areas of expertise are code applications, structural design, foundations, seismic design, steel connections, structural dynamics, coastal design, and civil engineering aspects of antiterrorism.



John C. Ryan, PhD, PE, is an assistant professor of civil engineering at The Citadel in Charleston, S.C. He provides structural foundation engineering services through Ryan Structural Engineers LLC. He is actively involved with prestress pile

research through PCI. He obtained his doctorate in civil engineering from Virginia Polytechnic Institute and State University in Blacksburg, Va., in 2006.

Abstract

The 2018 *International Building Code* and *American Concrete Institute Building Code Requirements for Structural Concrete (ACI 318-19) and Commentary (ACI 318R-19)* have adopted axial load limits that prohibit the use of some 14 in. (350 mm) square prestressed concrete piles in areas of moderate to high seismicity. This paper presents the results of a study that examined the development of these axial load limits, their appropriateness as an attempt to ensure reliable seismic performance, and the expected seismic performance of commonly used 14 in. (350 mm) square prestressed concrete piles when the axial load limit is increased to levels commonly used in seismic design practice. Results of the study suggest that the axial load limits established by previous researchers are overly conservative and do not ensure reliable seismic performance. This paper recommends that reduced nominal moment strength be used in lieu of axial load limits for consistency with codified approaches already used in the United States and to help ensure reliable seismic performance when appropriate.

<https://doi.org/10.15554/pcij66.6-02>


Keywords

Axial load limit, confinement, design, foundation, pile, seismic.

Review policy

This paper was reviewed in accordance with the Precast/Prestressed Concrete Institute's peer-review process.

Reader comments

Please address any reader comments to *PCI Journal* editor-in-chief Tom Klemens at tklemens@pci.org or Precast/Prestressed Concrete Institute, c/o PCI Journal, 8770 W. Bryn Mawr Ave., Suite 1150, Chicago, IL 60631. 

Live-load distribution of an adjacent box-beam bridge: Influence of bridge deck

Ryan T. Whelchel, Christopher S. Williams, and Robert J. Frosch

- Leaking longitudinal joints are commonly observed in adjacent box-beam bridges and may lead load-rating engineers to assume that there is no load distribution where signs of shear key deterioration are observed.
- This paper discusses a series of load tests that were performed on an existing adjacent box-beam structure with leaking joints to determine the load distribution for a deteriorated adjacent concrete box-beam bridge.
- The study found that deteriorated shear keys are capable of distributing load in an adjacent concrete box-beam bridge, the addition of a concrete deck can restore or improve load distribution for a deteriorated structure where the shear keys have failed, and the load distribution for the rehabilitated structure corresponds well with current design equations.

Leaking longitudinal joints are commonly observed in adjacent box-beam bridges and are often associated with an assumed loss of load distribution at the leaking joint. Evidence of a leaking joint (**Fig. 1**) or the presence of a reflective crack in the deck calls into question the condition of the shear key and the capacity of the shear key to transfer load between beams. The position of shear keys within an adjacent box-beam bridge makes visual inspection impossible, and there is no standard nondestructive inspection method to evaluate the condition of the shear key. In the absence of a dependable inspection, load-rating engineers may assume that there is no load distribution where signs of shear key deterioration are observed.

Investigators have conducted load tests to determine the load distribution of adjacent box-beam bridges exhibiting signs of shear key deterioration.^{1,2} Steinburg and colleagues¹ performed load tests on the center span of a three-span adjacent box-beam bridge constructed in 1967 with spans of 47.83 ft (14.58 m), transverse ties at the third points of each span, and a bituminous wearing surface. Center span deterioration consisted of delaminated concrete in the top flange of the exterior beams and minimal efflorescence at the longitudinal joints. Results of the load tests indicated that the distribution factors based on measured strains and deflections were consistent with the distribution factors estimated using equations from the fifth edition of the American Association of State Highway and Transportation Officials' *AASHTO LRFD Bridge Design Specifications*.³

PCI Journal (ISSN 0887-9672) V. 66, No. 6, November–December 2021.

PCI Journal is published bimonthly by the Precast/Prestressed Concrete Institute, 8770 W. Bryn Mawr Ave., Suite 1150, Chicago, IL 60631.

Copyright © 2021, Precast/Prestressed Concrete Institute. The Precast/Prestressed Concrete Institute is not responsible for statements made by authors of papers in *PCI Journal*. Original manuscripts and discussion on published papers are accepted on review in accordance with the Precast/Prestressed Concrete Institute's peer-review process. No payment is offered.



Figure 1. Leaking joint of an adjacent box-beam bridge.

Kassner and Balakumaran² conducted a series of load tests on one span of an existing adjacent box-beam bridge constructed in 1959 with five spans (consisting of a combination of 40.75 and 41.5 ft [12.42 and 12.65 m] individual spans), a single transverse tie tensioned to 30 kip (133 kN), and a bituminous wearing surface. The bridge deterioration consisted of isolated concrete spalling on two beams due to poor concrete consolidation, as well as efflorescence at longitudinal joints that indicated leaking shear keys. Consistent with the study by Steinburg et al., the results of the load tests revealed that the distribution factors based on measured strains were consistent with the distribution factors estimated using equations from the sixth edition of the AASHTO LRFD specifications,⁴ which were unchanged from the fifth edition. These same equations continue to be specified in the 2020 AASHTO LRFD specifications.⁵

Steinburg et al., Kassner and Balakumaran, and Attanayake and Aktan⁶ found that a leaking shear key may not indicate loss of load distribution. It should be noted that these studies were conducted on bridges constructed with bituminous wearing surfaces. Load test data are not available for bridges constructed with composite or noncomposite concrete decks that have evidence of leaking shear keys.

For adjacent box-beam bridges with reinforced concrete decks, the deck provides an additional mechanism for load distribution. However, current bridge design specifications do not consider the load distribution offered by this mechanism

acting without effective shear keys. Table 4.6.2.2.1-1 of the 2020 AASHTO LRFD specifications provides equations for two load distribution cases for adjacent box-beam bridge systems: cases (f) and (g). Case (f) considers adjacent beams with shear keys and a concrete deck. Case (g) considers adjacent beams with shear keys and transverse post-tensioning to provide compression at the longitudinal joint. When evaluating a Case (f) bridge with shear keys exhibiting signs of deterioration where the integrity of the shear key is in question, the amount of load distribution offered by the concrete deck alone is needed but not specified in the 2020 AASHTO LRFD specifications. Similarly, the *AASHTO Manual for Bridge Evaluation*⁷ provides no guidance on the live-load distribution of an adjacent box-beam bridge with a concrete deck and no (or deteriorated) shear keys. Furthermore, there is extremely limited experimental research available regarding the load distribution offered by a concrete deck over adjacent beams without shear keys. The only known research is by Jones,⁸ who conducted static load tests on an adjacent box-beam bridge constructed with a 4 in. (100 mm) thick composite concrete deck without shear keys or transverse post-tensioning. Although that study does not present the load distribution for the bridge, the load distribution can be estimated from strains that were measured on the underside of each beam.

Research scope and significance

Considering the general lack of test data and uncertainty in analyzing deteriorated concrete structures, a series of load

tests were conducted to determine the load distribution of a deteriorated adjacent concrete box-beam bridge. Both the load distribution of the existing structure with leaking joints and load distribution after rehabilitation with a noncomposite reinforced concrete deck were investigated. A noncomposite deck (no shear connectors) was selected to provide a cost- and time-effective solution for the rehabilitation of the existing bridge and also to simplify future deck replacements.

The load tests were conducted on a 40 ft (12.2 m) long adjacent precast, prestressed concrete box-beam bridge in Tippecanoe County, Ind. The bridge was tested in four conditions: as built, after removal of the bituminous wearing surface, after the shear keys were disabled, and with a reinforced concrete deck installed. In addition to assessing load distribution of the existing bridge, the results of this study can serve as support for the use of a concrete deck as a rehabilitation strategy to restore load distribution or function as the primary load distribution mechanism of an adjacent box-beam bridge.

Existing bridge

The adjacent box-beam bridge used for this study was constructed in 1957 and designed based on the 1957 edition of the American Association of State Highway Officials' *AASHTO Standard Specifications for Highway Bridges*.⁹ The single-span bridge consists of seven adjacent precast, prestressed concrete box beams that are 45 in. (1143 mm) wide and 21 in. (533 mm) deep. The total length of the bridge is 40 ft (12.2 m), and the beams span approximately 39 ft (11.9 m) from centerline of bearing to centerline of bearing. Section properties were assumed to be similar to the 1961 Indiana Department of Transportation (INDOT) standard box beam, section B-21-3-9 (Fig. 2). Only a portion of the original design drawings is available, and there are no standard drawings from before 1961.

The original drawings specified $\frac{3}{8}$ in. (9.5 mm) diameter seven-wire stress-relieved strand with a minimum tensile strength of 250 ksi (1724 MPa). In 1993, the north exterior box beam (beam 7) was replaced with a precast, prestressed concrete box beam of the same overall dimensions (Fig. 3). Drawings are also unavailable for this replacement beam.

The number of strands in each beam was determined using ground-penetrating radar (GPR). The 1957 beams were found to have 21 strands, and the 1993 beam had 12 strands. The difference in the number of strands led investigators to conclude that the 1993 replacement beam is reinforced with $\frac{1}{2}$ in. (12.7 mm) diameter strand. The bridge included a bituminous wearing surface, which was estimated to be 5 in. (127 mm) thick based on a GPR survey. The bridge did not include transverse tie rods, and no transverse post-tensioning was provided.

The condition of the existing bridge was investigated prior to testing and is documented in Fig. 3. Investigators found evidence of water leaking through the shear keys between every beam, with the exception of the joint between beams 4 and 5 (Fig. 3). The investigation also revealed deterioration on beams 1 and 7. Minor longitudinal cracking and concrete spalling were observed on the west end of beam 7 (Fig. 4), and the investigators assumed that these conditions had a negligible effect on the flexural strength of the beam. Beam 1 had two rust-stained longitudinal cracks approximately 5 ft (1.5 m) long, located at midspan (Fig. 4) and three exposed strands at the east support (Fig. 4).

Testing procedure

The bridge was load tested in four stages, as described in the following sections, to capture the live-load distribution con-

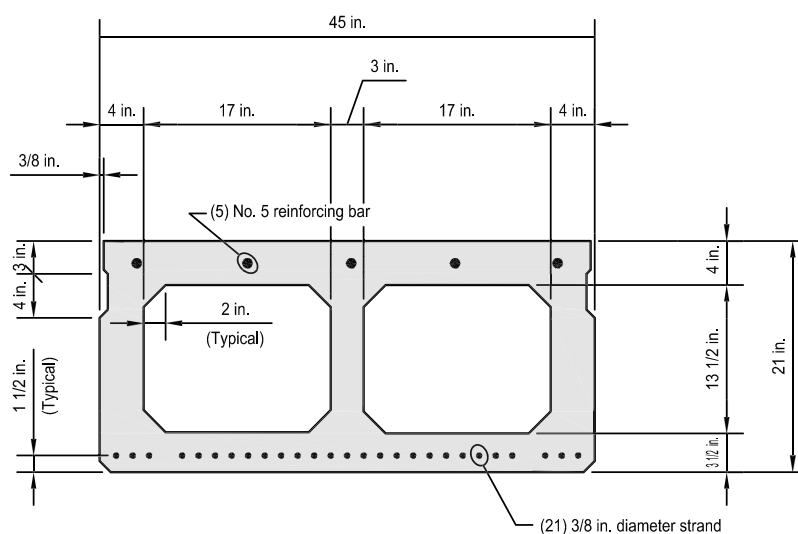


Figure 2. Box-beam cross-section geometry. Note: no. 5 = 16M; 1 in. = 25.4 mm.

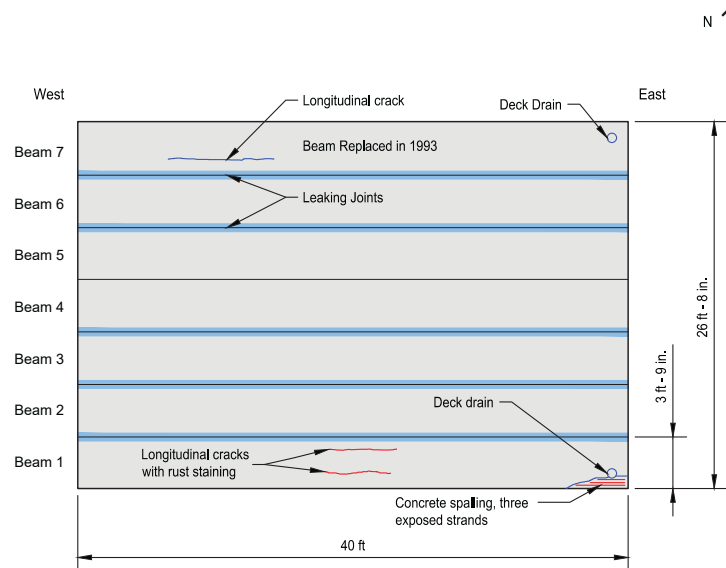
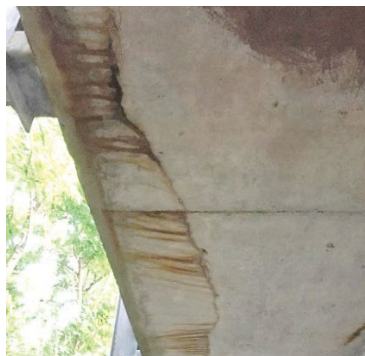


Figure 3. Bottom flange deterioration map of existing bridge. Note: 1 in. = 25.4 mm; 1 ft = 0.305 m.



Longitudinal cracking and minor concrete spalling in west end of beam 7



Rust-stained longitudinal crack on south side of beam 1



Rust-stained longitudinal crack on north side of beam 1



Three exposed strands at east support of beam 1

Figure 4. Bridge deterioration.

sidering four different superstructure conditions. **Figure 5** provides a visual summary of the conditions.

Load test 1: As built

The first load test (LT1) was performed on the bridge as built without any modifications. Beam 1 was not directly loaded because there were concerns regarding the deterioration of the member (Fig. 3).

Load test 2: Wearing surface removed

After LT1 was completed, the bridge was closed to traffic to allow bridge modifications to be completed safely. A bridge contractor removed the bituminous wearing surface. During the milling operation, the milling machine removed a portion of the top flange of each beam and exposed regions of deterioration in beams 1 and 3 that had led to the formation of holes through the flanges (**Fig. 6**). The hole in beam 1 was

approximately 10 × 10 in. (254 × 254 mm), and the concrete around the hole had been reduced to rubble over the life of the structure. Both holes in beam 3 were approximately 30 in. (762 mm) long and 10 in. wide after the removal of deteriorated concrete. The holes in each beam were prepared for repair by removing any deteriorated concrete and cleaning the surface around each hole. The contractor then repaired the top flanges by positioning formwork along the bottom of the flange and filling the holes with prepackaged concrete. After the repairs to the top flange of beams 1 and 3 were completed, a second load test (LT2) was performed. As a consequence of the damage to the top flanges, beams 1, 2, and 3 were not directly loaded during the second and third load tests.

Load test 3: Shear keys disabled

A pavement saw, cutting to a depth of 12 in. (305 mm), was used to cut through the entire depth of the shear keys (**Fig. 7**). The third load test (LT3) was performed to verify that the

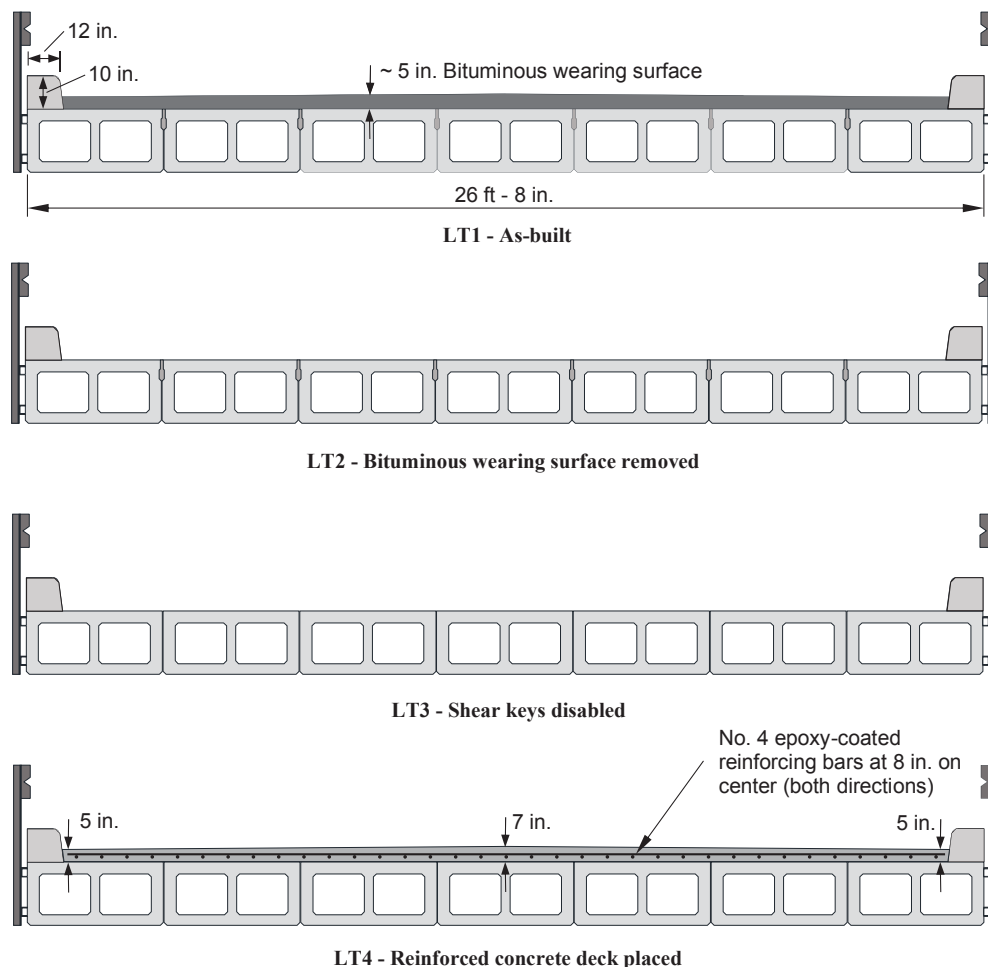


Figure 5. Load test bridge conditions. Note: LT1 = load test 1; LT2 = load test 2; LT3 = load test 3; LT4 = load test 4. No. 4 = 13M; 1 in. = 25.4 mm; 1 ft = 0.305 m.

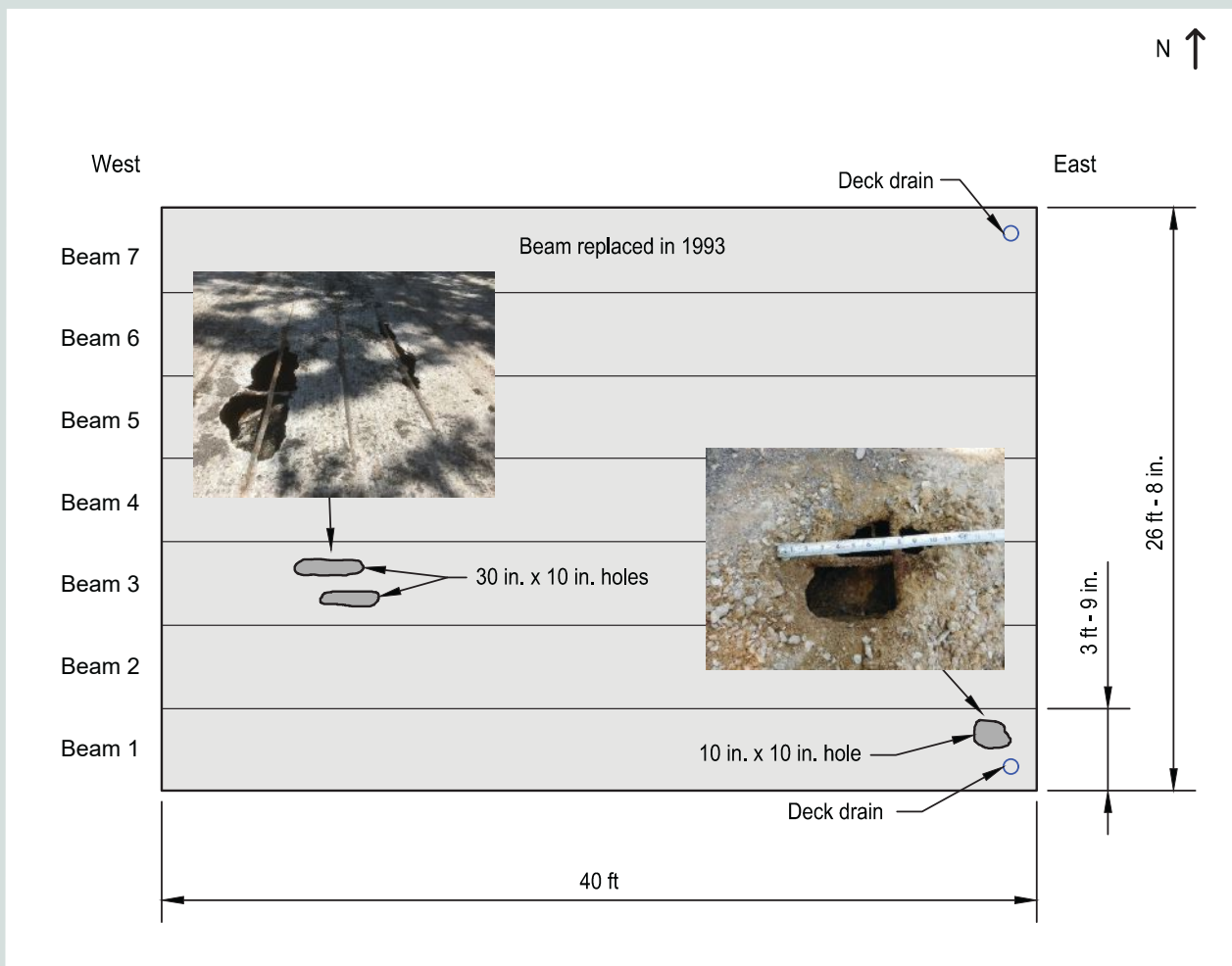


Figure 6. Plan view of the bridge top flange deterioration. Note: 1 in. = 25.4 mm; 1 ft = 0.305 m.



Figure 7. Shear key-cutting operation.

shear keys were disabled and that each beam was acting independently. Disabling the shear keys provides a worst-case scenario for load distribution and allows the contribution of a deck retrofit to load distribution to be fully assessed.

Load test 4: Concrete deck placed

The fourth and final load test (LT4) was performed after a new reinforced concrete deck was placed on the box beams.

Bridge deck

A noncomposite concrete deck was added to the bridge to evaluate its effectiveness in restoring load distribution to a bridge with nonfunctioning shear keys.

Design

The concrete deck was designed using the *Indiana Design Manual*¹⁰ (IDM) and the eighth edition of the 2017 AASHTO LRFD specifications.¹¹ The deck reinforcement was selected to satisfy the temperature and shrinkage reinforcement requirements of the 2017 AASHTO LRFD specifications. The required area of reinforcement was calculated to be 0.11 in.²/ft (233 mm²/m). The IDM also specifies an 8 in. (203 mm) maximum spacing for bridge deck reinforcement. This light reinforcement requirement could have been satisfied using no. 3 (10M) reinforcing bars or even welded-wired reinforcement. However, the use of small-diameter reinforcing bars or welded-wire reinforcement in bridge decks is not recommended because workers walking on the reinforcement

can easily bend the flexible bars or wires. Bent or displaced reinforcement can lead to difficulties maintaining minimum cover requirements and controlling the effective depth of the reinforcement. Therefore, no. 4 (13M) reinforcing bars at 8 in. maximum spacing were selected (0.3 in.²/ft [635 mm²/m] area of reinforcement provided) to prevent constructibility issues. To conform with IDM bridge deck reinforcement requirements, Grade 60 (414 MPa) epoxy-coated reinforcing bars were specified.

The IDM specifies that concrete decks must have a minimum top cover thickness of 2.5 in. (63.5 mm) plus 0.5 in. (12.7 mm) for a sacrificial wearing surface. On this project, a minimum bottom cover of 1 in. (25.4 mm) was used to provide for concrete flow under the reinforcement. Using a single mat of no. 4 (13M) reinforcing bars in both directions (1 in. thick), along with the cover requirements, resulted in a total minimum deck thickness of 5 in. (127 mm).

Construction

The surface of each box beam was prepared by sandblasting (**Fig. 8**) to ensure that an adequate bond between the beams and the deck was achieved. The deck was placed in four sections from south to north (**Fig. 6**), each requiring one concrete truck. The deck thickness was tapered from the bridge centerline to the curb for water drainage. The thickness of the deck was 7 in. (178 mm) at the bridge centerline and 5 in. (127 mm) at each curb line of the transverse section (1.3% cross slope) (**Fig. 5**). The cross slope was achieved by using tapered formwork at the bridge ends and



Figure 8. Sandblasted box-beam surface.

using a mechanical screed to finish the bridge along the span and across the width (**Fig. 9**). For the final surface finish, the deck was tined after the concrete set. After the surface finish was applied, the deck was covered with wet burlap and plastic for a three-day wet cure.

Materials

The deck concrete mixture proportions (**Table 1**) referenced ASTM standards^{12–14} and followed Class C specifications from INDOT’s *2018 Standard Specifications*.¹⁵ Concrete cylinders (6 × 12 in. [152 × 305 mm]) were prepared for compression testing from each of the four trucks used for the deck placement. According to Tippecanoe County’s construction guidelines, the deck must reach a minimum compressive strength of

4000 psi (27.6 MPa) before a bridge is opened to traffic. All cylinders were cast and stored at the bridge site in accordance with ASTM C31 *Standard Practice for Making and Curing Concrete Test Specimens in the Field*¹⁶ until the cylinders were transported from the site for testing. The graph in **Fig. 10** plots the average concrete compressive strength of the cylinders over time. For each data point, eight cylinders (two from each truck) were tested in accordance with ASTM C39 *Standard Test Method for Compressive Strength of Cylindrical Concrete Specimens*.¹⁷ Figure 10 shows that the concrete met the minimum requirements to be opened to traffic within three days.

Grade 60 (414 MPa) no. 4 (13M) reinforcing bars conforming to ASTM A615 *Standard Specification for Deformed and Plain Carbon-Steel Bars for Concrete Reinforcement*¹⁸ were



Figure 9. Use of mechanical screed and tapered formwork to construct bridge cross slope.

Table 1. Concrete mixture proportions

Material	Type	Quantity
Cement	ASTM C150 Type I	658 lb/ft ³
Coarse aggregate	No. 8 limestone (1 in. maximum aggregate size)*	1725 lb/ft ³
Fine aggregate	No. 23 natural sand*	1225 lb/ft ³
Air entrainment	ASTM C260	3.3 oz/yd ³
Water-reducing admixture and retarder	ASTM C494 Type D	19.7 oz/yd ³
Water	n/a	249 lb/yd ³
Water-cement ratio	n/a	0.38
Specified slump	n/a	4 in.

Note: n/a = not applicable. 1 in. = 25.4 mm; 1 oz/yd³ = 38.681 mL/m³; 1 lb/ft³ = 16.031 kg/m³; 1 lb/yd³ = 0.593 kg/m³.

* Refer to Indiana Department of Transportation (INDOT) standard specifications (INDOT, 2018) for gradation.

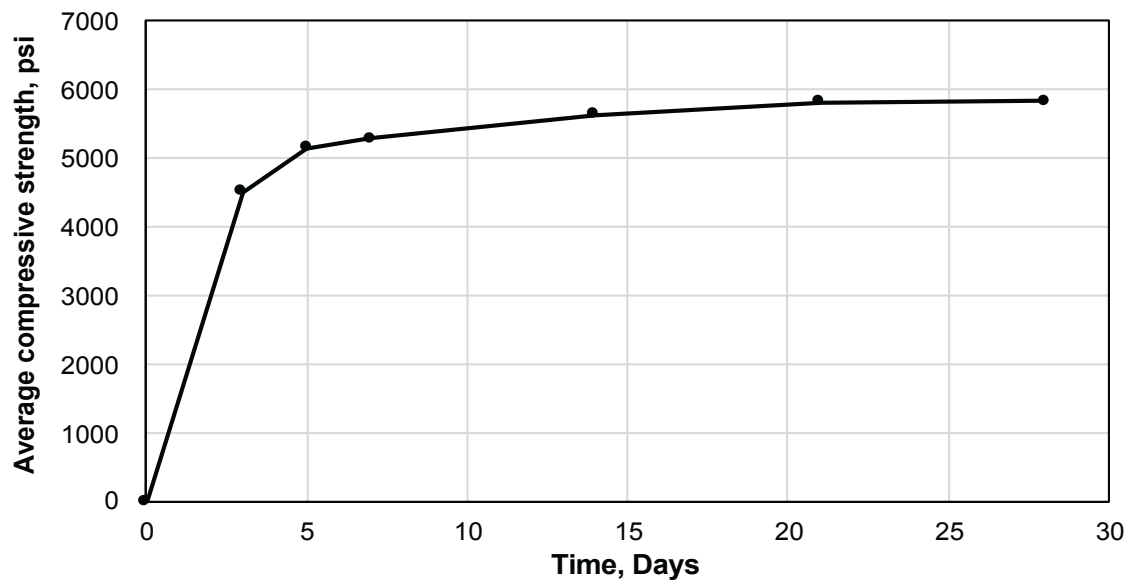


Figure 10. Concrete cylinder compressive strength over time. Note: 1 psi = 6.895 kPa.

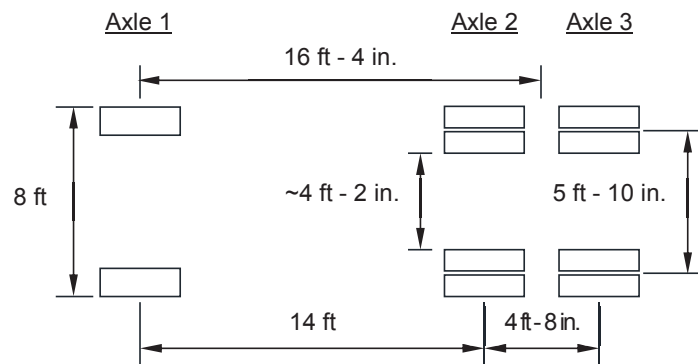


Figure 11. Truck used for load tests and diagram of truck wheel locations. Note: 1 in. = 25.4 mm; 1 ft = 0.305 m.

used for all reinforcement. The measured yield and ultimate tensile strengths of the reinforcing bars were 88 and 104 ksi (607 and 717 MPa), respectively.

Loading procedure

Each of the four load tests was conducted with the same tri-axle truck loaded with gravel. The weight of the vehicle was measured using portable truck-weigh scales from the Indiana State Police Division of Commercial Vehicles. **Figure 11** includes the wheelbase dimensions and axle labels for the truck, and **Table 2** provides the axle weights for each load

Table 2. Truck weights

Load test	Axle 1, lb	Axle 2, lb	Axle 3, lb	Total, lb
LT1	16,450	21,100	20,050	57,600
LT2	15,650	22,300	21,350	59,300
LT3	14,800	15,450	14,450	44,700
LT4	16,450	21,000	21,300	58,750

Note: 1 lb = 4.45 N.

test. A reduced load was used for LT3 because the shear keys were disabled.

A total of 50 load positions—five longitudinal locations along 10 transverse paths—were defined for the bridge. The five positions along the span were selected to approximate the progression of a vehicle crossing the bridge (**Fig. 12**). The 10 transverse paths traveled by the truck were split into five eastbound paths (paths 1 through 5) and five westbound paths (paths 6 through 10). **Figure 13** illustrates the transverse positions of the truck for the 10 paths. The deterioration observed in the site survey and after removal of the bituminous wearing surface prevented some paths from being used for LT1, LT2, and LT3.

Instrumentation

The bridge was instrumented with three linear string potentiometers per beam (21 potentiometers total) to monitor the deflection at the quarter points of each beam. **Figure 14** shows a plan view of the bridge indicating the sensor locations. The potentiometers were mounted on a frame erected on top of scaffolding positioned under the bridge to record absolute deflections. In addition to the potentiometers, concrete strain

gauges (90 mm gauge length) were installed on the bottom flange of each beam at midspan as a redundant measurement in the event a potentiometer failed.

Load test results

Figure 15 summarizes the load test results corresponding to position 4 (see **Fig. 12** for position location), which is the position where the maximum midspan deflections were recorded. The illustration at the top of **Fig. 15** shows the longitudinal position of the truck (position 4) and the direction of travel corresponding to the plots that are provided below the illustration (eastbound for paths 1 through 5 and westbound for paths 6 through 10). A representation of the bridge cross section is illustrated above each deflection plot, and a set of truck tires is shown on top of each cross section to indicate the transverse position of the truck. Midspan deflections of each beam are shown for the truck positioned along all paths. As discussed previously, damage to some beams prevented the loading of some paths. Therefore, paths 4, 5, 9, and 10 were the only paths loaded for all four load tests. A comparison of the results from the eastbound and westbound paths shows the results for both traveling directions were similar.

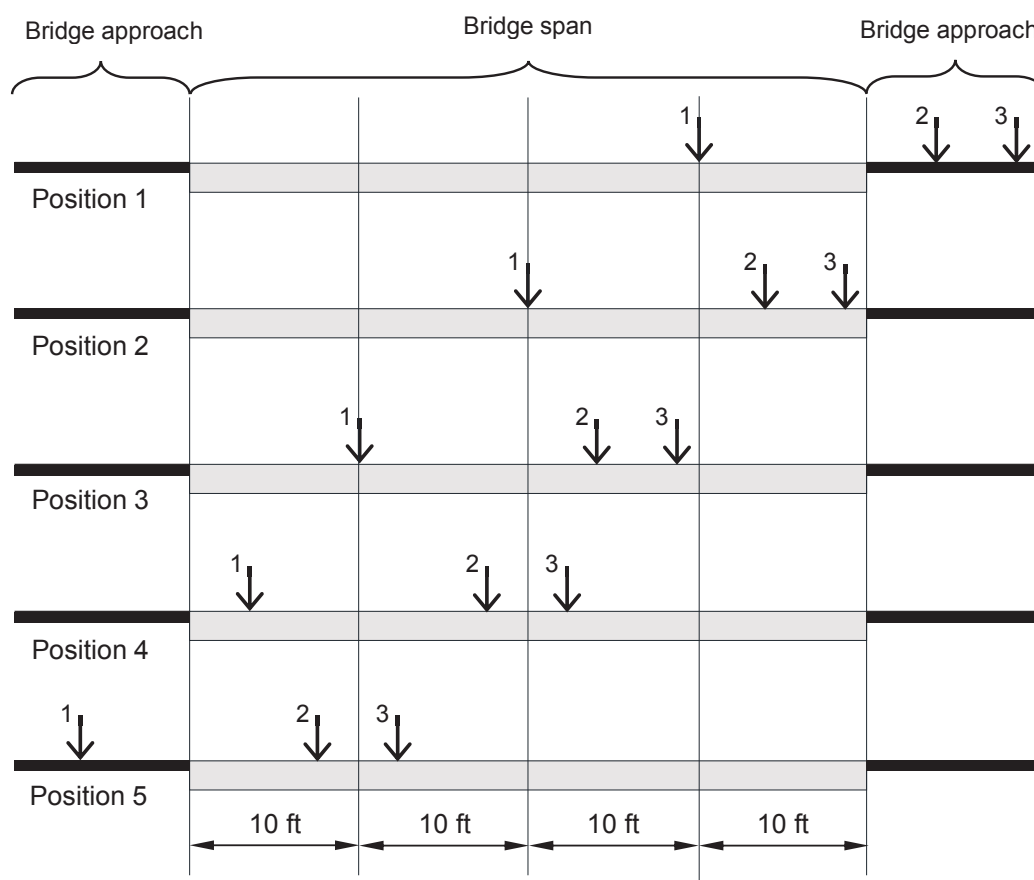


Figure 12. Longitudinal truck positions. Note: Numerical values next to arrows refer to axle labels in **Fig. 11**. 1 ft = 0.305 m.

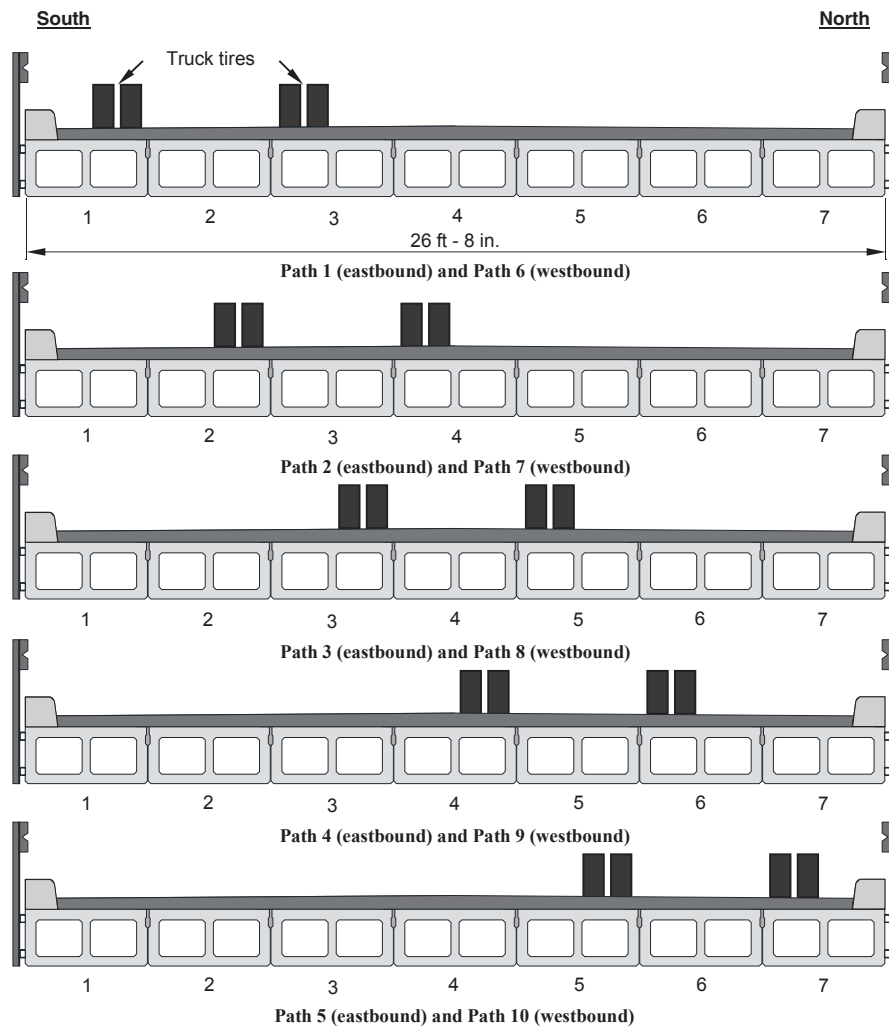


Figure 13. Transverse truck positions during load testing. Note: 1 in. = 25.4 mm; 1 ft = 0.305 m.

LT1: As-built condition

For the first load test, the deflected shape of the transverse section for each path in Fig. 15 shows that a nonzero value of deflection was recorded for every beam. This indicates that every beam was engaged to carry the truck load for each path. Although the longitudinal joints exhibited signs of water leaking through the shear keys, load was distributed to all seven beams for each transverse position. This finding demonstrates that a leaking shear key does not indicate that load transfer has been eliminated or that the shear key is ineffective.

LT2: Wearing surface removed

A comparison of the curves for LT1 and LT2 in Fig. 15 shows that larger deflections were generally measured during LT2 for the beams that were directly loaded. In addition, discontinuities in the transverse deflected shape appear for the beams that were directly loaded.

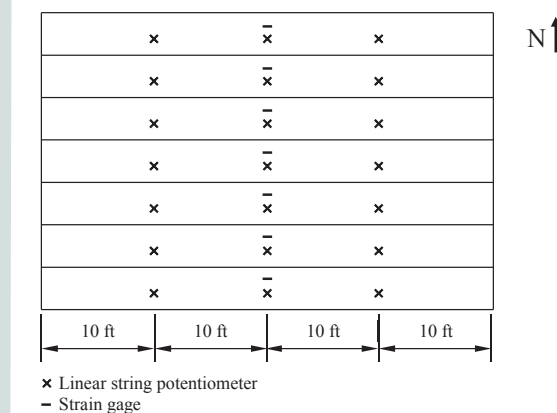


Figure 14. Instrumentation plan. Note: 1 ft = 0.305 m.

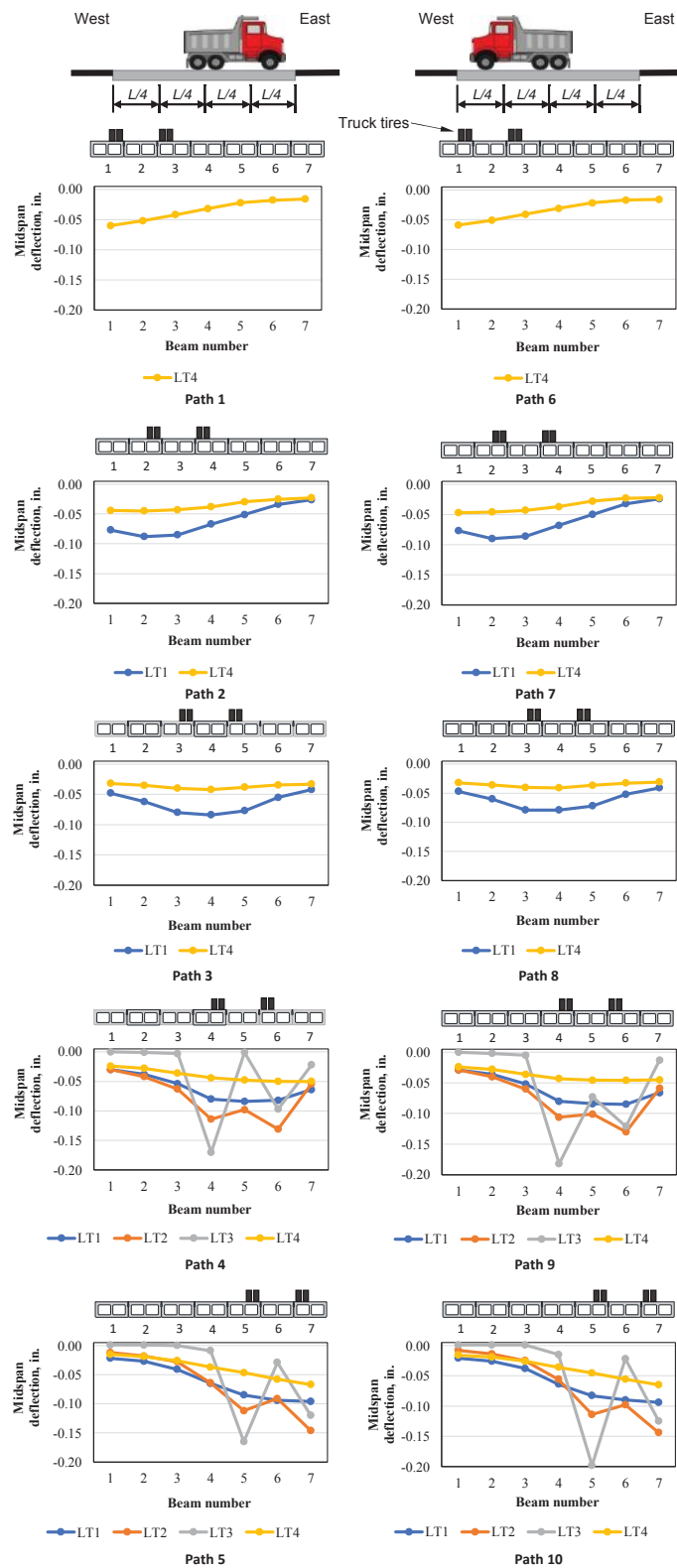


Figure 15. Summary of load test results for truck position 4. Note: The illustration at the top of the figure shows the longitudinal position of the truck (position 4) and the direction of travel corresponding to the plots that are provided below the illustration (eastbound for paths 1 through 5 and westbound for paths 6 through 10). A representation of the bridge cross section is illustrated above each deflection plot, and a set of truck tires is shown on top of each cross section to indicate the transverse position of the truck for the indicated path. L = span length; LT1 = load test 1; LT2 = load test 2; LT3 = load test 3; LT4 = load test 4. 1 in. = 25.4 mm.

The increase in measured deflections and the discontinuities in the deflected shape were caused by three factors. First, the milling operation that was conducted between LT1 and LT2 removed a small portion (approximately 0.5 to 2 in. [12.7 to 50.8 mm]) of each beam top flange. The exact reduction in depth could not be accurately measured, but a GPR survey was conducted to estimate the depth to the box-beam void. The depth to the void was then compared to the top flange thickness noted on the 1961 INDOT standard drawing (Fig. 2) to estimate the amount of section lost during the milling operation. Beams 1, 2, and 3 had the greatest loss of top flange thickness (up to approximately 2 in.), whereas beams 4, 5, 6, and 7 were reduced by 0.5 to 1 in. (12.7 to 25.4 mm). The reduction in depth caused a reduction in the moment of inertia, decreasing the flexural stiffness.

Second, removal of the wearing surface and a portion of the top flange (and therefore a portion of the grout between beams) may have allowed slip to occur at the shear keys (Fig. 16). The loss of shear key depth increased shear stresses in the keyway, which may have caused the shear key to crack and reduced the shear key's ability to distribute load to adjacent beams. Furthermore, the loss of material reduced the shear stiffness of the shear key.

Finally, removal of the wearing surface itself reduced both the longitudinal flexural stiffness and the transverse joint stiffness. However, considering the relatively low stiffness of the bituminous wearing surface, the contribution of wearing surface removal to the larger deflections of the directly loaded beams is thought to be small relative to the first two factors discussed.

LT3: Shear keys disabled

LT3 was conducted to verify that the shear-key-cutting operation had been successful in disabling the shear keys. Figure 15 shows that the deflected shape for LT3 had large discontinuities

at the beams that were directly loaded, indicating the shear keys were disabled. The measured deflections for the beams located between the truck tires were attributable to the proximity of the tires to the shear key joint. The distance between the rear axle tires of the truck was approximately 50 in. (1270 mm), whereas the width of one box beam was 45 in. (1143 mm). Consequently, it was difficult to position the truck so that both rear tires were straddling a beam. However, as shown for paths 4 and 9 in Fig. 15 (in which beams 4 and 6 were directly loaded), no significant loads were transferred to beams 3 and 7. The data for path 4 also show that beam 5 was disengaged. For paths 5 and 10 (in which beams 5 and 7 were directly loaded), beam 4 deflected less than 0.02 in. (0.51 mm), indicating that the beam was effectively disengaged. Although there was some transfer to beam 6 for paths 5 and 10, the large relative deflection between beam 6 and beams 5 and 7 indicates that the key was disengaged but some load was likely applied through the tires. Observation of the lack of load transferred between beams supports the conclusion that the shear keys were disabled.

LT4: Concrete deck added

LT4 was conducted 22 days after the deck was cast. The measured concrete cylinder compressive strength was 5800 psi (40.0 MPa) on the day preceding the load test. Figure 15 compares the results from LT4 and LT1. Although the data from paths 1 and 6 for LT4 cannot be compared to data from LT1, they are presented to provide complete results. The comparison indicates that load distribution was restored by the concrete deck after the shear keys were disabled. A smooth deflected shape is observed for LT1 and LT4. In addition, the deflections measured during LT4 were on average 37% less than the deflections measured during LT1.

The reduction in deflection provides evidence that the concrete deck was acting compositely with the beams even though it was constructed as a noncomposite deck. A simple

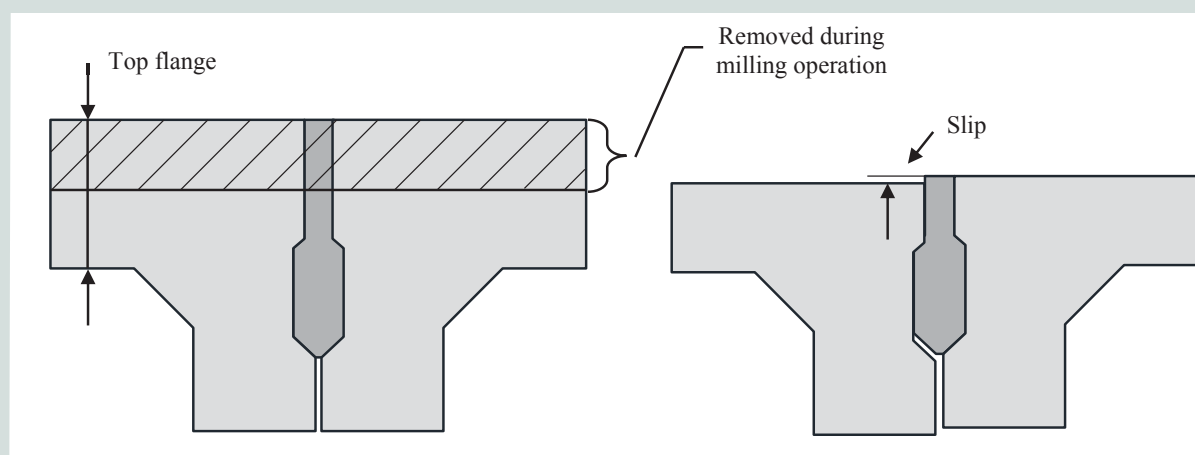


Figure 16. Illustration of shear key slip.

calculation based on the interface shear resistance provisions in Article 5.7.4.3 of the 2020 AASHTO LRFD specifications⁵ demonstrated that the cohesion between the concrete deck and concrete box beams for a width of 45 in. (1143 mm) resulted in a factored resistance of 36.5 kip/ft (533 kN/m). The corresponding shear flow generated by the fully factored HL-93 loading on the bridge was calculated to be 28.6 kip/ft (417 kN/m). Therefore, cohesion between the deck and the beams was adequate to transfer the horizontal shear required for composite action under the truck loading.

To further examine the amount of composite action between the box beams and the concrete deck, investigators calculated the estimated midspan deflection of each beam for LT1 $\delta_{est,LT1}$ (no concrete deck) and LT4 $\delta_{est,LT4}$ (considering full composite action) for the truck in position 4 for each load path. When estimating the midspan deflection of each beam, simple support conditions and elastic beam behavior were assumed. The load on each beam was distributed using the midspan deflection data for each load path. Deflections for LT1 were calculated using a moment of inertia of 30,100 in.⁴ (1.25×10^{10} mm⁴) as calculated for the beam without a concrete deck. Deflections for LT4 were calculated using a moment of inertia

of 53,100 in.⁴ (2.21×10^{10} mm⁴) as calculated for the composite beam and deck. The reduction in midspan deflection between LT1 and LT4 was calculated as $1 - (\delta_{est,LT4} / \delta_{est,LT1})$ for all load cases (Table 3). The calculated average reduction in midspan deflection was 39%. The reduction in measured midspan deflection between LT1 and LT4 was calculated as $1 - (\Delta_{LT4} / \Delta_{LT1})$, where Δ_{LT1} and Δ_{LT4} are the measured midspan deflections for LT1 and LT4, respectively. The average reduction in measured midspan deflection was 37% (Table 4). This comparison indicates that the concrete deck and concrete box beams exhibited full composite behavior.

Live-load distribution

The proportion of the truck load carried by each beam, herein referred to as live-load distribution, was determined by dividing the midspan deflection of a single beam by the sum of midspan deflections for every beam in the span, as shown in Eq. (1).

$$LLD_i = \frac{\Delta_{mid_i}}{\sum_{i=1}^7 \Delta_{mid_i}} \quad (1)$$

Table 3. Reduction in estimated deflection calculated as $1 - (\delta_{est,LT4} / \delta_{est,LT1})$

Path	Beam 1	Beam 2	Beam 3	Beam 4	Beam 5	Beam 6	Beam 7
2	0.43	0.49	0.49	0.43	0.42	0.26	0.12
3	0.33	0.44	0.50	0.50	0.50	0.37	0.21
4	0.20	0.26	0.33	0.45	0.43	0.39	0.22
5	0.32	0.30	0.37	0.43	0.45	0.38	0.30
7	0.39	0.49	0.50	0.46	0.44	0.28	0.08
8	0.32	0.40	0.49	0.48	0.49	0.37	0.24
9	0.17	0.22	0.31	0.46	0.46	0.46	0.32
10	0.24	0.27	0.32	0.44	0.45	0.38	0.31

Note: Average reduction = 0.39. $\delta_{est,LT1}$ = estimated midspan deflection for load test 1; $\delta_{est,LT4}$ = estimated midspan deflection for load test 4.

Table 4. Reduction in measured deflection calculated as $1 - (\Delta_{LT4} / \Delta_{LT1})$

Path	Beam 1	Beam 2	Beam 3	Beam 4	Beam 5	Beam 6	Beam 7
2	0.43	0.49	0.49	0.43	0.42	0.25	0.11
3	0.32	0.42	0.49	0.49	0.49	0.36	0.20
4	0.28	0.34	0.40	0.51	0.49	0.45	0.30
5	0.37	0.34	0.41	0.47	0.49	0.43	0.35
7	0.38	0.48	0.50	0.45	0.44	0.28	0.07
8	0.32	0.40	0.49	0.48	0.49	0.37	0.24
9	0.22	0.27	0.35	0.50	0.49	0.49	0.36
10	0.30	0.33	0.37	0.48	0.50	0.43	0.36

Note: Average reduction = 0.37. Δ_{LT1} = measured midspan deflection for load test 1; Δ_{LT4} = measured midspan deflection for load test 4.

where

LLD_i = live-load distribution to beam i (proportion of load carried by beam i)

$\Delta_{mid,i}$ = midspan deflection of beam i

i = beam number

By expressing the live-load distribution of each beam in this manner, the results from each load test can be compared independently of both the superstructure's flexural stiffness and variance in the truck's weight.

Wearing surface removed: LT1 compared with LT2

Figure 17 compares the live-load distribution for the load tests LT1, LT2, and LT4. It shows that the live-load distribution of the bridge after the wearing surface was removed (LT2) was reduced compared to the live-load distribution in the original condition (LT1). The live-load distribution was impaired because deflections of the beams that were directly loaded increased relative to the beams that were not directly loaded by the truck. The increase in relative deflection was caused primarily by an increase of slip in the joint (Fig. 16) and a reduction in the stiffness of the shear key, as previously discussed. The contribution of the wearing surface itself to live-load distribution was considered to be minimal.

Concrete deck added: LT1 compared with LT4

By comparing live-load distribution for LT1 and LT4, Fig. 17

shows that the addition of a concrete deck to the bridge without shear keys restored the live-load distribution to a level similar to or greater than that of the bridge in the original condition. For paths 5 and 10 (exterior beams loaded), the live-load distribution was restored to a similar level as the original condition (LT1) by the addition of a concrete deck. For paths 2, 3, 4, 7, 8, and 9 (interior beams loaded), the live-load distribution was improved relative to the original condition.

Investigators used the standard deviation of each load distribution curve for all curves loaded in LT1 and LT4 to further compare these two load tests (Table 5). The standard deviation provides a metric to describe the difference between the experimental results and a perfect load distribution. A standard deviation of zero indicates that all values in a data set are the same. Therefore, a standard deviation of zero for the load distribution values would indicate that all beams carried equal load. This scenario is considered a perfect load distribution. The population standard deviation was calculated using the load distribution values of beams 1 through 7 for each load path. Comparison of the values in Table 5 indicates that, for all cases, the load distribution provided by the concrete deck was improved or the same as the load distribution of the bridge in its original condition.

Live-load distribution factor

When a simplified beam-line analysis is used to determine the force effects for bridge design, a live-load distribution factor is required to assign a proportion of the force effects to each beam in the bridge.¹⁹ In this investigation, the measured deflection data from the load tests were used to determine the live-load distribution factors for the bridge in its original condition and after the concrete deck had been placed. The distribution factor for the interior beams is defined as the maximum of the live-load distribution values calculated using Eq. (1) for all the interior beams considering all load paths during both LT1 and LT4 (Fig. 17) while the truck was in position 4, the position corresponding with the largest midspan deflections. The distribution factor for the exterior beams is defined similarly and is equal to the maximum live-load distribution (Eq. [1]) of the two exterior beams. Table 6 provides the maximum distribution factors based on the experimental results.

Although the distribution factors for LT4 are higher than those for LT1, the differences are very small (0.01 and 0.02). Furthermore, the overall behavior of the bridge system improved with the addition of the deck due to the increased flexural stiffness of the bridge, resulting in decreased deflections and reduced stresses in the box beams under service loads.

The distribution factors for LT1 and LT4 are in good agreement with the distribution factors determined by analyzing the strain gauge data from load tests performed by Jones⁸ of an adjacent box-beam bridge constructed with a composite concrete deck without shear keys or transverse post-tensioning. For that bridge, the interior and exterior distribution factors were calculated to be 0.26 and 0.23, respectively.

Table 5. Standard deviation of load distribution

Path	Load test		Difference
	LT1	LT4	
1*	n.d.	0.07	n.d.
2	0.05	0.03	-0.02
3	0.03	0.01	-0.02
4	0.05	0.04	-0.01
5	0.07	0.07	0
6*	n.d.	0.07	n.d.
7	0.06	0.04	-0.02
8	0.03	0.01	-0.02
9	0.05	0.03	-0.02
10	0.07	0.07	0

Note: LT1 = load test 1; LT4 = load test 4; n.d. = no data.

*Deterioration prevented the use of paths 1 and 6 during LT1.

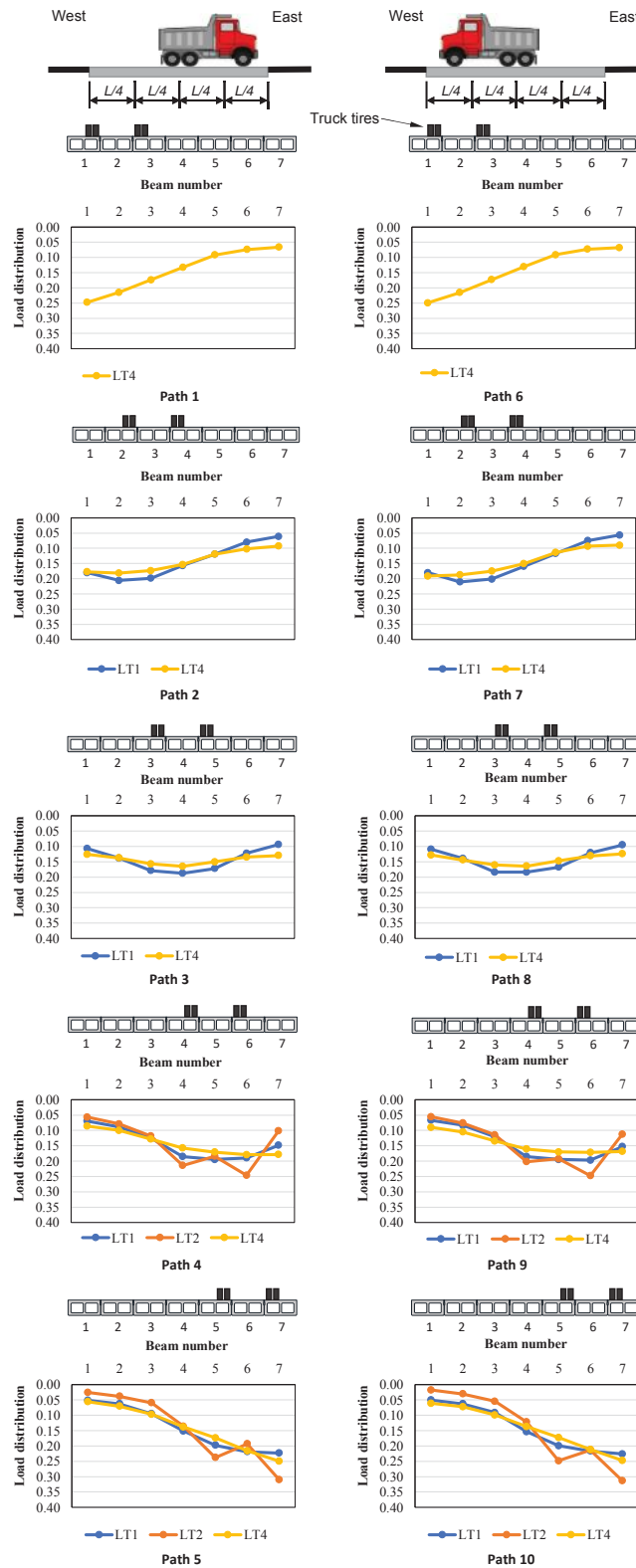


Figure 17. Summary of experimental live-load distribution for truck position 4. Note: The illustration at the top of the figure shows the longitudinal position of the truck (position 4) and the direction of travel corresponding to the plots that are provided below the illustration (eastbound for paths 1 through 5 and westbound for paths 6 through 10). A representation of the bridge cross section is illustrated above each load distribution plot, and a set of truck tires is shown on top of each cross section to indicate the transverse position of the truck for the indicated path. L = span length; LT1 = load test 1; LT2 = load test 2; LT3 = load test 3; LT4 = load test 4.

Table 6. Summary of live-load distribution factors

Beam location	Based on load test results		1957 AASHO standard specifications	2002 AASHTO standard specifications	2020 AASHTO LRFD specifications
	As built, LT1	With concrete deck added, LT4			
Interior	0.22	0.23	0.38	0.32	0.21
Exterior	0.23	0.25			0.24

Note: AASHO = American Association of State Highway Officials; AASHTO = American Association of State Highway and Transportation Officials.

1957 AASHO standard specifications live-load distribution factor

The 1957 AASHO standard specifications⁹ do not include specific design equations to calculate distribution factors for adjacent beam bridges. The specifications only include guidance for concrete stringers. Assuming that the load distribution expression for concrete stringers was used in the design of the bridge of the current study, the applicable expression from Table 1.3.1 of the AASHO specifications is as follows:

$$\text{load fraction} = \frac{S}{5.0} \quad (2)$$

where

load fraction = wheel-load distribution factor

S = beam spacing

The width of the beam in the bridge is 3.75 ft (1.14 m), resulting in a load fraction value of 0.75. The relationship between the load fraction and the live-load distribution factors in the 2020 AASHTO LRFD specifications⁵ is discussed later.

2002 AASHTO standard specifications live-load distribution factor

In article 3.23.4, Eq. (3.11) of the 2002 AASHTO *Standard Specifications for Highway Bridges*,²⁰ the live-load distribution factor for moment, specified as a wheel-load distribution factor, is expressed as follows:

$$\text{Load fraction} = \frac{S}{D} \quad (3)$$

where

$D = (5.75 - 0.5N_L) + 0.7N_L(1 - 0.2C)^2$

N_L = number of traffic lanes on the bridge

$C = K(W/L)$ for $W/L < 1$

$= K$ for $W/L \geq 1$

$K = \left[(1 + \mu) \left(\frac{I}{J} \right) \right]^{0.5}$

W = overall width of the bridge

L = span length of the beams

μ = Poisson's ratio of concrete

I = moment of inertia of the beam section

J = torsional constant

The torsional constant J is approximated using Eq. (4):

$$J = \frac{2t_f(b-t)^2(d-t_f)^2}{bt + dt_f - t^2 - t_f^2} \quad (4)$$

where

t = web thickness (use single web for multiple web beam)

t_f = flange thickness

b = width of the beam

d = depth of the beam

For the calculation of load distribution, section properties were taken from the 1961 INDOT standard drawing (Fig. 2); Poisson's ratio was assumed to be 0.2, as recommended by the 2002 AASHTO standard specifications; and the number of lanes is 2.¹⁹ The resulting load fraction value calculated from Eq. (3) and Eq. (4) is 0.64.

2020 AASHTO LRFD specifications live-load distribution factors

The 2020 AASHTO LRFD specifications⁵ provide an empirical equation for live-load distribution developed by Zokaie et al.²¹ To determine the live-load distribution using the 2020 AASHTO LRFD specifications, investigators categorized the bridge in this study as having a Case (f) typical cross section (Table 4.6.2.2.1-1). Then they used the following equation from Table 4.6.2.2.2b-1 of the specifications to estimate the live-load distribution factor for moment in an interior girder $g_{int,m}$:

$$g_{int,m} = k \left(\frac{b}{33.3L} \right)^{0.35} \left(\frac{I}{J} \right)^{0.25} \quad (5)$$

where

$k = 2.5(N_b)^{-0.2} \geq 1.5$

N_b = number of beams in the bridge

Similarly, investigators used the following equation from Table 4.6.2.2.2d-1 of the 2020 AASHTO LRFD specifications to calculate the live-load distribution factor for moment in an exterior girder $g_{ext,m}$:

$$g_{ext,m} = g_{int,m} \left(1.125 + \frac{d_e}{30} \right) \quad (6)$$

where

d_e = distance from the centerline of the exterior web to the interior edge of the curb

The curbs of the bridge sit on top of the exterior web of the exterior beam. Therefore, a d_e of 0 ft (0 m) was used for the calculation of $g_{ext,m}$. Using section properties taken from the 1961 INDOT standard drawing (Fig. 2), the live-load distribution factors for moment were calculated from Eq. (5) and (6) to be 0.25 and 0.29 for the interior and exterior beams, respectively.

To compare the live-load distribution factors calculated using the equations in the 2020 AASHTO LRFD specifications to the measured distribution factors, the calculated distribution factors were divided by a multiple presence factor of 1.2 in consideration of the single-lane loading of the load tests. The resulting distribution factors are 0.21 and 0.24 for the interior and exterior beams, respectively.

Discussion

As presented in the preceding sections, the live-load distribution factors in both the 1957 AASHO⁹ and 2002 AASHTO standard specifications²⁰ are given as a “load fraction.” These factors are intended to be applied to the wheel load of the standard truck loading, which is equal to half the axle load of the design truck (Fig. 18). However, both the live-load

distribution factors based on deflection data from the load tests conducted in this study and the live-load distribution factors defined in the 2020 AASHTO LRFD specifications⁵ are intended to be applied to the load effect of the entire design truck over the full design lane. Therefore, to compare the distribution factors from both the test data and the 2020 AASHTO LRFD specifications to the load fraction values in the 1957 AASHO and 2002 AASHTO standard specifications, the results of Eq. (2) and (3) must be divided by 2.

Table 6 summarizes the design live-load distribution factors and the factors based on the load tests. The 1957 and 2002 standard specifications substantially overestimate the distribution factors of the bridge (and resulting demand on the box beams) for both LT1 and LT4. Load ratings performed using the older specifications are therefore conservative. The interior load distribution factor calculated using the expression in the 2020 AASHTO LRFD specifications is in excellent agreement with the experimental results. A similar agreement is observed for the exterior load distribution factors. These results indicate that the live-load distribution factors for moment in the 2020 AASHTO LRFD specifications corresponding to the Case (f) cross section may be used for a bridge with a concrete deck on adjacent box beams without shear keys.

Summary and conclusion

An experimental investigation was conducted on a full-scale adjacent precast, prestressed concrete box-beam bridge in the field. The study included four load tests on the bridge under four conditions: as-built, after removal of the bituminous wearing surface, after the shear keys were disabled, and with a reinforced concrete deck installed. Load was applied using a triaxle truck, and quarter-point deflections of each beam were measured. Load distribution was calculated based on the midspan deflections of each beam when the truck was in the load position corresponding to the maximum recorded deflections. The load distribution was compared among all load tests. Furthermore, the experimental load distribution factors for each load test were determined. The appropriate experimental distribution factors were then compared with the load fraction factors calculated based on the 1957 AASHO⁹ and 2002 AASHTO²⁰ standard specifications, as well as the interior and exterior distribution factors for moment calculated using equations from the 2020 AASHTO LRFD specifications.⁵ The primary findings of the investigation are as follows:

- Leaking shear keys are not an indication that load transfer has been eliminated or that the shear keys are ineffective in distributing live load. The test results indicate that even though the shear keys were leaking, live-load distribution was maintained.
- The results of the load tests indicate that the addition of a reinforced concrete deck can restore load distribution even if the primary load distribution mechanism consid-

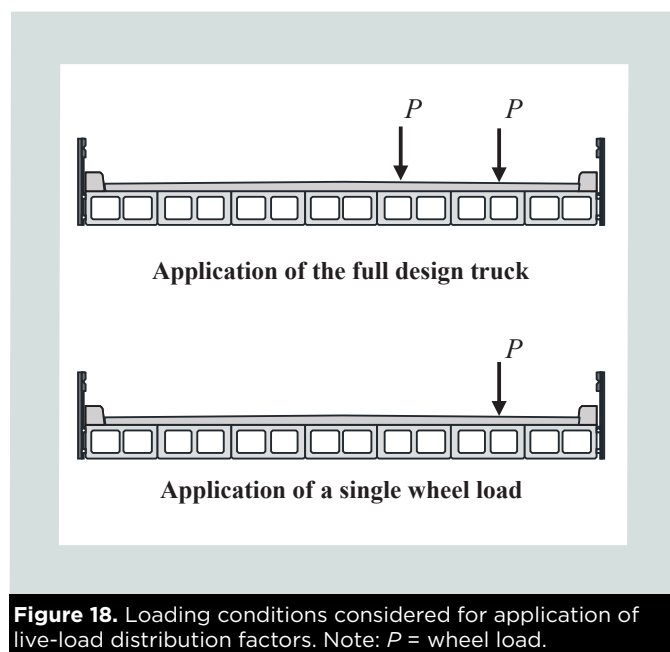


Figure 18. Loading conditions considered for application of live-load distribution factors. Note: P = wheel load.

ered in design (shear keys) is disabled. The addition of a reinforced concrete deck provides an excellent method for improving both the load rating of a deteriorated box-beam bridge and the overall behavior of the bridge.

- A concrete deck placed on concrete beams can achieve full composite action through cohesion between the deck concrete and the concrete beams. The surface should be properly cleaned and roughened prior to placement of the concrete deck. Through composite action, the addition of the deck is not only able to improve load distribution but also can reduce service stresses and deflections of the box beams.
- The load fraction factors calculated based on both the 1957 AASHTO and 2002 AASHTO standard specifications were found to be conservative for load rating 1950s-era adjacent box-beam bridges. Similar results are provided by both load fraction equations, and both significantly overestimate the demand on the box beams.
- The expressions in the 2020 AASHTO LRFD specifications for live-load distribution factors for moment provide accurate estimates of the load distribution of an adjacent box-beam bridge. These distribution factors are also appropriate for estimating the live-load distribution factors corresponding to a reinforced concrete deck on adjacent concrete beams without shear keys or with shear keys that are considered damaged or disabled.

Acknowledgments

The authors would like to thank the Indiana Department of Transportation; the Local Technology Assistance Program in Indiana; the Joint Transportation Research Program; and Tippecanoe County, Ind., for making this research possible. The technical perspectives and conclusions reported in this paper are those of the authors, and the authors alone are responsible for the facts and accuracy of the data presented.

References

1. Steinburg, E., R. Miller, D. Nims, and S. Sargand. 2011. *Structural Evaluation of LIC-310-0396 and FAY-35-17-6.82 Box Beams with Advanced Strand Deterioration*. FHWA/OH-2011/16. Columbus, OH: Ohio Department of Transportation, Office of Innovation, Partnerships and Energy. https://www.dot.state.oh.us/Divisions/Planning/SPR/Research/reportsandplans/Reports/2011/Structures/134381_ES.pdf.
2. Kassner, B. L., and S. S. G. Balakumaran. 2017. "Live-Load Test of a 54-Year Old Prestressed Concrete Voids Slab Bridge." Presentation at PCI Convention and National Bridge Conference, February 28–March 4, 2017, Huntington Convention Center, Cleveland, OH.
3. AASHTO (American Association of State Highway and Transportation Officials). 2010. *AASHTO LRFD Bridge Design Specifications*. 5th ed. Washington, DC: AASHTO.
4. AASHTO. 2012. *AASHTO LRFD Bridge Design Specifications*. 6th ed. Washington, DC: AASHTO.
5. AASHTO. 2020. *AASHTO LRFD Bridge Design Specifications*. 9th ed. Washington, DC: AASHTO.
6. Attanayake, U., and H. Aktan. 2013. "First-Generation ABC System, Evolving Design, and Half a Century of Performance: Michigan Side-by-Side Box-Beam Bridges." *Journal of Performance of Constructed Facilities* 29 (3). [https://doi.org/10.1061/\(ASCE\)CF.1943-5509.0000526](https://doi.org/10.1061/(ASCE)CF.1943-5509.0000526).
7. AASHTO. 2019. *Manual for Bridge Evaluation, with 2019 Interims Revisions*. Washington, DC: AASHTO.
8. Jones, H. L. 1999. *Multi-Box Beam Bridges with Composite Deck*. FHWA/TX-OO/1709-1. College Station: Texas A&M University. <https://static.tti.tamu.edu/tti.tamu.edu/documents/1709-1.pdf>.
9. AASHTO (American Association of State Highway Officials). 1957. *Standard Specifications for Highway Bridges*. 7th ed. Washington, DC: AASHTO.
10. INDOT (Indiana Department of Transportation). 2013. *Indiana Design Manual—2013*. https://www.in.gov/indot/design_manual/design_manual_2013.htm.
11. AASHTO. 2017. *AASHTO LRFD Bridge Design Specifications*. 8th ed. Washington, DC: AASHTO.
12. ASTM International. 2018. *Standard Specification for Portland Cement*. ASTM C150/C150M. West Conshohocken, PA: ASTM International.
13. ASTM International. 2016. *Standard Specification for Air-Entraining Admixtures for Concrete*. ASTM C260/C260M. West Conshohocken, PA: ASTM International.
14. ASTM International. 2017. *Standard Specification for Chemical Admixtures for Concrete*. ASTM C494/C494M. West Conshohocken, PA: ASTM International.
15. INDOT. 2018. *2018 Standard Specifications*. <https://www.in.gov/dot/div/contracts/standards/book/sep17/sep.htm>.
16. ASTM International. 2018. *Standard Practice for Making and Curing Concrete Test Specimens in the Field*. ASTM C31/C31M. West Conshohocken, PA: ASTM International.
17. ASTM International. 2018. *Standard Test Method for Compressive Strength of Cylindrical Concrete Specimens*. ASTM C39/C39M. West Conshohocken, PA: ASTM International.

18. ASTM International. 2018. *Standard Specification for Deformed and Plain Carbon-Steel Bars for Concrete Reinforcement*. ASTM A615/A615M. West Conshohocken, PA: ASTM International.
19. Barker, R. M., and J. A. Puckett. 1997. *Design of Highway Bridges*. New York, NY: John Wiley & Sons.
20. AASHTO. 2002. *Standard Specifications for Highway Bridges*, 17th ed. Washington, DC: AASHTO.
21. Zokaie, T., T. A. Osterkamp, and R. A. Imbsen. 1991. *Distribution of Wheel Loads on Highway Bridges*. National CHRP 12-26 Final Report Volume 1. Washington, DC: Transportation Research Board. http://onlinepubs.trb.org/onlinepubs/nchrp/docs/NCHRP12-26_FR.pdf.

Notation

b	= width of the beam
C	= empirical constant
d	= depth of the beam
d_e	= distance from the centerline of the exterior web to the interior edge of the curb
D	= empirical constant
$g_{ext,m}$	= exterior beam live-load distribution factor for moment
$g_{int,m}$	= interior beam live-load distribution factor for moment
i	= beam number
I	= moment of inertia of beam section
J	= torsional constant
k	= empirical constant
K	= empirical constant
L	= span length
$LLDi$	= live-load distribution to beam i (proportion of load carried by beam i)
<i>load fraction</i>	= wheel-load distribution factor
N_b	= number of beams in the bridge cross section
N_L	= number of traffic lanes on the bridge
P	= wheel load

S	= beam spacing
t	= web thickness
t_f	= flange thickness
W	= overall width of the bridge
$\delta_{est,LT1}$	= estimated midspan deflection for load test 1
$\delta_{est,LT4}$	= estimated midspan deflection for load test 4
ΔLT_1	= measured midspan deflection for load test 1
ΔLT_4	= measured midspan deflection for load test 4
Δ_{mid_i}	= midspan deflection of beam i
μ	= Poisson's ratio of concrete

About the authors



Ryan T. Whelchel, PhD, is a bridge engineer at Beam, Longest, and Neff. His work is focused on the design, inspection, and rehabilitation of all types of bridges. Whelchel holds a bachelor's degree in architectural engineering from Kansas State University in Manhattan, Kans., and a master's degree and PhD in civil engineering from Purdue University in West Lafayette, Ind. His graduate work concerned the study of the deteriorated behavior of prestressed concrete bridge beams and the nondestructive evaluation of reinforced concrete.



Christopher S. Williams, PhD, is an assistant professor of civil engineering at Purdue University. He received his bachelor of science degree from Southern Illinois University Carbondale and his master of science and PhD from the University of Texas at Austin. He is a consulting member of the PCI Committee on Bridges and the Committee on Bridges Precast Post-tensioned Bridges Subcommittee.



Robert J. Frosch, PhD, PE, FACI, FASCE, is a professor of civil engineering and senior associate dean of facilities and operations in the Purdue University College of Engineering. A fellow of the American Concrete Institute (ACI), he is the editor-in-chief of the *ACI Structural Journal* and serves on the ACI 318 Structural Concrete Building Code Committee, for which he chairs ACI 318D, Structural Members. His research, which focuses on the design and behavior of structural concrete, has resulted in changes to the ACI building code and the American Association of State Highway and Transportation Officials' design specifications.

Abstract

Leaking longitudinal joints are commonly observed in adjacent box-beam bridges and are often associated with an assumed loss of load distribution at the leaking joint. To address the lack of test data and general uncertainty in analyzing deteriorated concrete structures, a series of load tests was conducted to determine the load distribution of a deteriorated adjacent concrete box-beam bridge. Load distribution was investigated for the existing structure with leaking joints as well as for the structure following rehabilitation with a noncomposite reinforced concrete deck. The bridge was tested in four conditions: as built, after removal of the bituminous wearing surface, after the shear keys were disabled, and with a reinforced concrete deck installed. Load distribution was assessed for each condition, and the results were compared with design equations. In addition to assessing load distribution of the existing bridge, the results of this study can serve as support for the use of a concrete deck as a rehabilitation strategy to restore load distribution or function as the primary load distribution mechanism of an adjacent box-beam bridge.

<https://doi.org/10.15554/pci.66.6-03>

Keywords

Adjacent box-beam bridge rehabilitation, concrete deck, deteriorated prestressed concrete, live-load distribution, load rating, load testing.

Review policy

This paper was reviewed in accordance with the Precast/Prestressed Concrete Institute's peer-review process.

Reader comments

Please address any reader comments to *PCI Journal* editor-in-chief Tom Klemens at tklemens@pci.org or Precast/Prestressed Concrete Institute, c/o *PCI Journal*, 8770 W. Bryn Mawr Ave., Suite 1150, Chicago, IL 60631. [f](#)

*LEAVE YOUR MARK ON
THE THE FUTURE*

MAKE A LEGACY GIFT

Make a lasting statement about who you are and what is important to you.

You can do it today with a legacy gift through your will.

- Costs you nothing during your lifetime
- Preserves your savings and current cash flow
- Can be changed, reworked or revoked as needed
- Easy to arrange. A simple paragraph is all it takes and you don't have to rewrite your will.



INTERESTED?

Contact the PCI Foundation
Marty McIntyre
(708) 386-1715
info@pci-foundation.org



DIRECTORIES

Board of Directors

Dennis Fink, Chair, *Northeast Prestressed Products LLC*

J. Matt DeVoss, Vice Chair, *Jackson Precast Inc.*

Matt Ballain, Secretary-Treasurer, *Coreslab Structures (INDIANAPOLIS) Inc.*

J. Seroky, Immediate Past Chair, *High Concrete Group LLC*

Bob Risser, President and CEO, *PCI*

Dusty Andrews, Producer Member Director, *PCI Washington/Oregon, Knife River Corp.-Northwest*

Dennis Cilley, Associate Member Director, *Erector, American Steel & Precast Erectors*

Todd Culp, Producer Member Director, *PCI Midwest, Coreslab Structures (OMAHA) Inc.*

Jim Fabinski, Institute Program Director, *Transportation Activities, EnCon Colorado*

Greg Force, Institute Program Director, *Research and Development, Tindall Corp.*

Ashley Fortenberry, Associate Member Director, *Erector, Tindall Corp.*

Harry Gleich, Institute Program Director, *Technical Activities, Metromont Corp.*

Matt Graf, Producer Member Director, *PCI Illinois/Wisconsin, International Concrete Products Inc.*

Shelley Hartnett, Producer Member Director, *PCI Mountain States, EnCon United*

Lloyd Kennedy, Institute Program Director, *Educational Activities, Finrock Industries LLC*

Brent Koch, Producer Member Director, *PCI West, Con-Fab California LLC*

AJ Krick, Producer Member Director, *Mid-Atlantic, Smith-Midland Corp.*

Matt Mahonski, Producer Member Director, *PCI Central, High Concrete Group*

Bill Mako, Producer Member Director, *Georgia/Carolinas PCI, Atlanta Structural Concrete Co.*

David Malaer, Producer Member Director, *Texas, Oklahoma, New Mexico, Valley Prestress Products Inc.*

Jane Martin, Institute Program Director, *Marketing, Gate Precast Co.*

Phillip Miller, Producer Member Director, *PCI Gulf South, Alfred Miller Contracting*

Chris Mosley, Professional Member Director, *The Consulting Engineers Group Inc.*

Patty Peterson, Institute Program Director, *Business Performance, Tindall Corp.*

Jim Renda, Associate Member Director, *Supplier, Cresset Chemical Co.*

Cheryl Rishcoff, Professional Member Director, *TRC Worldwide Engineering Inc.*

Lenny Salvo, Producer Member Director, *Florida Chapter, Coreslab Structures (ORLANDO) Inc.*

Bob Sheehan, Associate Member Director, *Supplier, BASF Corp.*

Peter Simoneau, Producer Member Director, *PCI Northeast, Dailey Precast*

Gary Wildung, Institute Program Director, *Quality Activities, FDG Inc.*

Daniel Eckenrode, Regional Council Representative, *Nonvoting, PCI Gulf South*

Technical Activities Council

Chair Harry Gleich

Vice Chair Rich Miller

Secretary Jared Brewe

Ex-officio, fib Representative

Larbi Sennour

Ex-officio, Code Representatives

S. K. Ghosh and Stephen V. Skalko

Dusty Andrews

Suzanne Aultman

Ned M. Cleland

Mary Ann Griggas-Smith

David Jablonsky

Wayne Kassian

Yahya Kurama

John Lawler

Barry McKinley

Christopher Mosley

Pinar Okumus

Timothy Salmons

Stephen J. Seguirant

Venkatesh Seshappa

PCI staff

Tom Bagsarian	(312) 428-4945	tbagsarian@pci.org	Editorial content manager
Laura Bedolla	(312) 360-3218	lbedolla@pci.org	Technical activities program manager
Jared Brewe	(312) 360-3213	jbrew@pci.org	Technical services vice president
Trina Brown	(312) 360-3590	tbrown@pci.org	Transportation systems program manager
K. Michelle Burgess	(312) 282-8160	mburgess@pci.org	<i>PCI Journal</i> managing editor
Nikole Clow	(312) 360-3202	nclow@pci.org	Marketing coordinator
Royce Covington	(312) 428-4946	rcovington@pci.org	Member services manager
Cher Doherty	(312) 583-6781	cdoherty@pci.org	Manager, events
Walter Furie	(312) 583-6772	wfurie@pci.org	Production senior specialist
Christopher Hurst	(312) 360-3203	churst@pci.org	Membership project manager
Cody Kauh	(312) 583-6778	ckauh@pci.org	Web developer
Michael Kesselmayer	(312) 583-6770	mkesselmayer@pci.org	Quality programs managing director
Becky King	(312) 360-3201	bking@pci.org	Market development and education managing director
Tom Klemens	(312) 583-6773	tklemens@pci.org	Publications director
Ken Kwilinski	(312) 428-4944	kkwilinski@pci.org	Quality systems manager
Carolina Lopez	(312) 583-6774	clopez@pci.org	Certification programs coordinator
John McConvill	(312) 360-3208	jmconvill@pci.org	Controller
Sherrie Nauden	(312) 360-3215	snauden@pci.org	Continuing education manager
William Nickas	(312) 583-6776	wnickas@pci.org	Transportation systems managing director
Bob Risser	(312) 360-3204	brisser@pci.org	President and chief executive officer
Lisa Scacco	(312) 583-6782	lscacco@pci.org	Publications manager
Neal Sherman	(312) 786-0300	nsherman@pci.org	Staff accountant
Edith Smith	(312) 360-3219	esmith@pci.org	Codes and standards managing director
Mike Smith	(312) 786-0300	msmith@pci.org	Information technology manager
Beth Taylor	(312) 583-6780	btaylor@pci.org	Chief financial and administrative officer
Trice Turner	(312) 583-6784	tturner@pci.org	Business development manager
Cindi Ward	(312) 360-3214	cward@pci.org	Data quality and office administrative services coordinator
Randy Wilson	(312) 428-4940	rwilson@pci.org	Architectural precast systems director

Regional offices

Florida Prestressed Concrete Association

Diep Tu
Phone: (407) 758-9966
Email: diep@myfpca.org
MyFPCA.org

Georgia/Carolinas PCI

Ray Clark
Phone: (678) 402-7727
Email: ray.clark@gcpci.org
GCPCI.org

PCI Central Region

Phil Wiedemann
Phone: (937) 833-3900
Email: phil@pci-central.org
PCI-Central.org

PCI Gulf South

Dan Eckenrode
Phone: (228) 239-3409
Email: pcigulfsouth1@att.net
PCIGulfSouth.org

PCI of Illinois & Wisconsin

Joe Lombard
Phone: (312) 505-1858
Email: joe@pci-iw.org
PCI-IW.org

PCI Mid-Atlantic

Dawn Decker
Phone: (717) 682-1215
Email: dawn@pci-ma.org
PCI-MA.org

PCI Midwest

Mike Johnsrud
Phone: (952) 806-9997
Email: mike@pcimidwest.org
PCIMidwest.org

PCI Mountain States

Jim Schneider
Phone: (303) 562-8685
Email: jschneider@pcims.org
PCIMS.org

PCI Northeast

Rita Seraderian
Phone: (617) 484-0506
Email: contact@pcine.org
PCINE.org

PCI West

Ruth Lehmann
Phone: (949) 420-3638
Email: info@pciwest.org
PCIWest.org

Precast Concrete Manufacturers' Association

Chris Lechner
Phone: (866) 944-7262
Email: chris@precastcma.org
PrecastCMA.org

Coming ahead

Reinforcement

- High-cycle fatigue tests of pretensioned concrete beams

Also

- Impact of pile-to-cap fixity on the design and behavior of sensitive structures
- Expected compressive strength in precast, prestressed concrete design
- Structural grouting of load-bearing precast concrete elements—Issues and solutions
- Meet Cheryl Rishcoff



MEET KENNETH KRUSE

Forming a market

Sarah Fister Gale



Kenneth Kruse could have built a career around any industry he wanted, but once he discovered precast concrete, he was done looking.

"I was absolutely fascinated with precast," Kruse says of his first experience with the material. "It was so cool, and you could

build so many things with it."

Kruse was born and raised in Cincinnati, Ohio, the youngest of seven siblings. He received his bachelor's and master's degrees from the University of Cincinnati, where he participated in the school's co-op program working every other semester for industry organizations, including Proctor & Gamble. "Not many schools offer co-op programs anymore, but it was a great experience," he says.

Shortly after graduating, Kruse landed a job with BASF, the world's largest chemical producer, with subsidiaries in more than 80 countries. BASF's talent development model encourages new hires to work for a time in several business units to help them build a network and find their area of interest. Kruse's first assignment was in construction chemicals, which mostly focused on cast-in-place concrete.

At the time, BASF was already a leading supplier of chemicals for ready-mixed concrete, so Kruse went looking for other industries to support. That's when he found PCI. "I went to my first PCI Convention, and I was hooked," he says.

He immediately saw the cost and quality benefits that precast concrete designs brought to a project, and he liked that it was adaptable enough to be used in a variety of projects, such as hotels, bridges, and parking structures. "It had such a great value proposition," he says.

He was surprised that precast concrete didn't have a larger market share but found most of the stakeholders were engineers who weren't trained in how to market their products effectively. So Kruse decided to help them.

He let his bosses know that he wanted to stay in construction materials and focus on the precast concrete industry. Then he spent the next 35 years working with PCI and precast concrete manufacturers to expand the industry and broadcast the story of what precast concrete can do.

Early on he met with Tom Battles, who was the president and CEO of PCI at the time, to talk about market share and how the industry could double its sales potential with the right

marketing. Battles agreed and encouraged Kruse to act as an ambassador for the industry and to meet with PCI members to discuss how they could expand their market presence.

Kruse met with PCI board members and local leaders and gave presentations at dozens of PCI events to share his message: "If you merge technology and strategy, you can dominate the industry."

He eventually launched the Market Research and Metrics Committee with the goal of measuring the industry's market share. The idea was to quantify how much business PCI members were conducting in what segments and to define the percentage of the marketplace that work represented so they would have a baseline to grow that number.

At first, members were wary. Kruse recalls presenting the committee idea in a PCI meeting and asking the 45 participants in the room to sign up if they were interested in participating.

"We didn't get a single name," he says. Still, Kruse pushed forward, conducting surveys and talking with members about the products they made and the geographies and segments they served to get a sense of the industry's scale. He also asked them questions about revenue and pay scales to get a sense of how competitive the industry was compared with other areas of construction as a way to improve industry recruiting.

Many members were hesitant to share those numbers, even anonymously, but eventually Kruse persuaded them to participate. Over the years, the data has helped PCI members rethink their business strategies, which helped the industry grow and attract new talent, including a more diverse pool of engineers. Today, the Market Research and Metrics Committee captures detailed data about sales and market share by segment, including bridges, residence halls, churches, and prisons. Members use this data to build more effective business strategies. "We had a rough beginning, but we worked it out," he says.

Kruse went on to participate on many more committees, including the Digital Marketing Committee, Emerging Markets Committee, and Residential Market Team, and held positions on the PCI Board of Directors. He is a Fellow of PCI and the Canadian Precast/Prestressed Concrete Association.

Kruse retired last year and never regretted making precast concrete the focus on his career. "I'm proud I made that decision," he says. "I got to work with the people who built this industry, and I still love the technology and everything precast can do." ■

Always looking out for the safety of You and Your projects

7233 HEAD HARNESS ASSEMBLY

INSTALLATION VALVES

6893

6895
FILTER HOLDER

6895

6889
EXHALATION VALVE

THE CONSULTING ENGINEERS GROUP, INC.

CEG ILLINOIS
847-255-5200

CEG NEW MEXICO
505-796-0972

CEG TEXAS
210-637-0977

CEG FLORIDA
321-275-0580

www.cegengineers.com



HAMILTON FORM INDUSTRY INNOVATORS

"Hamilton Form guided our company with a high level of expertise as we collaborated on the form design. The forms are innovative and efficient, which will allow our company to manufacture a high-quality product with minimal effort. Their knowledge and teamwork throughout this process has been a key in this project's success."

Ron Sparks, VP/GM, Columbia Precast Products

OUR INNOVATIVE CUSTOM FORMS, BRING YOUR PROJECTS TO REALITY.

Hamilton Form is known for high-quality, hardworking custom forms and equipment, like the forms built for Columbia Precast to produce sound walls for the Washington State DOT I-90 corridor improvement project.

The forms cast 8-foot sound walls with integral monolithic pilasters and were designed to accept custom form liners. Internal headers are used to adjust wall heights from 31-35 feet. Hydraulically-actuated side forms make stripping and set-up efficient and easy.

When you need innovative formwork and custom equipment solutions, call on Hamilton Form to deliver: **817 590-2111** or sales@hamiltonform.com



Hamilton Form Company, Ltd.

7009 Midway Road, Fort Worth, Texas 76118
www.hamiltonform.com

